MAGNETIC EXCHANGE INTERACTIONS: THE SYNTHESIS AND CHARACTERIZATION OF SUPERPARAMAGNETIC NIFE$_2$O$_4$ NANOCRYSTALS

A Dissertation
Presented to
The Academic Faculty

by

Eric Thomas Drew

In Partial Fulfillment
of the Requirements for the Degree
Doctor of Philosophy in the
Chemistry and Biochemistry

Georgia Institute of Technology
December 2020

MAGNETIC EXCHANGE INTERACTIONS: THE SYNTHESIS AND CHARACTERIZATION OF SUPERPARAMAGNETIC NIFE$_2$O$_4$ NANOCRYSTALS

Approved by:

Dr. Z. John Zhang, Advisor
School of Chemistry and Biochemistry
Georgia Institute of Technology

Dr. Angus Wilkinson
School of Chemistry and Biochemistry
Georgia Institute of Technology

Dr. Younan Xia
School of Chemistry and Biochemsitry
Georgia Institute of Technology

Dr. Mostafa El-Sayed
School of Chemistry and Biochemistry
Georgia Institute of Technology

Dr. Christopher W. Jones
College of Science and Engineering
Georgia Institute of Technology

Date Approved: October 9, 2020

ACKNOWLEDGEMENTS

improve myself. To all the friends made along the way, you helped strike an incredible balance between work and life that spawned many fond memories and immeasurable fun throughout the years. And special thanks to Dr. Osiris Martinez-Guzman, my best friend and partner throughout our studies, thank you. You are my rock and support, grounding me through words of encouragement, you've patiently listened to my science and thoughts, and have shared many fond memories that made my time at Georgia Tech a pleasure. Thank you for all you have given, the love, support, and friendship; this wouldn't have been possible without you and you are deserving of pages of thanks but for the sake of breviate and conservation of trees, thank you for everything.

Thank you to everyone, I will never forget the love and support that made this work possible and culminated in Dr. Eric Drew!

TABLE OF CONTENTS

LIST OF TABLES

LIST OF FIGURES

LIST OF SYMBOLS AND ABBREVIATIONS

χ Magnetic susceptibility (emu/g*G)

T_B Blocking temperature

T_C Curie temperature

T_N Néel temperature

H_C Coercivity (Oe)

H_{EB} Exchange bias field shift (Oe)

H_0 Applied magnetic field

M_S Saturation magnetization (emu/g)

M_r Remanent magnetization (emu/g)

C Curie constant

E_A Anisotropy energy

K Magnetocrystalline anisotropy constant

V Volume (nm^3)

θ Angle

k_B Boltzmann constant

λ Wavelength

μ_B Bohr magneton

ν Frequency

E_{EX} Exchange coupling energy

A_{int} Interfacial contact area (nm^2)

SUMMARY

Magnetic nanoparticles have been pursued for various applications that include catalytic systems, data storage, biomedical imaging, drug delivery, sensors, and nanoelectronics. For many of these applications it is essential to tune the magnetic properties through careful synthetic manipulation to control chemical composition, morphology, and crystallite size. Further understanding of the fundamental relationships between magnetic properties and microstructure is necessary to meet the emerging technological needs. Spinel ferrite nanoparticles provide a flexible system to study this relationship due to their unique ferrimagnetism, variable chemical composition, and chemical stability. The purpose of this thesis is to study the unique magnetic properties through the synthesis of spinel ferrite based nanoparticles of variable composition, exchange-coupled hard/soft core@shell nanoparticles, and exchange biased ferrimagnetic (FiM)@ antiferromagnetic (AFM) nanoparticles. **Chapter 2** studies synthesis of redox-sensitive $NiFe_2O_4$ nanoparticles through modification of the aminolytic synthetic method (a method developed in the Zhang group). Through seed-mediate modified-aminolytic synthesis a study of the size-dependent magnetic properties of $NiFe_2O_4$ nanoparticles ranging from ~4-10 nm in diameter was performed as well an investigation into their ferromagnetic resonance properties. **Chapter 3** utilizes the versatile nature of the modified-aminolytic synthesis to study how the substitution of different divalent metal cations (A = Co^{2+}, Zn^{2+}, Mn^{2+}, and etc.) alters the magnetic properties of mixed composition $Ni_{1-x}A_xFe_2O_4$ nanoparticles. This series is to demonstrate a strategy to tune ferromagnetic resonance of spinel ferrites through understanding the relationship between

the effective magnetic anisotropy and ferromagnetic resonance absorption. This endeavor should allow for the design of tunable microwave materials via control of chemical composition to meet the requirements of communication and antenna technological. **Chapter 4** expands on the versatility of the seed-mediated modified-aminolytic method to synthesize bimagnetic exchange-coupled core@shell ferrimagnetic nanoparticles in which the core and shell materials have varied magnetic anisotropy energies (E_A). The design of exchange-coupled nanomaterials has been pursued as a method to achieve rare-earth free permanent magnets through the creation of exchange spring magnets that is a hybrid of beneficial magnetic properties of the hard/soft ferrimagnetic phases such as the large effective magnetocrystalline anisotropy (coercivity H_C) of the hard phase and large saturation magnetization (M_S) to achieve a magnetic squareness factor (M_r/M_s) closer to 1. Ferromagnetic resonance spectroscopy demonstrates that microwave absorption is largely dictated by the surface state of the nanomaterial and careful design of a core@shell heterostructure can lead to strategies to tune material properties to meet technological needs. **Chapter 5** studies the synthesis of nanoparticle analogs of bulk antiferromagnetic materials such as NiO and CoO. These antiferromagnetic nanoparticles demonstrate unique superparamagentic behavior in sub-10 nm single domain crystals. **Chapter 6** investigates the magnetic phenomena of exchange bias (EB) in bimagnetic core@shell (FiM@AFM) nanoparticles. Again utilizing the versatility of the seed-mediated modified-aminolytic method the synthesis of core@shell (FiM@AFM) nanoparticles can be studied with control over core/shell dimensions and chemical composition. Herein we will report the largest exchange field shift (H_E) in nanoparticle system, increased thermal stability of superparamagnetic nanoparticles, observe vertical shift along the magnetization axis, and

report strategies to tune exchange bias derived properties. Through synthetic design we can tune the anisotropy energy (E_A) of the ferrimagnetic and antiferromagnetic phases and additionally we can tune the interface coupling energy (E_{ex}) allowing for the fine control of EB magnetic properties. **Chapter 7** in the pursuit of understanding ferromagnetic resonance properties of spinel ferrite nanoparticles we also demonstrated the practical application of fabricated nanomagnetic films for use in communication/antennae technologies. This chapter will summarize the fabrication of these nanomagnetic films along with some results from our collaborative research pursuits with the Dr. Papapolymerou research group at Michigan State University. The novel synthesis and study of magnetic metal oxide nanocrystals has expanded our fundamental understanding of superparamagnetism, ferromagnetic resonance, spin-order in antiferromagnet nanoparticles, and interfacial exchange coupling interactions in core@shell nanostructures. Spinel ferrite nanocrystals are promising ultra-high frequency absorption materials with tunable properties capable of meeting engineering requirements. The observation of massive exchange bias shifts in core@shell ($NiFe_2O_4$@CoO) nanostructures challenges superparamagnetic limitations of magnetic nanoparticles and expands the potential of solid-state magnetic recording media.

INTRODUCTION

1.1 Background and Brief Theory of Magnetism

The initial discovery of magnetism was in naturally occurring magnetite mineral deposits known as lodestones that could attract iron. In 12th century China lodestones were harnessed to produce directional compasses to assist in navigation.[1] Despite the ancient origins of magnetism it was only relatively recently that advanced study of magnetic materials and properties flourished enabling considerable technological advancements that drive modern society. Magnetism arises from spin of unpaired electrons and their orbital angular momentum as they move around the nucleus, the collective contributions of the spin-orbit interactions yield the net magnetic moment of the material.[2, 3] Electron pairs cancels the magnetic spin contributions of the individual electrons as their spins are opposed (+/- ½) so materials with more unpaired electrons have larger magnetic moments. Crystal field theory outlines the interaction of transition metals and ligands arising from the attraction of positively charged metals cations with negatively charged ligands. The metal-ligand interactions of transition metals determine the degenerate energy levels of d-orbit electrons creating either high-spin or low-spin complexes depending on the ligand field strength. Low-spin complexes have increased energy levels between d-orbitals that encourage the preferred filling of low energy t_{2g} orbitals before higher energy e_g orbitals. High-spin complexes have reduced energy levels between d-orbitals increasing orbital degeneracy allowing increased unpaired electrons following Pauli exclusion principle.[4]

Metals, alloys, and metal oxides are the most common magnetic materials formed by intricate crystal lattices with long-range electronic and magnetic order. Crystal

structures enable spin-spin coupling between metal ions creating magnetic domains. Bulk solid-state magnetic materials are composed of multiple magnetic domains in which spin-spin coupled metal ions have magnetic ordering within the domain boundary. The net magnetic moment of a bulk material consists of the contributions of all magnetic domains.[5]

Magnetism is divided into multiple different types that describe the dominant spin-spin coupling interaction of the material. The varying types of magnetism are diamagnetism, paramagnetism, ferromagnetism, antiferromagnetism, and ferrimagnetism as illustrated in **Figure 1-1**.

1.1.1 Diamagnetism

Diamagnetism is fundamentally property of all matter in which all electrons are paired producing no net magnetic moment. When exposed to an applied magnetic field these materials a negative magnetization opposing the applied field is observed. The magnetic susceptibility of these materials is negative.

1.1.2 Paramagnetism

Paramagnetism occurs in materials with non-interacting unpaired electrons resulting in zero net magnetic moment. As the spins of a paramagnetic material are non-interacting they possess random spin orientations without long range magnetic ordering, which results in the net magnetic moment of the material to average to zero. Application of an external magnetic field would result in reorientation of the spins to partially align in the direction of the applied field. The interaction of paramagnetic spins with an applied magnetic field is subject to thermal agitation as outlined by Pierre Curie in the 1900's.[4]

Curie's Law dictates that as temperature increases the increased thermal energy disrupts the orientation of paramagnetic spins under an applied magnetic field. The temperature dependent nature of the magnetic susceptibility can be expressed as:

$$\chi = \frac{C}{T} \qquad\qquad (1\text{-}1)$$

Where C is the Curie constant of a material and T is the temperature. Curie's Law only functions for paramagnetic materials as the spins are non-interacting allowing for a simpler model.[4]

1.1.3   Ferromagnetism

Ferromagnetic materials possess a positive net magnetic moment that originates from the parallel alignment of magnetic spins, structured by the arrangement of the crystal lattice. The positive exchange interaction of magnetic spins results in a positive magnetic susceptibility and permeability exceeding one. Magnetic domain theory was originally proposed by Weiss in 1907, proposing that in bulk crystalline materials there will be separate magnetic domains possessing individual magnetic moments that interact upon each other and contribute to the net magnetic properties of the material. Upon application of an external field the magnetic domains walls could shift to lower energy orientations creating an induced magnetic moment. The presence of magnetic domains within a bulk material introduces energy barriers to magnetic spin ordering and propagates the presence of defects in the crystal structure.[5] The Heisenberg model of ferromagnetism is a quantum mechanical approach that proposes that to achieve the lowest energy exchange interaction between neighboring magnetic spins they will align in a parallel orientation.

Similarly to paramagnetic materials thermal agitation can disrupt the ordering of magnetic spins in ferromagnetic materials. The Curie temperature (T_C) is the critical temperature at which thermal energy fluctuations disrupt the exchange interaction of magnetic spins causing a magnetic phase transition from a ferromagnetic to paramagnetic state. The Curie-Wiess Law can express the temperature dependent nature of ferromagnetic materials:

$$\chi = \frac{C}{(T - \theta)} \qquad (1\text{-}2)$$

The Curie-Wiess Law is similar to the Curie Law for paramagnetic materials, but with the addition of a temperature constant (θ).[3]

1.1.4 Antiferromagnetism

Antiferromagnetic materials possess zero net magnetic moment as the result of the magnetic spins being distributed between two anti-aligned sublattices. The anti-alignment of interacting magnetic spins cancels their individual contributions yielding the zero net magnetic moment. Antiferromagnetic ordering is also subject to thermal agitation with the Néel Temperature (T_N) representing the critical temperature at which thermal energy disrupts the exchange interactions of magnetic spins.

1.1.5 Ferrimagnetism

Ferrimagnetic materials possess a unique magnetic structure in which the magnetic spins are distributed between two disproportionate anti-aligned sublattices resulting in a net positive magnetic moment. The unequal distribution of magnetic spins gives
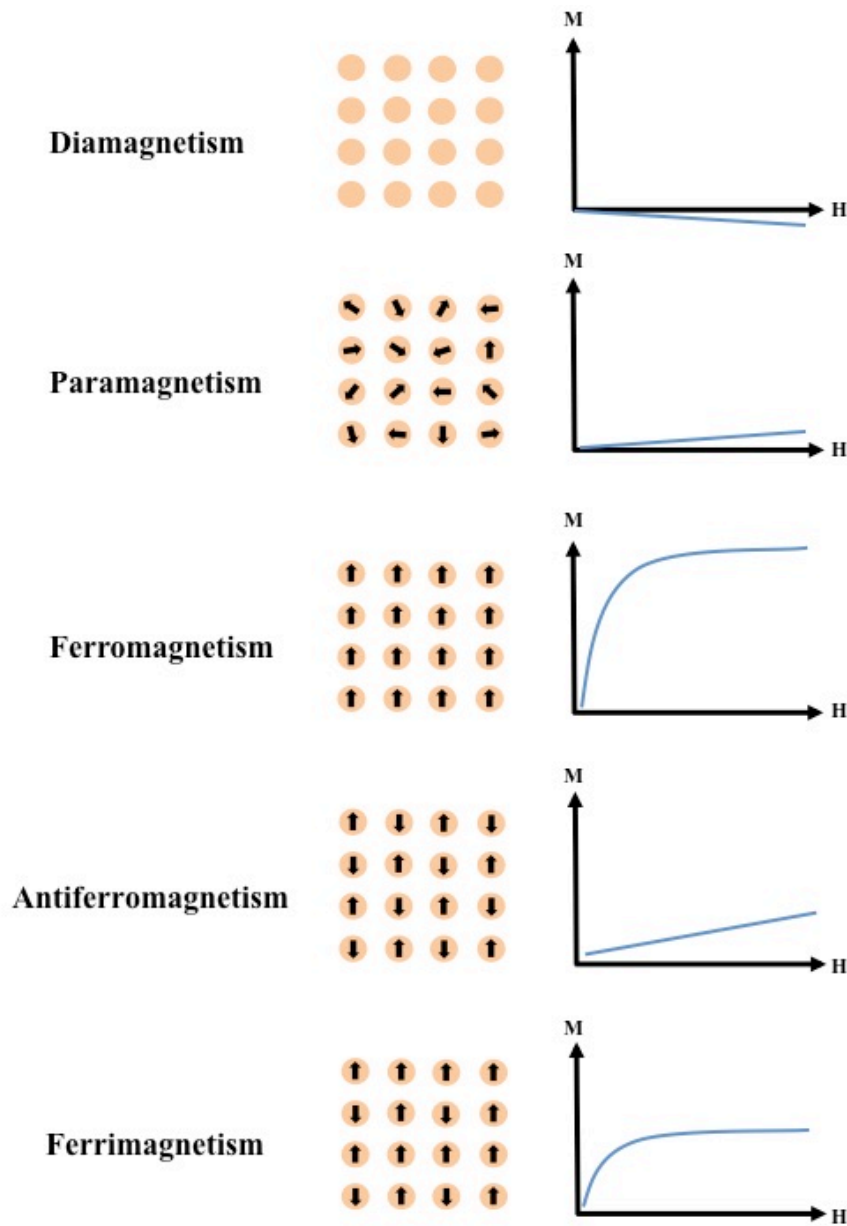
Figure 1-1: Illustration of different magnetic states including spin order and magnetic moment response to applied field.

ferrimagnetic materials microscopic antiferromagnetic spin ordering with macroscopic ferromagnetic properties such as Curie temperature and large positive magnetic susceptibility.

1.1.6 Experimental Measurements of Magnetism

Magnetic characterization of materials is performed via sensitive magnetometers such as a superconducting quantum interference device (SQUID) capable of varying the temperature and applied field strength to measure the sample response. The magnetic ordering of ferromagnetic and antiferromagnetic materials exhibit phase transitions at critical temperature points Curie and Néel temperatures respectively. The phase transitions can be determine by measuring the magnetic susceptibility of a material under a static applied magnetic field and varying the temperature, upon heating beyond the critical temperature the magnetic susceptibility will typically decrease and the increased thermal energy disrupts spin-spin coupling. In addition to temperature-dependent behavior magnetic materials will exhibit unique field-dependent properties. Field-dependent magnetic hysteresis measurements are performed on a sample at a static temperature while measurement the magnetic response to sweeping the applied field between positive and negative field strengths. Permanent magnets will exhibit a magnetic hysteresis loop at temperatures below their Curie temperature in which the magnetic moments do not return to a relaxed spin state after exposure to the applied field. A typical magnetic hysteresis loop is demonstrated in **Figure 1-2**.

Ferromagnets can be divided into hard and soft permanent magnets defined by the properties of their magnetic hysteresis loops such as coercivity, saturation, and remanent magnetizations. Coercivity (H_C) refers to the width of the hysteresis loop along the x-axis (applied field – H) and is reflective of the necessary applied magnetic field strength to flip the magnetic orientation of the sample. A hard magnet requires a strong field to reverse magnetic orientation thus possessing a large coercivity while a soft magnet is easily reversed with a small coercivity. Saturation magnetization (M_s) is the maximum magnetization achievable by the sample under an applied magnetic field. Remanent magnetization is the sample magnetization retained with zero applied field; located at the y-intercepts of the hysteresis loop.
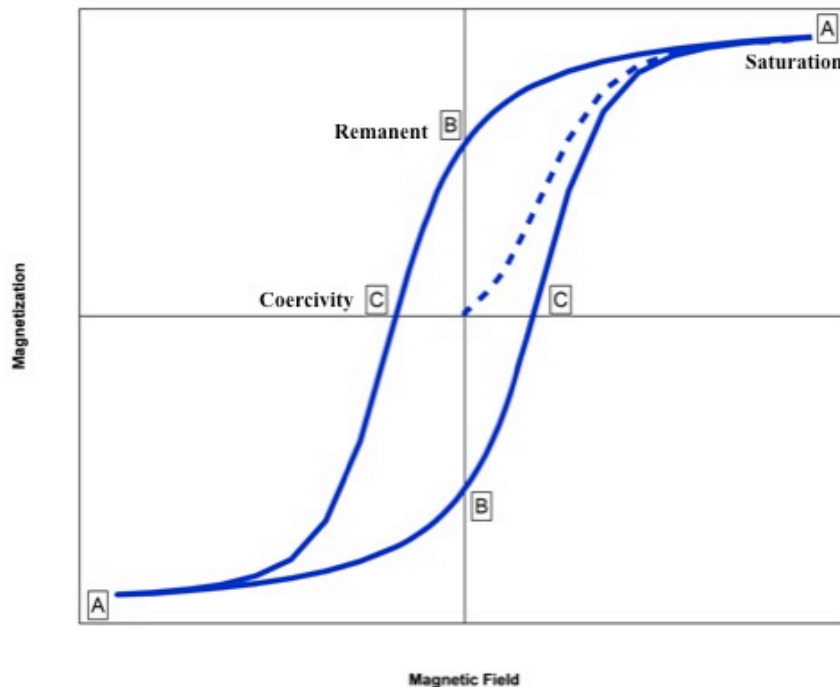
Figure 1-2: Illustration of magnetic hysteresis loop with (A) saturation, (B) remanent magnetizations, and (C) coercivity denoted.

1.2   Superparamagnetism and Magnetic Domain Theory

Magnetic domain theory was original proposed by Pierre-Ernst Weiss in 1906 to explain discrepancies observed between theoretical calculations and experimental observation of magnetic properties of solid-state bulk materials.[1, 6] Within a solid-state crystal lattice the magnetic moment of individual atoms couple to form long range magnetic ordering. This alignment of magnetic spins forms distinct magnetic domains with magnetic ordering. Bulk solid-state materials are composed of multiple magnetic domains that possess spin orientations to reduce magnetostatic energy of the system. Application of an external magnetic field can reorient the independent magnetic domains to align with the field direction, but must overcome energy barriers caused by aligning the domain spins and magnetic domain wall movement. Materials with multiple magnetic domains and domain walls are complicated to experimentally ascertain the magnetic structure of the system.
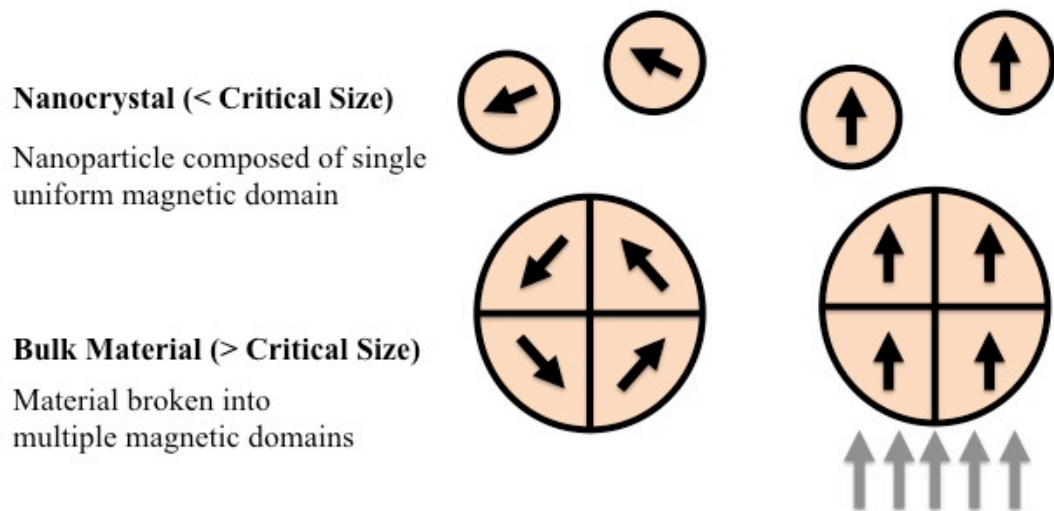
Figure 1-3: Illustration of magnetic domains in nanocrystalline and bulk materials under conditions when magnetic field is applied/not.

Reduction of crystallite grain size below a critical threshold (approximately 50 nanometers) will result in the entire crystal composing a single magnetic domain. Single domain nanocrystals have uniformed magnetic order without magnetic domain walls.[7] Experimental investigations of single domain nanocrystals can directly correlate chemical and structural alterations of a material with the impact on magnetic properties. The concept of magnetic domain walls and single domain nanocrystals is illustrated in **Figure 1-3**.

Superparamagnetism is a unique form of magnetism observed in single domain nanocrystals of ferromagnets.[7] Single domain nanocrystals possess an uniform magnetic structure with the orientation of magnetization aligning along the easy axis of magnetization. Thermal energy can disrupt the magnetic anisotropy of a nanocrystal causing the random orientation of magnetization giving the macroscopic appearance of paramagnetism. Finite-size constraints of nanocrystals reduce the thermal energy necessary to achieve transition to a paramagnetic state to occur at temperatures well below that of the bulk Curie temperature.[6] The critical temperature for this transition from ferromagnetism to superparamagnetism is known as the Blocking temperature T_B; below which single domain nanocrystals are in a "blocked" state in which their magnetic orientation is ferromagnetic in nature and above which they are "superparamagnetic" state in which thermal fluctuations cause random orientation of magnetization (paramagnetic in nature). Superparamagnetic nanocrystals have a larger magnetic susceptibility above T_B than expected of paramagnets.

Stoner-Wohlfarth model describes the behavior magnetic reversal mechanism of single domain magnetic nanocrystals:[8]

$$E_A = KV sin^2(\theta) = k_B T_B V \qquad (1\text{-}3)$$

Where E_A is the anisotropy energy of the nanoparticle, K is the magnetocrystalline anisotropy constant, V is the volume of the nanoparticle, and θ is the angle between the magnetic moment of the particle and the easy axis. This model can be adapted to access the size dependent nature of thermal fluctuations in superparamagnetic nanocrystals as shown in **equation (1-3)** where k_B is the Boltzmann constant, T_B is the blocking temperature, and V is the particle volume.[8]

1.3 Synthesis, Structure, and Applications of Magnetic Nanoparticles

Magnetic nanoparticles have been pursued for various applications including catalytic systems, data storage, biomedical imaging, drug delivery, sensors, and microelectronics.[2, 6, 9-19] For many of these applications it is essential to tune the magnetic properties through careful synthetic manipulation to control chemical composition, morphology, and crystallite size. Further understanding of the fundamental relationships between magnetic properties and microstructure is necessary to meet the emerging technological needs such as in microwave communication devices.[20-22] This thesis focuses on elucidating the complex magnetic coupling interactions through the bottom-up synthesis of novel magnetic nanoparticles such as mixed solid solutions and core@shell architectures.[23-25] These synthesized nanoparticles were characterized for their magnetic properties and evaluated for application in nanomagnetic microwave devices such as antennae, isolators, and/or circulators.[21]

1.3.1 Spinel Ferrites

Spinel ferrites are a family of ferrimagnetic metal oxides with a chemical formula AB_2O_4 in which cations occupying both the tetrahedral A sites and octahedral B sites are coordinated to close packed cubic lattice of oxygen ions. The spinel ferrite unit cell as illustrated in **Figure 1-4** consists of eight A site cations, sixteen B site cations, and 32 oxide ions. The distribution of divalent cations and trivalent iron cations between the A and B sites is dictated by the preferred coordination chemistry of the cationic species but the typical "normal" spinel structure consists of divalent A sites and trivalent iron B sites.[19] The complex distribution of cations within the crystal lattice is represented by $(M^{2+}_{1-\delta}Fe^{3+}_{\delta})_A[M^{2+}_{2-\delta}Fe^{3+}_{\delta}]_BO_4$ formulation indicating the occupancy of A and B sites. The inversion factor δ indicates the preference of a divalent cation species to occupy the B site locations of the crystal lattice forcing trivalent irons to occupy A sites.[26] Crystal field theory and synthetic approach are contributing factors to the cationic distribution.
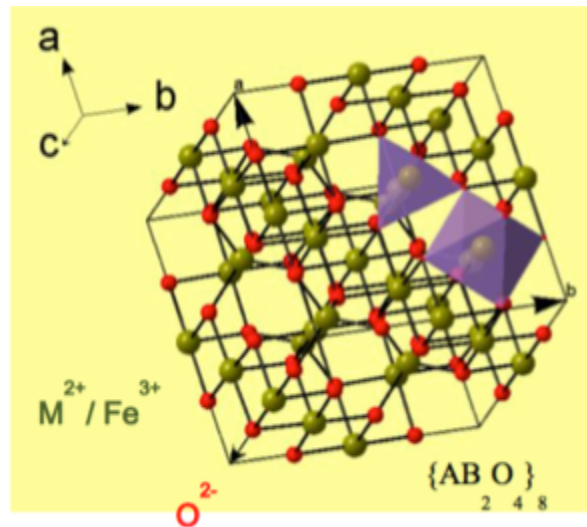
Figure 1-4: Spinel ferrite unit cell[2] (reprinted from Thesis of Dr. Daniel Sabo, Georgia Institute of Technology).

The magnetic structure arises from superexchange coupling of the A and B sites through coordinated oxygen ion intermediates. The A and B cation sites are antiferromagnetically coupled but the inequity of site populations (2B to 1A) produces a net positive magnetization and ferrimagnetic order. The net magnetization of a spinel ferrite is the contribution of the B sites minus the A sites and can be manipulated through the substitution of different divalent species ($M = Mn^{2+}$, Co^{2+}, Fe^{2+}, Ni^{2+}, Zn^{2+}, etc.) as well as the distribution of cations between A and B sites.[26] Spinel ferrites serve as a robust magnetic system that can be systematically studied for the correlation of magnetic properties to various physical and chemical properties.

1.3.2 Antiferromagnetic Metal Monoxides (CoO and NiO)

Metal monoxides with chemical formula MO ($M = Co^{2+}$ and Ni^{2+}) have a simple NaCl-type cubic crystal structure with both metals and oxide ions occupying octahedral coordination sites. The crystal lattice contains two antiferromagnetically coupled sublattices yielding a net zero magnetization.[6] Antiferromagnets are of technological interest as at temperatures below T_N they are resistant to manipulation by external magnetic fields. The natural resistance of antiferromagnets to external fields has been implemented in magnetic multilayered films to create stable field resistant magnetic moments through the exchange coupling a ferromagnet layer with an antiferromagnet layer. The spins of the antiferromagnet layer "pin" the spin of the ferromagnet through exchange coupling causing an increase in the energy barrier for the ferromagnetic spins to flip under an applied field. This concept of exchange coupled magnet multilayers revolutionized magnetic recording media in 1990 with the introduction of AMR read heads by IBM. This phenomenon enabled the miniaturization of magnetic recording media components sparking

considerable advances in electronics and computers over the decades.

1.3.3 Core@shell Architecture Nanocrystals

Core@shell architecture nanocrystals have been studied extensively to for their potential hybridized material properties and to further the fundamental the understanding of interfaced material interactions. Synthesis of core@shell architecture nanocrystals has followed two methodologies; post-synthesis surface passivation and seed-mediated epixatially growth of a shell unto a nanocrystal core (seed).[27] Surface passivation involves the synthesis of homogenous metallic nanocrystals followed by partially oxidizing the surface layers to yield a core@shell architecture with a metal core surrounded by its respective metal oxide. This technique is limited in scope, as it restricts the combination of viable materials, surface oxidation is difficult to uniformly control, and formation of voids and defects by Kirkendall Effect deteriorates the quality of the interface.[28] Seed-mediated growth is an entirely bottom-up approach, allowing for more diverse material combinations, but for epitaxially growth to occur there must be good agreement between specimen lattice parameters. The appeal of core@shell architecture in nanocrystals enables to the study of interfacial exchange interactions, surface specific phenomena, and hybridized material properties.[29]

Bimagnetic core@shell nanocrystals are a unique research medium because the high surface area to volume ratios amplifies interfacial exchange coupling between the core@shell materials. Exchange coupling is a spin-spin exchange interaction between the magnetic moments of two materials that results in a net hybridization of magnetization. Exchange coupling between magnetic multilayers has enabled application specific

tailoring of magnetic properties that has become essential to the development of modern computer and electronic devices. This thesis studies the unique magnetic properties that arise from the exchange coupling and interfacial exchange bias interactions of core@shell nanocrystals synthesized via seed-mediated growth techniques.

1.3.4   Synthesis of Metal Oxide Nanocrystals

The synthesis of novel nanomaterials has motivated decades of synthetic innovation developing techniques to overcome various challenges associated with each material. The Zhang groups' interest in further understanding the correlation between chemical composition and magnetic properties has inspired the development of a robust synthesis method for metal oxide nanocrystals. The design criteria for the synthesis method required that: 1) an industrially scalable method with affordable precursor reagents, 2) recyclable solvents to mitigate environmental impacts, 3) deft control of crystallite size and morphology, and 4) a flexible synthesis capable of producing a variety of complex chemical compositions.[30]   Thus, the aminolytic synthesis method was designed to be an affordable synthesis of chemically diverse metal oxide nanoparticles while maintaining control of crystallite size and morphology. Previous Zhang group members performed the development of this aminolytic method; this thesis will expand on their work to extend the capabilities of the aminolytic synthesis method to compounds containing nickel oxides and seed-mediated growth of core@shell architecture nanoparticles. To further establish the advantages afforded by the aminolytic method, other synthetic approaches will be highlighted.

Synthesis of nanoparticles can be divided into two groups: top-down and bottom-

up syntheses. Top-down synthesis of nanoparticles typically involves the synthesis of bulk compounds that are then physically fractured into nanometer-sized crystallites.[13] High-energy ball milling is one such approach that involves the physical mixing of stoichiometric metal oxide reagents in a ball mill that produces enough kinetic energy to chemically fuse the metal oxides together while maintaining sufficiently small crystallite sizes. This approach is energy intensive and the nanoparticle products are prone to structure defects from the abuse of ball milling. Bottom-up syntheses involve the concentrated mixing of precursor reagents while applying sufficient thermal energy to spark nucleation events that grow nanoparticles.[31] The bottom-up approach results in fewer atomic defects in the crystalline structure but the synthesis requires tailoring of reaction parameters for each unique nanoparticle composition.

Micro-emulsion synthesis is a well-studied bottom-up approach to synthesize metal oxide nanoparticles. Micelle and reverse-micelle methods are examples of micro-emulsion reactions in which the formation of micelle microreactors are utilized to control the growth of nanoparticles trapped within the micelles.[19, 32] The micelles are formed from low concentrations of long chain organic fatty acids and organic solvents being dispersed in aqueous solution.[33] Natural micelles will form in solution providing isolated nucleation and growth sites for nanoparticle formation to occur without aggregation. Micro-emulsion reactions are thermally restricted to approximately 100 °C due to the aqueous component, this thermal restriction typically means that nanoparticles formed via this method are amorphous and require further processing post-synthesis. Thermal annealing of micro-emulsion synthesized nanoparticles improves crystallinity of the sample but can result in aggregation and sintering of crystallites. Post-synthesis treatments are also detrimental to

industrial scaling as additional processes and energy input raise production costs.

Thermal decomposition synthesis is a modern approach capable of yielding high quality nanocrystals with low polydispersion. This approach utilizes the thermal decomposition of organometallic precursors to release low concentrations of metal cations in the presence of surfactants for controlled dispersion of nucleation events.[19, 34] High boiling point organic solvents are used to achieve reaction temperatures necessary for the decomposition of the organometallic precursor as well as promote nucleation and nanocrystal formation. The elevated temperatures necessary to achieve thermal decomposition also enable good crystallinity of the as-synthesized nanoparticles removing the necessity for post-synthesis treatments. The decomposition temperature of the organometallic precursors available restricts the thermal decomposition synthesis, and careful selection of compatible decomposition temperature reagents is necessary for synthesis of ternary metal oxide compositions. This restriction on organometallic precursors limits the applicability of thermal decomposition method to complex metal oxide compositions.[19]

Hydrothermal and solvothermal syntheses are not colloidal syntheses like most bottom-up approaches but instead create a gel-matrix to facilitate micrometer and nanometer sized crystals.[35, 36] Solvothermal synthesis utilizes jacketed metal pressure reactors to achieve reaction pressures and temperatures that colloidal approaches are incapable of achieving. The metal alkoxide precursors are dispersed in a polymer gel-matrix that provides a scaffold for hydrolysis reaction to form nanoparticles while preventing aggregation.[19, 37, 38] To remove the nanoparticles from the gel-matrix it is necessary to undergo calcination providing similar problems to the annealing of micro-

emulsion reactions. Nanoparticles formed by these methods are of lower quality with wide size distributions and rampant agglomeration.

Dr. Man Han of the Zhang group developed the aminolytic synthesis method improved on many aspects of the thermal decomposition method to yield a robust and versatile synthesis of metal oxide nanoparticles.[39] The primary flaw of the thermal decomposition method is its low versatility caused by the restriction of compatible decomposition temperatures of the organometallic precursors. Dr. Man Han adopted the synthesis of ZnO nanoparticles by Zhang et al. that utilized a chemically controlled release of zinc cations via the aminolysis reaction of zinc acetate with oleylamine in a high temperature organic solution.[40] Oleylamine serves dual roles in the synthesis as it both activates the release of metal cations through aminolysis reaction with the metal acetate complex and also facilitates nucleation and particle growth as a surfactant. The aminolysis reaction is the key to the versatility of the aminolytic synthesis as it enables the simultaneous release of all metal cations allowing for complex ternary and quaternary metal oxide compositions.

The aminolytic method has been extensively explored by the many members of the Zhang group to synthesize magnetic nanoparticles of diverse chemical compositions and study their complex magnetic properties. Dr. Lisa Vaughn demonstrated that the aminolytic reaction solution could be recycled upwards of ten times with little detriment to nanocrystal quality.[41] Dr. Dan Sabo studied the role of various chain length organic amines to optimize the surfactant and initiator components of the synthesis. He also showed the synthetic range of the aminolytic reaction by synthesizing cobalt ferrite, manganese ferrite, magnetite, and manganese oxide nanocrystals.[2] Dr. Wei-Ya (Helen) Chen systematically

17

synthesized $CoFe_2O_4$ nanocrystals of controlled size through carefully tuning reaction parameters of time and temperature. She also demonstrated the versatility through the synthesis or rare-earth substituted $CoFe_{2-x}M_xO_4$ nanocrystals.[42] Thanks to the dedicated work of my fellow Zhang group members, this thesis will extend the capabilities of the aminolytic synthesis to nickel oxide and nickel ferrite nanocrystals as well as to core@shell architecture nanoparticles.

1.4 **Instrumentation**

1.4.1 *Powder X-Ray Diffraction*

Powder X-ray diffraction (XRD) is a powerful analytical tool utilizing x-ray radiation to ascertain structural data of crystalline materials. Crystal structure, phase, and crystallite size can be obtained nondestructively on small samples. The instrument utilized for this work was a Bruker D8 Advance powder x-ray diffractometer with a Cu-Kα x-ray source with analysis software suites Diffrac.suite Eva and Topas 4.0. Initial diffraction pattern analysis involves Diffrac.suite Eva database comparison with known bulk material patterns from International Centre for Diffraction Data's Powder Data Diffraction Files (ICDD file number). The grain size and lattice parameters of a crystalline sample can be accessed with the Topas 4.0 software suite via the Scherrer Equation calculator.

X-ray diffraction patterns are the result of irradiating a crystalline sample with x-rays and detecting the constructive interference of reflected x-rays that satisfy Bragg's Law. For the Cu- Kα x-ray source the incident x-ray wavelength is 1.5418 Å that irradiates the crystal sample, scattering off the atoms in the unit cell. Bragg's Law describes the constructive interference of x-rays have the same angle of incident and reflection using

equation:[43]

$$n\lambda = 2d\ sin\ (\theta) \qquad\qquad (1\text{-}4)$$

Which n is the order of diffraction, λ is the incident beam wavelength, d is the interplanar

spacing, and θ is the angle of reflection/incidence. **Figure 1-5** visualizes the x-ray

interactions with crystalline solid.
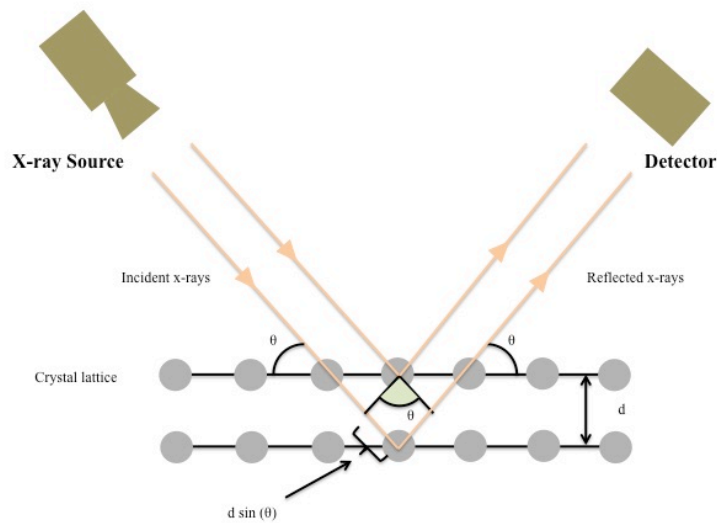
Figure 1-5: Technical description of powder X-ray diffraction instrument in which the incident beam interacts with sample crystal lattice. The beam is reflected to the detector following Braggs Law [equation (1-4)].

Powder X-ray diffraction is particularly useful technique to analyze nanoparticles through

identification of crystal phase and purity as well as to determine crystallite grain size. The

finite size constraints of nanocrystalline materials leads to broadening the well-defined

diffraction peaks observed for bulk crystal samples. Broadening can also be caused by

strains or faults in the crystal structure but, in the absence of defects, broad peaks can be

utilized to analyze crystal grain size.[44-46] Single domain nanocrystals the crystal grain size

reflects the size of the nanoparticle and can be calculated via the Scherrer equation:

$$d = \frac{K\lambda}{B\cos(\theta)} \qquad (1\text{-}5)$$

In which d is the average length (nanometers) of the distance along the diffraction vector, K is the Scherrer constant (0.9 for all calculations in this thesis), β is the full-width at half maximum (radians), λ is the incident beam wavelength, and θ is the angle of reflection/incidence (Bragg's angle).[47] The Scherrer equation is limited to samples with small crystallite size distributions. Calculations were performed with the assistance of Topas 4.0 software suite to calculate average crystal grain size for synthesized nanocrystals.

1.4.2 Total Reflection X-Ray Fluorescence

Total reflection X-ray fluorescence (T-XRF) is an elemental analysis technique that utilizes incident x-ray radiation to excite and detect fluorescence emitted from the sample. The fluorescence emissions of the sample are unique to specific elements that compose the material.[48] This technique is for surface level (approximately 80 Å) elemental analysis as the incident x-ray beam hits the sample at extreme low angle to prevent detection of
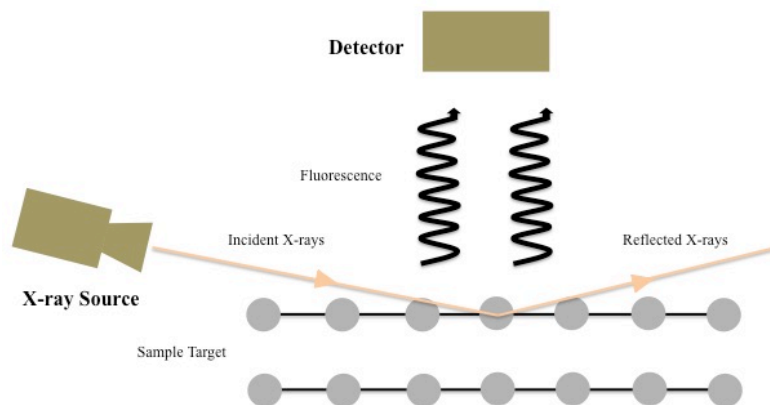
Figure 1-6: Technical description of total reflection x-ray fluorescence in which the sample is exposed to the incident beam at a low angle preventing detection of reflected x-rays. Positioning of the detector enables collection of only fluorescence radiation for elemental analysis.

reflected x-rays (**Figure 1-6**).[49] In this work samples were prepared by drop casting

nanocrystals dispersed in ethanol unto the silica sample wafer and allowed to dry. T-XRF

functioned well for the samples because of the small grain size and homogenous nature of

the mixed solid solution nanocrystals.

1.4.3   Superconducting Quantum Interference Device (SQUID) Magnetometer

Superconducting Quantum Interference Device MPMS-5S, affectionately known

as SQUID, is a highly sensitive magnetometer with a resolution of 10^{-11}G. The high

sensitivity of the SQUID detector is ideal for measuring magnetic moments in weakly

magnetic samples such as nanocrystals and organometallic complexes. The MPMS-5S

magnetometer is capable of producing applied fields ranging from -5 to 5 Telsa and

achieving stable temperatures as low as 1.8 K. The powerful applied fields are produced

by the SQUID's superconducting coil that necessitates liquid helium cooling to maintain superconducting properties. The liquid helium reserve also serves as coolant source for low temperature measurements.

SQUID magnetometers are designed around a SQUID detection coil system composed of a superconducting coil with one to two Josephson junctions (**Figure 1-7**).[50] The Josephson junction is constructed of two superconducting materials separated by an insulating barrier, the current that passes across the barrier is the Josephson current. When operated at near 0 K the Josephson current is extremely sensitive to magnetic fluctuations, a property exploited to measure the magnetic moment of a sample. The sample is moved with respect to the detection coil, the magnetic field fluctuations with respect to the detecting coil induces a measurable current in the Josephson junction. The magnetic moment of the sample is directly proportional to the current alterations in the SQUID.
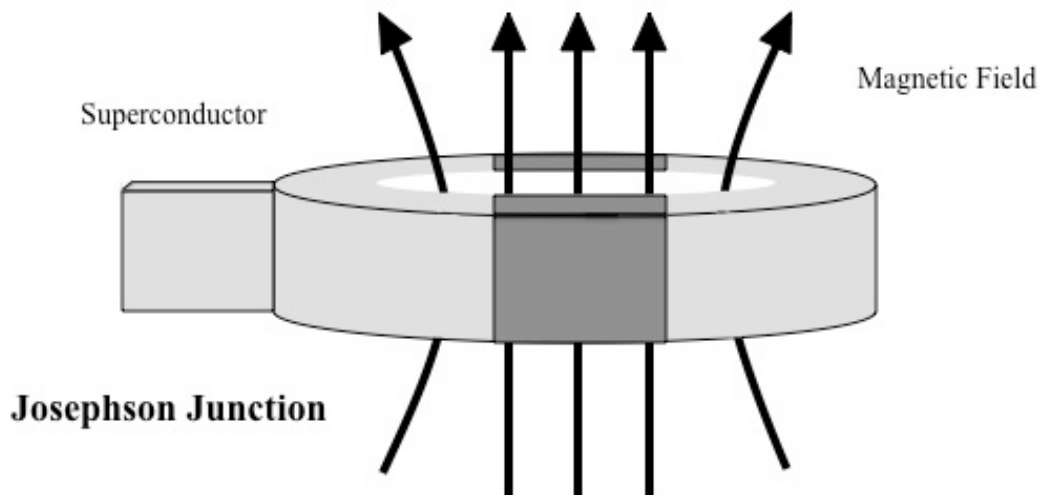
Figure 1-7: Technical description of superconducting Josephson Junction for SQUID magnetometer.

Sample preparation for SQUID measurements typically involves the careful measurement of a powder sample into a gelatin capsule. Hysteresis measurements require powder samples to be stabilized by dispersing the powder sample in Icosane ($C_{20}H_{42}$) to prevent physical movement induced by alternating magnetic fields. The gelatin capsule is assembled to encapsulate the powder sample and sealed with Kapton tape. The assembled capsule is inserted into a plastic straw and suspended at a predetermined height. The straw is sealed at the bottom end with Kapton tape and ventilation holes are made above and below the capsule to stabilize the sample under vacuum conditions of the SQUID sample chamber. The top end of the straw is attached to the sample rod with Kapton tape, the sample is now ready to be inserted into the sample chamber airlock. The sample chamber is maintained at approximately 4.24 K under a vacuum to protect it from atmospheric O_2 and N_2 that would freeze at low temperatures causing blockages.[2]

This thesis will focus primarily on two types of measurements: temperature dependent magnetic susceptibility and field-dependent magnetic hysteresis. Temperature dependent magnetic susceptibility measures the magnetic response of a sample with respect to temperature changes (5 – 310 K) under a stable applied field (100 G). The magnetic susceptibility measurements will be reported in units of emu/g•G, with the magnetization (M) as a function of the sample mass (g) and applied field (G). Temperature dependent magnetic susceptibility measurements reveal critical temperatures of magnetic phase transitions such as Curie, Néel, and/or blocking temperatures. Field-dependent magnetic hysteresis measurements involve maintaining the sample at a stable temperature (5 or 300 K) while measuring the magnetic response to an alternating applied magnetic field from sweeping from 5 to -5 T. The magnetic hysteresis reveals field-dependent sample

properties of coercivity (G), saturation, and remanent magnetizations (emu/g). Superparamagnetic nanocrystals will exhibit reduced field-dependent properties at temperatures greater than the T_B. This thesis utilizes the SQUID to systematically study the magnetic properties of all synthesized samples to determine the correlations between chemical composition and magnetism.

1.4.4   Ferromagnetic Resonance Spectroscopy

Ferromagnetic resonance (FMR) spectroscopy is a technique to measure the magnetization of ferromagnets through exposing the sample to high frequency (microwaves) electromagnetic waves under an applied magnetic field. Coupling between the magnetic moment of the sample and the incident electromagnetic wave induces absorption by the ferromagnet resulting in resonance and the electromagnetic wave losing power.[4] The magnetization of the ferromagnetic sample possesses an intrinsic precession frequency that must be matched by the incident wave for coupling to occur.[51] The precession frequency is unique to the magnetic structure of the material so induced
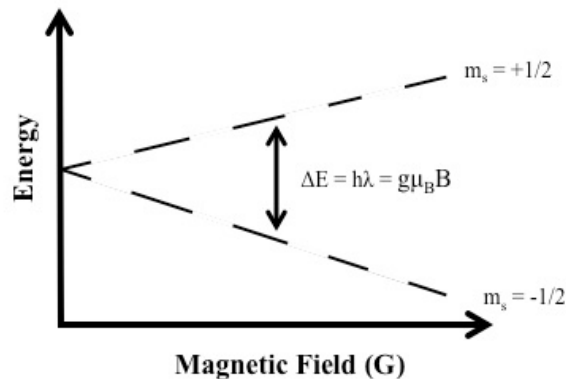
Figure 1-8:   Zeeman field splitting, fundamental excitation mechanism of ferromagnetic resonance spectroscopy

24

resonance will generate a unique ferromagnetic resonance spectrum. Microwave devices such as isolators, circulators, and antennae operate under the principle of ferromagnetic resonance to absorb high frequency signals.

The power loss of the incident wave is absorbed by the ferromagnet can be explained through Zeeman splitting of electron spins:

$$\Delta E = h\nu = g\mu_B H_0 \tag{1-6}$$

In which ΔE is the energy absorbed from the incident wave, h is plank's constant, ν is the frequency of the incident wave, g is the electron g-factor, μ_B is the Bohr Magneton, and H_0 is the applied magnetic field.[4] Zeeman Effect is further illustrated in **Figure 1-8**.
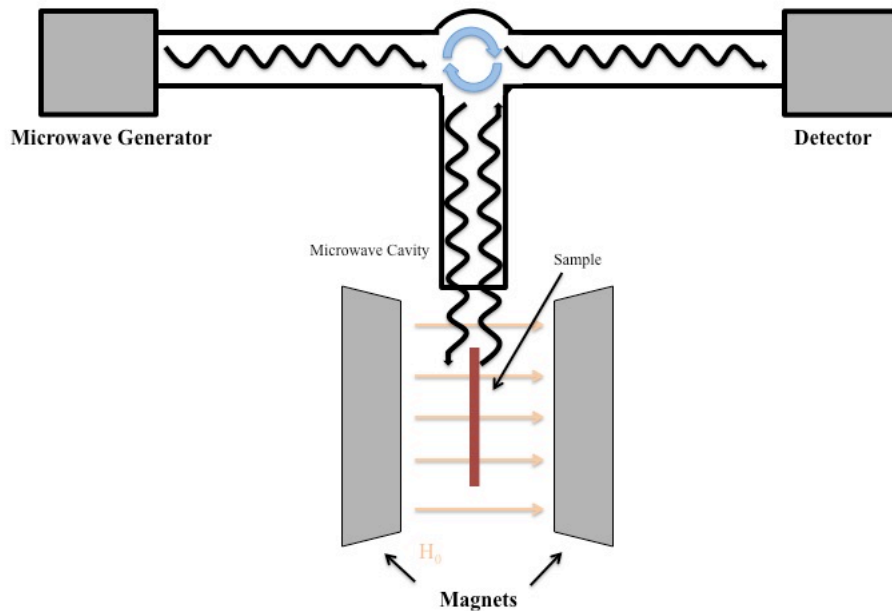
Figure 1-9: **Technical description of electron paramagnetic resonance spectrometer/ferromagnetic resonance spectrometer.**

In this work the FMR experiments were performed with a X-band frequency Bruker EMX spectrometer operating at 9.88 GHz (**Figure 1-9**). FMR experiments are conceptual similar and can utilize instruments designed for electron paramagnetic resonance (EPR) spectroscopy where microwaves excite unpaired electrons under an applied magnetic field. As the X-band instrument has a set frequency (9.88 GHz) the applied magnetic field was swept from 500 to 10,000 G. Resonance condition can be met through increasing the applied magnetic field until the precision frequency matched the incident wave. Samples were prepared by dispersing 1-10 w/w% nanoparticles in KCl with a mortar and pestle. The resonance field (G) and linewidth (G) can be derived from the first derivative of the absorption spectra.[42]

Magnetic materials are critical components to the function of modern electronic devices from producing electric current in generators, magnetic recording media for computers and phones, to communication applications including cellular data and wifi. The increasing interconnected nature of modern society has driven the development of ever-more powerful compact electronic devices that conveniently meet our daily needs. Nanoscale barriers such as "superparamagnetic limitations" obstruct this march of progress toward miniaturized devices and their essential magnetic components. Superparamagnetism is manifest as lowered thermal stability of single domain magnetic nanocrystals, these thermal fluctuations disrupt the magnetic ordering of the material yielding a macroscopic paramagnetic state. This nanoscale phenomena is at odds with innovation in consumer microelectronics by restricting the miniaturization of key magnetic components.

1.5 REFERENCES

1.   Jiles, D. C., Introduction to Magnetism and Magnetic Materials, Third Edition. *CRC Press* **2015**, 588.

2.   Sabo, D. E., Novel Synthesis of Metal Oxide Nanoparticles via the Aminolytic Method and the Investigation of Their Magnetic Properties. **2012**, 158.

3.   O'Handley, R. C., Modern Magnetic Materials: Principles and Applications. *John Wiley & Sons, INC.* **2000**, 764.

4.   Kittel, C., Introduction to Solid State Physics, 8th Edition. *John Wiley & Sons, INC.* **2004**, 704.

5.   McCurrie, R. A., Ferromagnetic Materials: Structure and Properties. *Academic Press.* **1994**, 292.

6.   Kodama, R. H., Magnetic nanoparticles. *J Magn Magn Mater.* **1999,** *200*, 359-372.

7.   Bedanta, S.; Kleemann, W., Supermagnetism. *J Phys D: Appl Phys.* **2009,** *42*, 1-28.

8.   Tannous, C.; Gieraltowski, J., The Stoner–Wohlfarth model of ferromagnetism. *Eur J Phys* **2008,** *29* (3), 475-487.

9.   Young-Wook Jun, J.-W. S., Jinwoo Chen, Nanoscaling Laws of Magnetic Nanoparticles and Their Applicabilities in Biomedical Sciences. *Acc Chem Res.* **2007,** *41* (2), 179-189.

10.   Obaidat, I. M.; Issa, B.; Haik, Y., Magnetic Properties of Magnetic Nanoparticles for Efficient Hyperthermia. *Nanomaterials (Basel)* **2015,** *5* (1), 63-89.

11.   Issa, B.; Obaidat, I. M.; Albiss, B. A.; Haik, Y., Magnetic nanoparticles: surface effects and properties related to biomedicine applications. *Int J Mol Sci* **2013,** *14* (11), 21266-305.

12.   Koh, I.; Josephson, L., Magnetic nanoparticle sensors. *Sensors (Basel)* **2009,** *9* (10), 8130-45.

13.   Laurent, S., Forge, D., Port, M., Roch, A., Robic, C., Vander Elst, L., Muller, R. N., Magnetic Iron Oxide Nanoparticles: Synthesis, Stabilization, Vectorization, Physicochemical Characterizations, and Biological Applications. *Chem Rev* **2008,** *108*, 2064-2110.

14.   Jang, J. T.; Nah, H.; Lee, J. H.; Moon, S. H.; Kim, M. G.; Cheon, J., Critical enhancements of MRI contrast and hyperthermic effects by dopant-controlled magnetic nanoparticles. *Angew Chem Int Ed Engl* **2009,** *48* (7), 1234-8.

15.   David R. Baselt, G. U. L., Mohan Natesan, Steven W. Metzger, Paul E. Sheehan, Richard J. Colton, A Biosensor Based on Magnetoresistance Technology. *Biosens Bioelectron.* **1998,** *13*, 731-739.

16.   M Lorenz, M. S. R. R., T Venkatesan, E Fortunato4,; P Barquinha, R. B., D Salgueiro, R Martins, E Carlos, A Liu, F K Shan, M Grundmann, H Boschker, J Mukherjee, M Priyadarshini, N DasGupta, D J Rogers, F H Teherani, E V Sandana, P Bove,; K Rietwyk, A. Z., A Veziridis, A Weidenkaff, M Muralidhar,; M Murakami, S. A., J Fompeyrine, J Zuniga-Perez, R Ramesh,; N A Spaldin, S. O., V Borisov, I Mertig, V Lazenka,; G Srinivasan, W. P., M Uchida, M Kawasaki, R Pentcheva,; P Gegenwart, F. M. G., J Fontcuberta and N Pryds, The 2016 Oxide Electronic Materials and Oxide Interfaces Roadmap. *J Phys D: Appl Phys.* **2016,** *49*, 1-54.

17.   Na, H. B.; Song, I. C.; Hyeon, T., Inorganic Nanoparticles for MRI Contrast Agents. *Adv Mater.* **2009,** *21* (21), 2133-2148.

18.   Polshettiwar, V.; Luque, R.; Fihri, A.; Zhu, H.; Bouhrara, M.; Basset, J. M., Magnetically recoverable nanocatalysts. *Chem Rev* **2011,** *111* (5), 3036-75.

19.   Kefeni, K. K.; Msagati, T. A. M.; Mamba, B. B., Ferrite nanoparticles: Synthesis, characterisation and applications in electronic device. *Mater Scin Eng: B* **2017,** *215*, 37-55.

20.   J. Y. Shin, J. H. O., The Microwave Absorbing Phenomena of Ferrite Microwave Absorbers. *IEEE Trans Magn.* **1993,** *29* (6), 3437-3439.

21.   Özgür, Ü.; Alivov, Y.; Morkoç, H., Microwave ferrites, part 1: fundamental properties. *J Mater Sci: Mater Electron.* **2009,** *20* (9), 789-834.

22.   Pardavi-Horvath, M., Microwave Applications of Soft Ferrites. *J Magn Magn Mater.* **2000,** *215*, 171-183.

23.   Song, Q.; Zhang, Z. J., Controlled synthesis and magnetic properties of bimagnetic spinel ferrite $CoFe_2O_4$ and $MnFe_2O_4$ nanocrystals with core-shell architecture. *J Am Chem Soc* **2012,** *134* (24), 10182-90.

24.   Granados-Miralles, C.; Saura-Muzquiz, M.; Andersen, H. L.; Quesada, A.; Ahlburg, J. V.; Dippel, A. C.; Canevet, E.; Christensen, M., Approaching Ferrite-Based Exchange-Coupled Nanocomposites as Permanent Magnets. *ACS Appl Nano Mater* **2018,** *1* (7), 3693-3704.

25.   Song, Q.; Zhang, Z. J., Correlation between Spin-Orbital Coupling and the Superparamagnetic Properties of Magnetite and Cobalt Ferrite Spinel Nanocrystals. *J Phys Chem B.* **2006,** *110*, 11205-11209.

26.   Pacakova, B.; Kubickova, S.; Reznickova, A.; Niznansky, D.; Vejpravova, J., Spinel Ferrite Nanoparticles: Correlation of Structure and Magnetism. In *Magnetic Spinels - Synthesis, Properties and Applications*, 2017.

27.   Hartmut Zabel, S. D. B., Magnetic Heterostructures. *Springer Tracts in Modern Physics* **2008**.

28.   Anderson, B. D., Tracy, J.B., Nanoparticle Conversion Chemistry: Kirkendall Effect, Galvanic Exchange, and Anion Exchange. *Nanoscale* **2014,** *6* (21), 12195-12217.

29.   Saha, A.; Viswanatha, R., Magnetism at the Interface of Magnetic Oxide and Nonmagnetic Semiconductor Quantum Dots. *ACS Nano* **2017,** *11* (3), 3347-3354.

30.	Nguyen, T. D., Do, T.O., Size- and Shape-Controlled Synthesis of Monodisperse Metal Oxide and Mixed Oxide Nanocrystals. *Nanocrystal*, 56-87.

31.	Cushing, B. L., Kolesnichenko, V.L., O'Connor, C.J., Recent Advances in the Liquid-Phase Syntheses of Inorganic Nanoparticles. *Chem Rev* **2004,** *104*, 3893-3946.

32.	Liu, C., Zou, B., Rondinone, A.J., Zhang, Z.J., Reverse Micelle Synthesis and Characterization of Superparamagnetic $MnFe_2O_4$ Spinel Ferrite Nanocrystallites. *The J Phys Chem B.* **2000,** *104* (6), 1141-1145.

33.	Moumen, N., Pileni, M.P., New Syntheses of Cobalt Ferrite Particles in the Range 2-5 nm: Comparison of the Magnetic Properties of the Nanosized Particles in Dispersed Fluid or in Powder Form. *Chem. Mater.* **1996,** *8*, 1128-1134.

34.	Lang, F.; Sun, D.; Liu, J.; Wang, H.; Yan, H., Improved size-tunable synthesis of monodisperse NiO nanoparticles. *Mater Lett.* **2016,** *181*, 328-330.

35.	Huang, F., Zhang, H., Banfield, J. F., Two-Stage Crystal-Growth Kinetics Observed during Hydrothermal Coarsening of Nanocrystalline ZnS. *Nano Letters* **2003,** *3* (3), 373-378.

36.	Komarneni, S., Li, Q., Roy, R., Microwave-hydrothermal processing of layered anion exchangers. *J Mater Res.* **1996,** *11* (8), 1866-1869.

37.	Sutka, A.; Mezinskis, G., Sol-gel auto-combustion synthesis of spinel-type ferrite nanomaterials. *Front Mater Sci.* **2012,** *6* (2), 128-141.

38.   Beach, E. R.; Shqau, K.; Brown, S. E.; Rozeveld, S. J.; Morris, P. A., Solvothermal synthesis of crystalline nickel oxide nanoparticles. *Mater Chem Phys.* **2009,** *115* (1), 371-377.

39.   Han, M. H., Development of Synthesis Method for Spinel Ferrite Magnetic Nanoparticle and Its Superparamagnetic Properties. **2008**, 181.

40.   Zhang, Z.; Zhong, X.; Liu, S.; Li, D.; Han, M., Aminolysis route to monodisperse titania nanorods with tunable aspect ratio. *Angew Chem Int Ed Engl* **2005,** *44* (22), 3466-70.

41.   Vaughan, L. A., Enviromentally Benign Synthesis and Applications of Some Spinel Ferrite Nanoparticles. **2011**, 164.

42.   Chen, H. W., Aminolytic Synthesis and Ferromagnetic Resonance of Cobalt and Manganese Based Spinel Ferrite Nanoparticles. **2018**, 148.

43.   Klug, H. P., Alexander, L. E., X-Ray Diffraction Procedures: For Polycrystalline and Amorphous Materials, 2nd Edition. *John Wiley & Sons, INC.* **1974**, 992.

44.   Skoog, D. A., Holler, F.J., Crouch, S.R., Principles of Instrumental Analysis. *Cengage Learning.* **2018**, 992.

45.   Wang, Z. L., Liu, Y., Zhang, Z., Handbook of Nanophase and Nanostructured materials. *Springer US.* **2002**, 1-406.

46.   Ingham, B., X-ray scattering characterisation of nanoparticles. *Crystallography Reviews* **2015,** *21* (4), 229-303.

47.   Cullity, B. D., Stock, S.R., Elements of X-Ray Diffraction, Third Edition. *Pearsons.* **2001**, 696.

48.   Dalipi, R.; Margui, E.; Borgese, L.; Depero, L. E., Multi-element analysis of vegetal foodstuff by means of low power total reflection X-ray fluorescence (TXRF) spectrometry. *Food Chem* **2017,** *218*, 348-355.

49.   Klockenkaemper, R., von Bohlen, A., Elemental Analysis of Envirnomental Samples by Total Reflection X-Ray Fluorescence: A Review. *X-Ray Spectrometry* **1996,** *25*, 156-162.

50.   Schmelz, M.; Vettoliere, A.; Zakosarenko, V.; De Leo, N.; Fretto, M.; Stolz, R.; Granata, C., 3D nanoSQUID based on tunnel nano-junctions with an energy sensitivity of 1.3 h at 4.2 K. *Appl Phys Lett.* **2017,** *111* (3).

51.   Von Sovskii, S. V., Ferromagnetic Resonance: The Phenomenon of Resonant Absorption of a High-Frequency Magnetic Field Ferromagnetic Substances. *Elsevier*, *LTD*. **2016**, 1-340.

CHAPTER 2. MODIFIED-AMINOLYTIC SYNTHESIS OF NICKEL FERRITE NANOCRYSTALS AND THEIR SIZE-DEPENDENT MAGNETIC PROPERTIES

2.1   Introduction

Magnetic nanoparticles have been extensively studied for decades to investigate aspects of fundamental magnetism with technological applications including magnetic recording media, biosensors, drug delivery, catalysis, chemical separation, telecommunications, and spintronics.[1-5] The pursuit of novel nanomaterials has driven the development of robust colloidal synthetic methods capable of versatile high-yield syntheses that maintain control of crystallite size and chemical composition. Spinel ferrites (MFe_2O_4) are a class of chemically stable magnetic nanomaterial in which superexchange coupling within the crystal lattice yields a ferrimagnetic order.[6-8] Through the synthesis of high quality metal oxide nanocrystals we are able to study a plethora of nanoscale magnetic phenomena that include superparamagnetism, ferromagnetic resonance, spin-glass states, magnetic exchange coupling, and exchange bias.[9]

Nanoscale spinel ferrites have been the subject of extensively research due to their unique magnetic properties that includes size-dependent blocking temperature, chemical stability, and composition-dependent magnetocrystalline anisotropy and coercivity.[10] The ability to modify their magnetic properties through chemical substitutions makes them ideal candidates for a variety of applications including magnetic recording media,

biomedical sensors, drug delivery, chemical separation, and telecommunications. The growing industrial relevance of magnetic nanoparticles has inspired the development of versatile yet high-yield synthesis method to produce high quality nanocrystals without sacrificing efficiency. Amongst spinel ferrite nanomaterials $NiFe_2O_4$ have proven to be ostensibly difficult to synthesize and research as limited studies have investigated $NiFe_2O_4$ nanocrystals grown from a bottom-up synthetic approach. Nickel ferrite is of interest as it possesses high permeability, low electrical resistivity have been exploited in high frequency electronic components for decades. Modern technological demands expanding it incentives improving our understanding of ultrahigh frequency microwave materials through the synthesis and study of nanocrystalline samples.

Synthetic techniques of nanoscale materials vary wildly in versatility and quality and include methods such as sol-gel, hydrothermal, micelle, and thermal decomposition. Sol-gel and hydrothermal methods yield nanoparticles with high poly-disparity and are subject to high-energy cost to achieve the necessary reaction temperature and pressure.[11] The development of colloidal synthesis techniques such as micelle and thermal decomposition enable isolated nucleation events enabling control of crystallite size and avoiding aggregation. Colloidal synthesis techniques follow the La Mer model of nanocrystal nucleation and growth.[12] The thermal decomposition method is capable of yielding high quality nanocrystals but is limited by the selection of organometallic precursors. To synthesize spinel ferrites and other complex chemical compounds require the simultaneous release of metal cations into solution or independent nucleation events with yield a mixture of products. The reliance on the thermal decomposition of the

35

organometallic precursors severely limits the synthesis of materials to complimentary decomposition temperatures.

In the endeavor to develop high-yield synthetic method the Zhang group developed the aminolytic method capable of the controlled synthesis of spinel ferrite nanocrystals of variable size and chemical compositions. The aminolytic method was modified from the synthesis of ZnO nanoparticles.[13, 14] The aminolytic method deviates from other colloidal synthesis methods by chemically controlling the release of metal cations into solution through the aminolysis reaction of oleylamine with the metal acetate precursor. The chemical initiation of the aminolytic reaction enables the substitution of various metal acetate precursors allowing the synthesis of complex compositions of spinel ferrite nanocrystals. The metal acetate precursors also enable a diverse selection of chemical compositions through their preparation different stoichiometry of mixed metal acetates can be utilized to synthesize complex metal oxide nanocrystals involving 4+ metal cations incorporated into the spinel ferrite product.[7, 8]

The spinel ferrite crystal lattice is divided into two sublattices with one composed of metal cations in either the tetrahedral A sites or octahedral B sites in which both are coordinated to oxygen ions.[7] Superexchange coupling between the A-B sublattices produces net ferrimagnetic order within the spinel ferrite lattice that can be tuned through the chemical substitution of metal cations or through redistribution cation site occupancy.[13] The ferrimagnetic ordering of spinel ferrites allows for deft control of the magnetic properties through chemical substitution creating an ideal model system to study correlations of fine magnetic alterations.

Microwave ferrites are a family of microwave absorbing materials that includes spinel ferrites, hexaferrites, and garnets.[4] Due to their absorption of ultra-high frequency microwaves, these ferrites have been extensively utilized in radar and antenna applications. Amongst these materials nickel-based spinel ferrites are of high interest due to their high resonance frequency, high resistivity, low permeability.[15, 16] High power transformer cores are composed of $Ni_{1-x}Zn_xFe_2O_4$ as a high frequency absorption material to dissipate energy. Herein, we demonstrate the modification of the aminolytic synthetic method to yield high quality $NiFe_2O_4$ nanocrystals that were investigated for their ferromagnetic resonance and size-dependent magnetic properties.

2.2 Experimental

2.2.1 Synthesis of Metal Acetate Precursors

Metal acetate precursors for the aminolytic method were synthesized through the reaction of metal hydroxides with acetic acid. A typical preparation for $NiFe_2O_4$ synthesis begins by dissolving a 1:2 ratio of metal salts such as $NiCl_2 \bullet 6(H_2O)$ (6 mmol) and $FeCl_3$ (12 mmol) in 150 mL of DI water while vigorously stirred. Once all the metal salts are dissolved in solution, 150 mL of 5 M NaOH solution was added causing the precipitation of metal hydroxide complexes, the solution was stirred for 2 hours. The metal hydroxide mixture was collected via centrifugation; the mixture was washed 4 times with DI water to remove excess NaOH and Na^+ from the solid mixture. The metal hydroxide mixture was transferred to a 1000 mL beaker with stir bar, approximately 200 mL of glacial acetic acid was added dissolving the metal hydroxides. Stir the solution overnight while applying 100°C heat to promote the formation of metal acetates while removing excess moisture.

The dried metal acetate mixture was collected the following day, and ground with mortar and pestle to promote thorough mixing of the metal acetate precursors in the desired stoichiometric ratio. This method can be adapted to create mixtures of multiple metal acetates in varying molar ratios as well as single metal acetates such as Fe(III)acetate.

2.2.2   Modified Aminolytic Method

The aminolytic method can be utilized to synthesize a diverse composition of metal and metal oxide nanoparticles depending on adjustment of the reaction parameters. In order to synthesis metal oxide nanoparticles composed of Ni(II) cations, the aminolytic method was modified to incorporate an oxygen enriched atmosphere in substitution for the typical argon; this procedure is termed the modified aminolytic method. The synthesis of $NiFe_2O_4$ nanocrystals is accomplished through the modified aminolytic method as described. A three-neck round bottom flask equipped with stir bar in which the metal acetate precursor mixture was added [1:2 ratio of Ni(II):Fe(III)] (12 mmol), additionally 20 mL of oleylamine and 60 mL of dibenzyl ether were added. The three-neck round bottom flask was equipped with a thermometer, reflux condenser, and gas line, and placed into a heating mantle set upon a magnetic stir plate. Once the reaction preparation was completed, the reaction mixture was heated to 140°C for 1 hour at temperature while stirred. After 1 hour at temperature the oxygen gas flow was introduced and the reaction temperature was increased to 240°C for 2 hours with stirring. The reaction vessel was allowed to cool to room temperature and the synthesized nanoparticles were collected by washing the reaction mixture with a 50/50 solution of ethanol/hexane into a 1,000 mL beaker. The nanoparticles were collected with a strong permanent magnet and the organic solution was decanted off, the nanoparticles were washed of excess surfactant and organic

solvents by repeated washes with ethanol (190 proof) and collected via magnet. The nanoparticles were allowed to dry overnight then ground with mortar and pestle to achieve a fine powder of magnetic $NiFe_2O_4$ nanocrystals. Reaction parameters such as temperature, time, and atmosphere can be adjusted to acquire desired physical properties of the product nanoparticle such as the crystallite size, morphology, or oxidation state.

2.2.3   Instrumentation

Powder x-ray diffraction (XRD) patterns were obtained with a Bruker D8 Advance Powder X-ray Diffractometer with a copper Kα source across a 15-85º 2θ angle. Phase analysis matching was performed with EVA software suite to confirm crystal structure of synthesized particles. Nanoparticle crystallite size was analyzed with TOPAS 4.0 software suite through the average peak broadening analysis via the Debye-Scherrer equation. Total reflection x-ray fluorescence was utilized for elemental analysis of nanoparticles performed on a Bruker S2 PICOFOX with a molybdenum Kα. Samples were prepared by dilute suspension of nanoparticle sample in hexane with 2 w/w% gallium standard was drop cast onto the sapphire sample plate. The ratio of peak signals of divalent species to iron was used to determine the stoichiometry of the sample. Thermogravimetric analysis (TGA) was performed with a Perkin Elmer TGA-7 with temperature ranging from 25 ºC to 400ºC with a ramp rate of 5ºC/min to determine the weight loss that can be attributed to organic surface ligands. Transmission electron microscopy (TEM) was performed on JEOL 100 CX2 at 100 kV, samples were prepared by dilute suspension of nanoparticle samples into hexane then drop casting onto the copper grid. Sample batches were analyzed for nanoparticle size, polydisparity, and morphology.

Magnetometry measurements were performed with the Quantum Design MPMS-5S Superconducting Quantum Interference Device (SQUID) capable of achieving fields $\pm$ 5 Telsa with temperatures ranging from 2 to 350 K. SQUID samples were prepared by weighing 5-20 mg of nanoparticles into a gelatin capsule, sealed with Kapton tape, suspended in a plastic straw, and then attached to the sample rod with Icosane wax used to stabilize samples for hysteresis measurements. Magnetic susceptibility (both zero-field cooled ZFC and field-cooled FC) measurements were typically performed from 5 to 305 K under an applied field 100 G. Hysteresis measurements were ZFC and performed at 5 K with the applied field alternating between $\pm$ 5 Telsa. Ferromagnetic resonance spectroscopy measurements were performed on a X-band frequency Bruker EMX spectrometer. Samples were prepared by diluting nanoparticle samples by thoroughly grinding in 2 w/w% particles in KCl then depositing in sample tube. Ferromagnetic resonance profiles were obtained at room temperature, χ = 9.88 GHz, and sweeping the Hall field from 250 to 10,000 Oe.

2.3   Results and Discussion

The aminolytic method has been demonstrated to provide for the controlled synthesis of metal oxide nanocrystals of variable size and chemical composition. Unfortunately the reductive nature of the oleylamine that serves as chemical initiator and surfactant causes the reduction of metal cations such as Ni(II) and Cu(II) to form metallic nanoparticles. The reduction limits the versatility of the aminolytic method requiring modification to enable the synthesis of nickel-based spinel ferrites. The argon atmosphere of the aminolytic method serves to remove atmospheric oxygen and H_2O from the reaction vessel preventing the formation of oxidation prone side products. The modification of the

reaction atmosphere through substitution of argon for oxygen in the synthesis of nickel ferrites prevents reduction of Ni(II) cations in solution. This small modification enables the synthesis of NiO, $NiFe_2O_4$, and various compositions of $Ni_{1-x}M_xFe_2O_4$ nanocrystals, allowing the study and synthesis of highly crystalline superparamagnetic $NiFe_2O_4$ nanocrystals for the first time.

Atmospheric control of the reaction conditions enables further modification of reaction conditions and increased control over the synthetic method. An unexpected consequence of the oxygen-rich atmosphere causes an increased binding affinity of the oleylamine surfactant to the nanocrystal surface (**Figure 2-3**). As shown in **Figure 2-1** through thermogravimetric analysis (TGA) of 6 nm $CoFe_2O_4$ nanocrystals synthesized under both reaction conditions demonstrates a stark increase of nearly 2-fold in organic surfactant from only 80 w/w% under argon to 55 w/w% on the surface of the modified
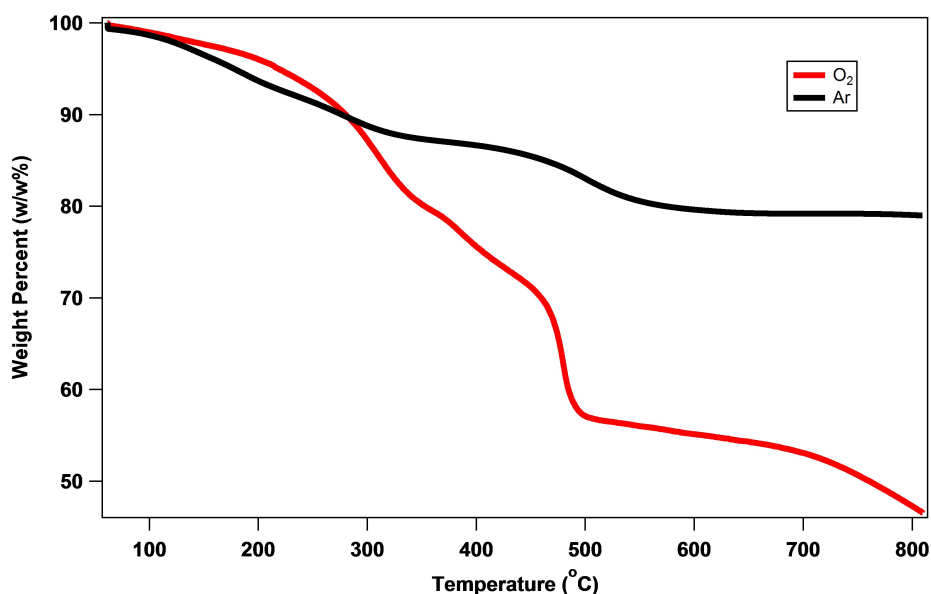
Figure 2-1: Thermogravimetric analysis of CoFe₂O₄ nanocrystals synthesized via the aminolytic with argon atmosphere and modified aminolytic with oxygen atmosphere methods of similar crystal size (6.0 nm diameter)

aminolytic synthesis. This results in reduction of the nanocrystal growth phase allowing for fine size control of 4-6 nm spinel ferrite nanocrystals under the modified atmospheric conditions. In order to increase the crystallite size beyond this narrow threshold seed-mediate aminolytic synthesis was adapted by repeated growth of core@shell nanoparticles composed of $NiFe_2O_4@NiFe_2O_4$ to achieve larger nanoparticles.

Initial phase analysis of synthesized particles from both aminolytic and modified syntheses were performed via powder X-ray diffraction. Samples containing nickel under the aminolytic reaction conditions can be determined to contain two distinct phase contributions as shown in **Figure 2-2**. The spinel crystal pattern can clearly be identified but additionally a face-centered cubic (FCC) pattern that has been determined via Diffrac.EVA phase analysis software to be metallic Ni contamination. Under argon atmospheric conditions the aminolytic reaction consists of a reducing environment with oleylamine serving as a reducing agent. Within these conditions Ni(II) cations will be reduced to Ni^0 and been to nucleate as FCC-Ni nanocrystals as seen in **Figure 2-2B**. Modifying the aminolytic method's reaction atmosphere to be oxygen-rich creates a more oxidative reaction environment that prevents the reduction of Ni(II) (**Figure 2-2A**). This simple modification of the aminolytic reaction, thus deemed the modified aminolytic method enables the synthesis of various Ni(II) containing metal oxide materials including NiO, $NiFe_2O_4$, and $Ni_{1-x}M_xFe_2O_4$ nanocrystals. Beyond Ni(II) behavior in the modified aminolytic method the behavior of other metal cations Cu(II), Mn(II), and Fe(III) were tested as well. These materials respond in various ways as demonstrated in **Figure 2-3** including the partial reduction of Cu(II) to Cu(I) to form Cu_2O nanoparticles, the oxidation
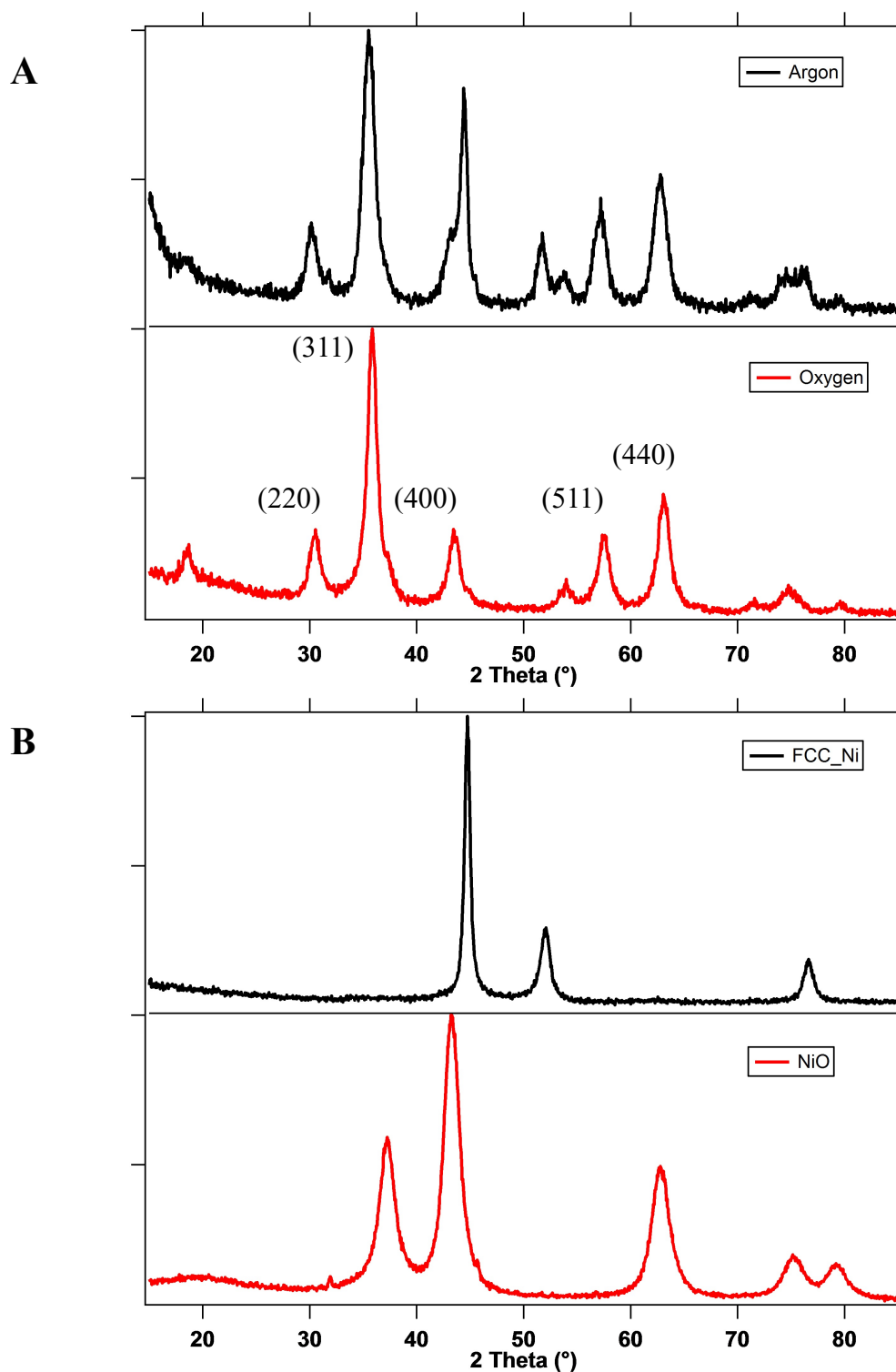
Figure 2-2A,2B: XRD diffraction patterns of (A) NiFe₂O₄ and (B) NiO synthesized under aminolytic method with argon atmosphere (black) and modified aminolytic method with oxygen atmosphere (red)
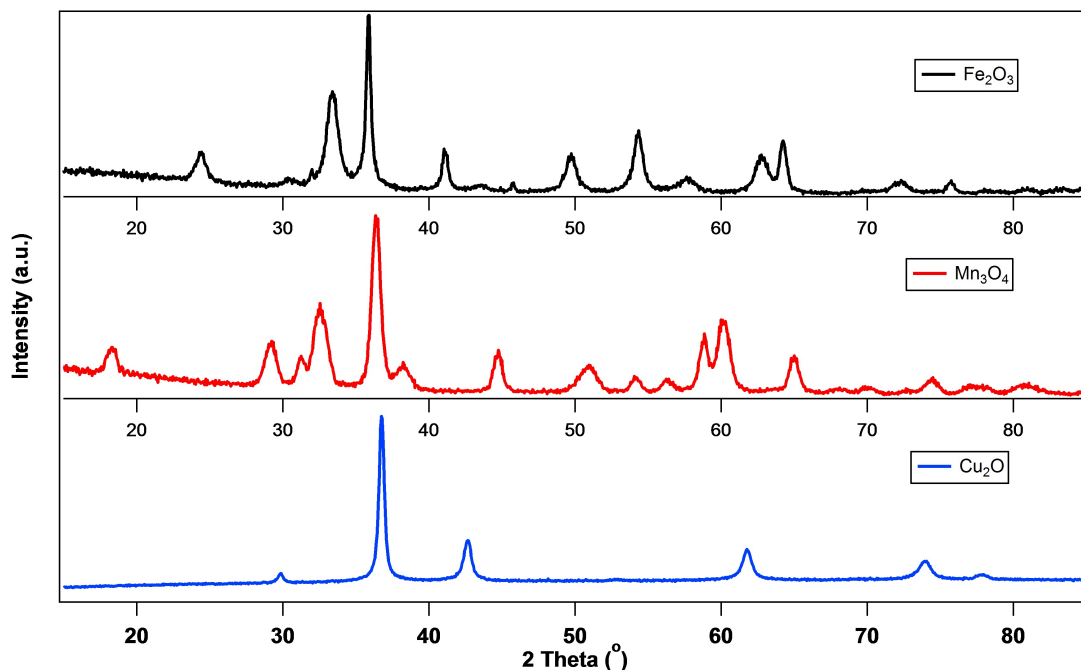
Figure 2-3: XRD Patterns of resulting material phases for Cu(II), Mn(II), and Fe(III) under the modified aminolytic synthesis method resulting in Cu₂O, Mn₃O₄, and Fe₂O₃ respectively.
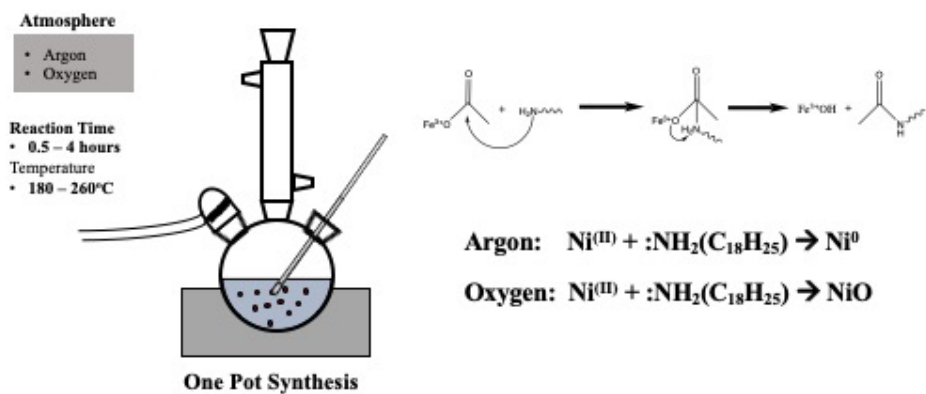
Figure 2-4: Diagram of aminolytic reaction setup, aminolysis reaction mechanism, and reduction of Ni(II) reagents under variable reaction atmospheres.

of Mn(II) to Mn(III) yielding Mn_3O_4 nanoparticles, and prevention of Fe(III) reduction yielding Fe_2O_3 nanoparticles.

Pure-phase $NiFe_2O_4$ nanocrystals synthesized via the modified aminolytic method were confirmed by XRD pattern phase analysis with elemental analysis performed via total reflection x-ray fluorescence (T-XRF) to consist of approximate stoichiometry $Ni_{.95}Fe_{2.05}O_4$ within acceptable error to be pure $NiFe_2O_4$ nanocrystals. The oxygen-rich atmosphere restricts the growth phase of nanocrystal in the LaMer Plot preventing the nucleated nanocrystals from exceeding 6.0 nm in diameter. To circumvent this growth restriction, seed-mediate growth techniques were utilized by seeding modified aminolytic method with previously synthesized 5.5 nm seed crystals that serve as epitaxial growth substrates for the growth of larger nanocrystals alternative to new nucleation events. Through the combining seed-mediated growth and modified aminolytic method a series of $NiFe_2O_4$ nanocrystals ranging in crystallite size from 4.4-10.0 nm were synthesized and characterized for their physical and magnetic properties.

Magnetic studies were performed on all variable size $NiFe_2O_4$ nanocrystal samples utilizing the SQUID magnetometer capable of achieving fields from $\pm$ 5 Telsa and temperatures ranging from 2-350 K. Temperature-dependent measurements were performed on each sample size (5.5, 6.3, 7.0, 8.4, 9.2, and 9.7 nm diameter samples) measured under 100 Oe applied field from 5-305 K. All samples exhibit a magnetic susceptibility maximum before decreasing with higher temperatures; this maximum is known as the blocking temperature (T_B) and is typical behavior of superparamagnetic nanoparticles. The blocking temperature represents the energy barrier at which thermal energy exceeds the alignment of the particle's net magnetic moment with the applied field,

and manifests as a macroscopic paramagnetic state despite the magnetic ordering of the crystal remaining intact. The variable size $NiFe_2O_4$ samples investigated demonstrated increased T_B with increased particle volume (**Figure 2-4**), this correlation between nanoparticle volume and T_B is consistent with the Stoner-Wohlfarth Model for superparamagnetic nanoparticles:

$$E_A = KV sin^2 (\theta) = k_B T_B V \tag{7}$$

In which E_A is the anisotropy energy of the nanoparticle, K is the magnetocrystalline anisotropy constant of the material, V is the volume of the nanoparticle, k_B is the Boltzmann constant, and T_B is the blocking temperature.[17] The low T_B values observed
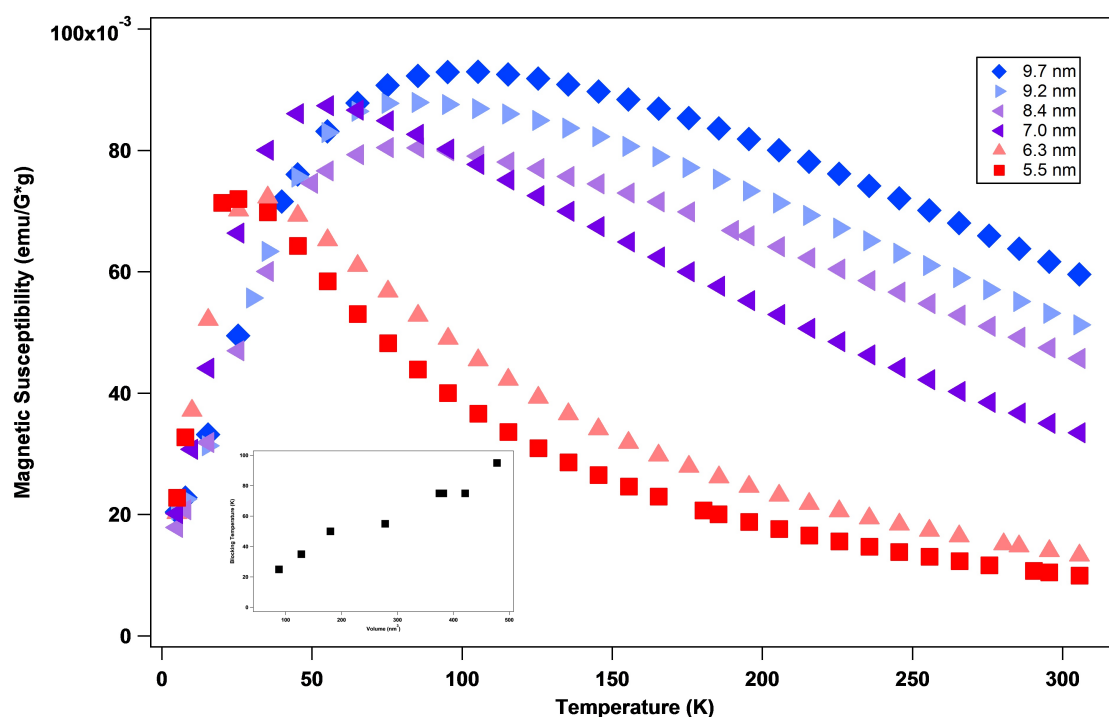
Figure 2-5: Temperature dependent magnetic susceptibility of $NiFe_2O_4$ nanocrystals ranging in diameter from 5.5 to 10.0 nm measured from 5 to 305K under 100 Oe applied field. Inset demonstrates linear correlation between the blocking temperature and volume of the nanoparticle in good agreement with the Stoner-Wohlfarth model for superparamagnetic nanoparticles.

with $NiFe_2O_4$ nanocrystals are consistent with expectations of low magnetocrystalline anisotropy constant of bulk $NiFe_2O_4$.

Field-dependent magnetization measurements of 6.3 nm $NiFe_2O_4$ nanocrystals were also performed at 5K with fields ranged from $\pm$ 5 Telsa (**Figure 2-6**). The sample exhibits low saturation and remanent magnetizations of 32.4 and 11.5 emu/g respectively. The coercivity of the sample is 300 Oe, which is consistent with $NiFe_2O_4$ possessing a low magnetocrystalline anisotropy constant indicative of a soft magnet. The field-dependent magnetic behavior is consistent across the size range investigated in this study. In addition to the magnetic measurements performed on as-synthesized $NiFe_2O_4$ nanocrystals,
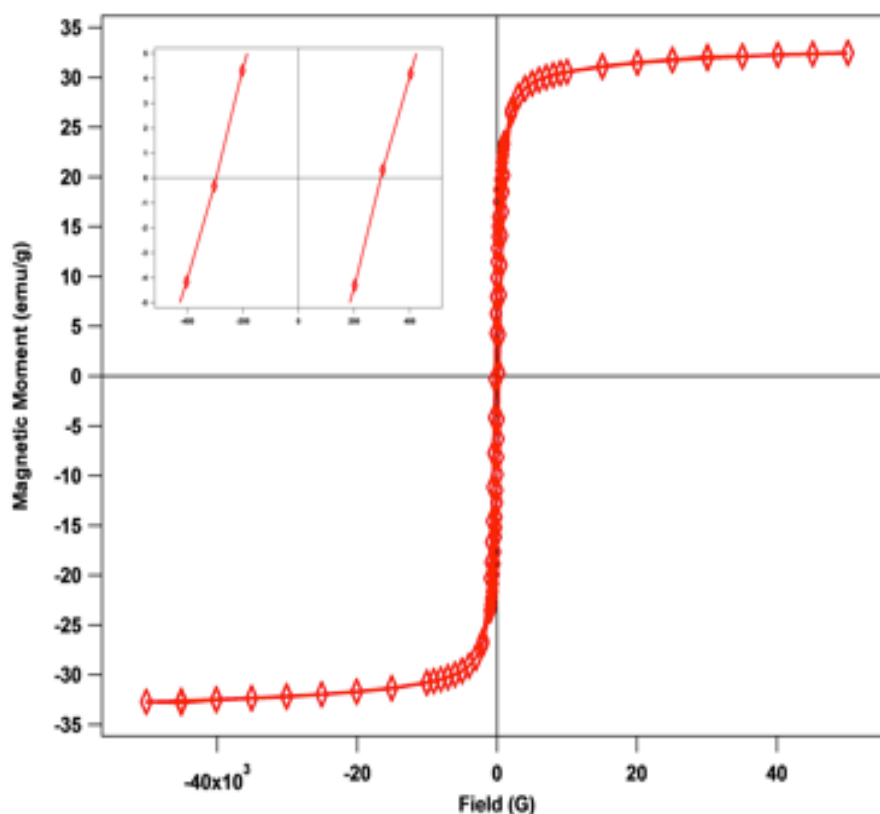
Figure 2-6:   Field-dependent magnetic hysteresis of $NiFe_2O_4$ nanocrystals (6.0 nm diameter) measured at 5 K.

measurements were also performed on ligand-free nanoparticles that had undergone a ligand stripping procedure. The stripped samples exhibit increased saturation and remanent magnetization values (**Figure 2-7**) and additionally a slight increase in coercivity from 300 Oe to 450 Oe. This increase in coercivity is the product of enhanced magnetic moment stability through increased interparticle interactions of neighboring nanoparticles.[18-20]

Ferromagnetic resonance spectroscopy measures the microwave absorption profile of ferromagnetic materials through exposure of high frequency radiation under an applied magnetic field. All FMR measurements performed in this work were performed on Bruker
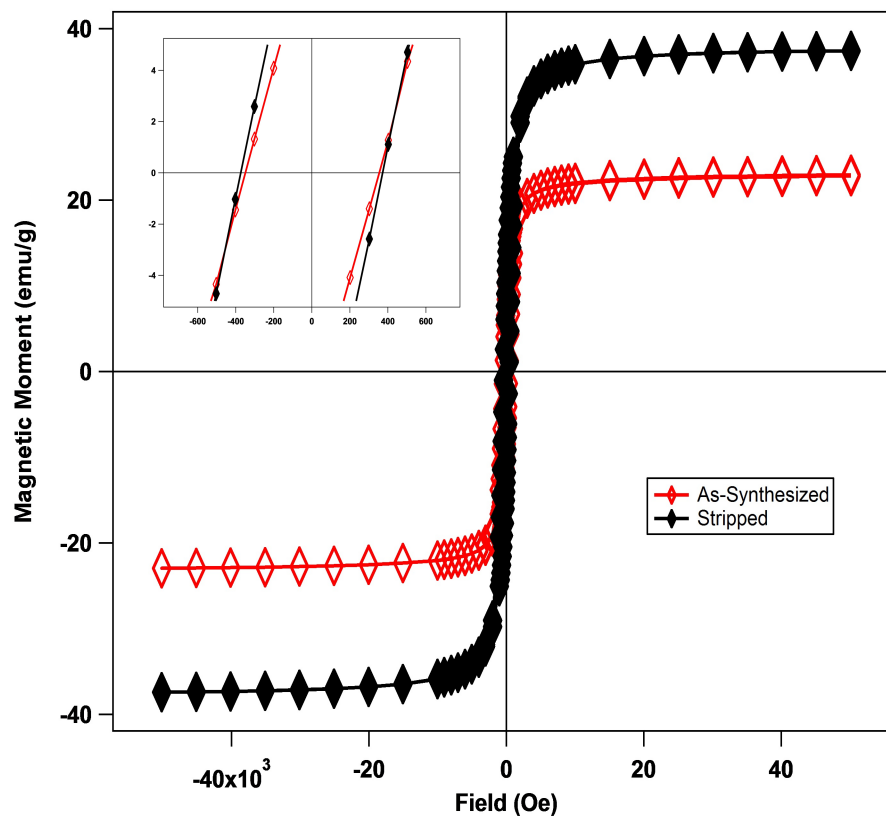
Figure 2-7: **Field-dependent magnetic hysteresis of NiFe$_2$O$_4$ nanocrystals both as-synthesized and stripped of surface ligands.**

EMX spectrometer (9.88 GHz) while sweeping the applied field from 250 to 10,000 Oe. Spinel ferrite compositions each exhibit unique FMR profiles (**Figure 2-8**) with $NiFe_2O_4$ possession a strong absorption signal, narrow linewidth and resonance field at approximately 3200 Oe (**Figure 2-9**). Investigation of the FMR profiles of variable sized $NiFe_2O_4$ nanocrystals was performed as depicted in **Figure 2-10**. The FMR profiles of all samples maintained a narrow linewidth $\Delta H < 1,000$ Oe, high absorption intensity, and resonance fields ranging from 3200-3300 Oe. The lower resonance field samples were the larger nanocrystals with smaller samples shifting absorbing closer to 3,300 Oe. With the difference in resonance fields for different sized $NiFe_2O_4$ being negligible, and no observable trends of either the linewidth or absorption intensity with the size of the nanocrystal for the purposes of tuning the FMR properties the crystallite size is a minimal contributing factor. Ferromagnetic resonance studies of mixed composition $Ni_{1-x}M_xFe_2O_4$
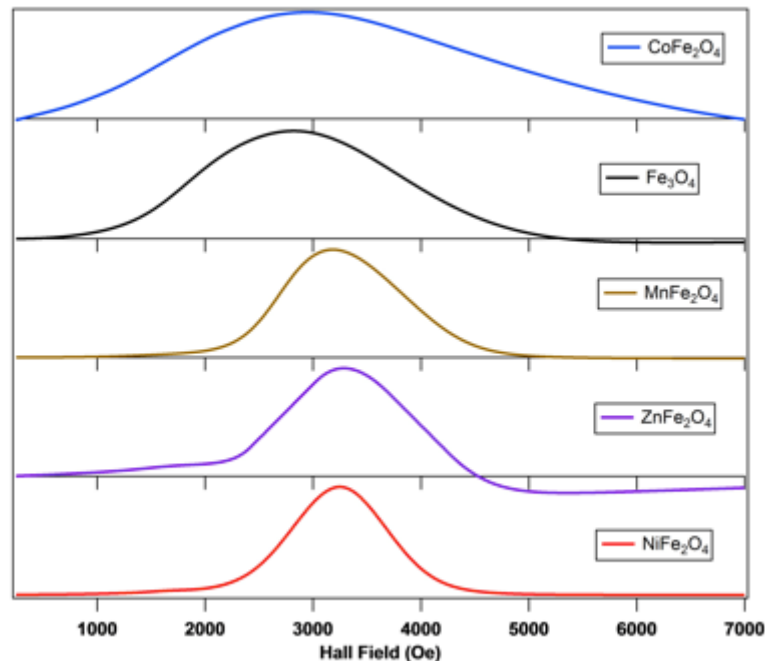
Figure 2-8: Ferromagnetic resonance spectroscopy profiles of various pure phase spinel ferrite nanocrystals, normalized.
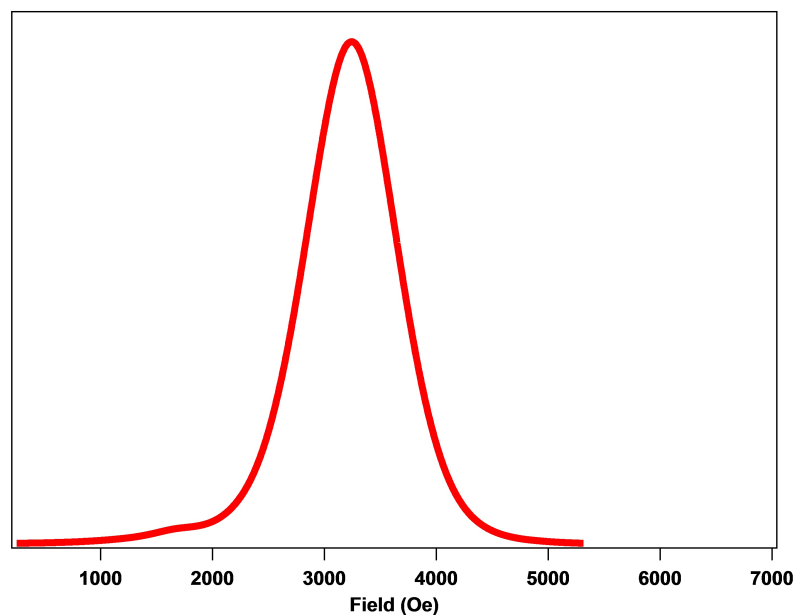
Figure 2-9: Ferromagnetic resonance spectroscopy profile of NiFe$_2$O$_4$ nanocrystal.
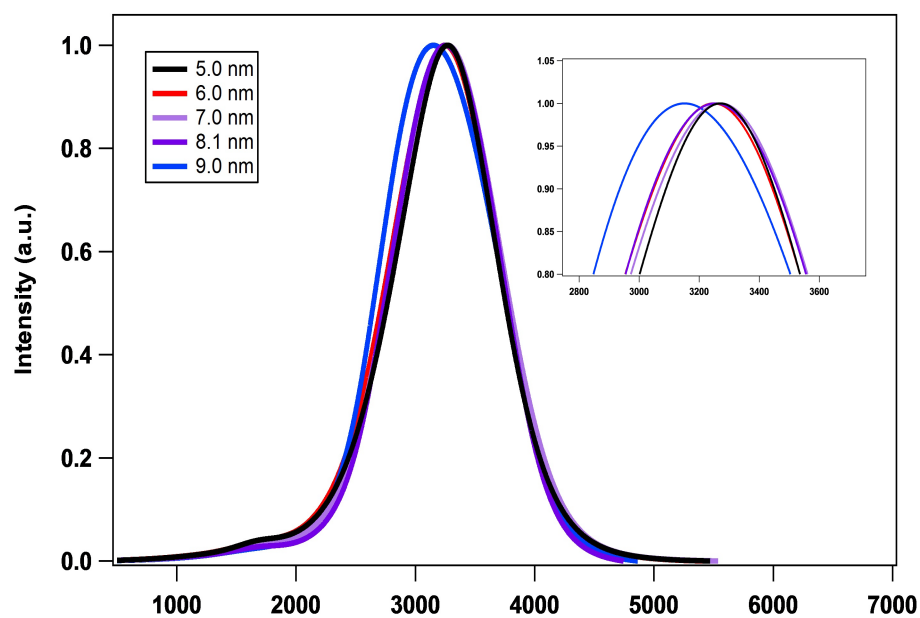
Figure 2-10: Ferromagnetic resonance spectroscopy profile of various size NiFe$_2$O$_4$ nanocrystals.

(M = Zn^{2+} and Co^{2+}) and core@shell architecture nanoparticles will be expanded upon in Chapters III-IV.

The modified aminolytic method enables the synthesis of Ni(II) oxide nanocrystals such as NiO and $NiFe_2O_4$ with controlled crystallite size and low polydisparity. The introduction of an oxygen rich reaction atmosphere prevents the reduction of Ni(II) to Ni^0 and also increases the binding affinity of the oleylamine surfactant to the metal oxide surface restricting the growth of nanocrystals. The restricted growth enables the controlled synthesis of low polydisparity nanocrystals of 4.5-6.0 nm size regime but requires the use of seed-mediated growth to synthesize nanoparticles exceeding this regime. The synthesized $NiFe_2O_4$ nanocrystals possess low blocking temperatures <100 K, with low coercivity H = 300 Oe, and additionally low saturation and remanent magnetization values M_S = 32.4 emu/g and M_r = 11.5 emu/g. The FMR investigations of $NiFe_2O_4$ nanocrystals provides insight into how modification of material properties influences microwave absorption and specifically confirms $NiFe_2O_4$ as a viable high frequency antennae material due to its narrow linewidth and high absorption intensity at 9.88 GHz.

2.4   Conclusions

The novel synthesis of high-quality size-controlled $NiFe_2O_4$ nanocrystals was accomplished through introduction of an oxygen-rich atmosphere to produce the modified aminolytic method. Physical characterization of the synthesized $NiFe_2O_4$ nanocrystals confirmed the crystallite size and phase purity via XRD; chemical composition via T-XRF; and crystallite size, morphology, and polydisparity via TEM. After confirmation of the synthesis of pure $NiFe_2O_4$ nanocrystals, the nanoparticles were investigated for their

superparamagnetic and ferromagnetic resonance properties. The temperature dependent magnetic susceptibility studies demonstrated size-dependent trend of increasing blocking temperature with increased nanoparticle volume that fits the Stoner-Wohlfarth model for superparamgnetic nanoparticles. Magnetic hysteresis measurements demonstrate that $NiFe_2O_4$ is a soft ferrimagnet with low coercivity $H = 300$ Oe, low saturation and remanent magnetizations $M_S = 32.4$ emu/g and $M_r = 11.5$ emu/g. Ferromagnetic resonance spectroscopy measurements indicate that $NiFe_2O_4$ nanocrystals are good candidates for ultra high frequency applications with resonance field around 3200 Oe under 9.88 GHz frequency with large absorption intensity and narrow linewidth. The successful synthesis of superparamagnetic $NiFe_2O_4$ nanocrystals via the modified aminolytic method provides novel insight into the nanomagnetic properties and the potential technological applications in telecommunications.

2.5 REFERENCES

1.   David R. Baselt, G. U. L., Mohan Natesan, Steven W. Metzger, Paul E. Sheehan, Richard J. Colton, A Biosensor Based on Magnetoresistance Technology. *Biosens Bioelectron.* **1998,** *13*, 731-739.

2.   Jang, J. T.; Nah, H.; Lee, J. H.; Moon, S. H.; Kim, M. G.; Cheon, J., Critical enhancements of MRI contrast and hyperthermic effects by dopant-controlled magnetic nanoparticles. *Angew Chem Int Ed Engl* **2009,** *48* (7), 1234-8.

3.   Von Sovskii, S. V., Ferromagnetic Resonance: The Phenomenon of Resonant Absorption of a High-Frequency Magnetic Field Ferromagnetic Substances. *Elsevier, LTD.* **2016**, 1-340.

4.   Ozgur, U., Alivov, Y., Morkoc, H., Microwave Ferrites, part 1: Fundamental Properties. *J. Mater. Sci. Mater. Electron.* **2009,** *20*, 789-834.

5.   Tiano, A. L.; Papaefthymiou, G. C.; Lewis, C. S.; Han, J.; Zhang, C.; Li, Q.; Shi, C.; Abeykoon, A. M. M.; Billinge, S. J. L.; Stach, E.; Thomas, J.; Guerrero, K.; Munayco, P.; Munayco, J.; Scorzelli, R. B.; Burnham, P.; Viescas, A. J.; Wong, S. S., Correlating Size and Composition-Dependent Effects with Magnetic, Mössbauer, and Pair Distribution Function Measurements in a Family of Catalytically Active Ferrite Nanoparticles. *Chem Mater.* **2015,** *27* (10), 3572-3592.

6.   Chao Liu, B. Z., Adam J. Rondinone, and Z. John Zhang, Chemical Control of Superparamagnetic Properties of Magnesium and Cobalt Spinel Ferrite Nanoparticles through Atomic Level Magnetic Couplings. *J Am Chem Soc* **2000,** *122*, 6263-6267.

7.   Sabo, D. E., Novel Synthesis of Metal Oxide Nanoparticles via the Aminolytic Method and the Investigation of Their Magnetic Properties. **2012**, 158.

8.   Chen, H. W., Aminolytic Synthesis and Ferromagnetic Resonance of Cobalt and Manganese Based Spinel Ferrite Nanoparticles. **2018**, 148.

9.   Song, Q.; Zhang, Z. J., Correlation between Spin-Orbital Coupling and the Superparamagnetic Properties of Magnetite and Cobalt Ferrite Spinel Nanocrystals. *J Phys Chem B.* **2006,** *110*, 11205-11209.

10.   Lasheras, X.; Insausti, M.; Gil de Muro, I.; Garaio, E.; Plazaola, F.; Moros, M.; De Matteis, L.; M. de la Fuente, J.; Lezama, L., Chemical Synthesis and Magnetic Properties of Monodisperse Nickel Ferrite Nanoparticles for Biomedical Applications. *J Phys Chem C.* **2016,** *120* (6), 3492-3500.

11.   Kefeni, K. K.; Msagati, T. A. M.; Mamba, B. B., Ferrite nanoparticles: Synthesis, characterisation and applications in electronic device. *Mater Sci Eng: B.* **2017,** *215*, 37-55.

12.   Park, J.; Joo, J.; Kwon, S. G.; Jang, Y.; Hyeon, T., Synthesis of monodisperse spherical nanocrystals. *Angew Chem Int Ed Engl* **2007,** *46* (25), 4630-60.

13.   Han, M. H., Development of Synthesis Method for Spinel Ferrite Magnetic Nanoparticle and Its Superparamagnetic Properties. **2008**, 181.

14.   Zhang, Z.; Zhong, X.; Liu, S.; Li, D.; Han, M., Aminolysis route to monodisperse titania nanorods with tunable aspect ratio. *Angew Chem Int Ed Engl* **2005,** *44* (22), 3466-70.

15.   Mattei, J.-L.; Le Guen, E.; Chevalier, A.; Tarot, A.-C., Experimental determination of magnetocrystalline anisotropy constants and saturation magnetostriction constants of NiZn and NiZnCo ferrites intended to be used for antennas miniaturization. *J Magn Magn Mater.* **2015,** *374*, 762-768.

16.   N Ponpandian, P. B., and A Narayanasamy, Electrical Conductivity and Dielectric Behavior of Nanocrystalline $NiFe_2O_4$ Spinel. *J Phys Condens Matter..* **2002,** *14*, 3221-3237.

17.   Tannous, C.; Gieraltowski, J., The Stoner–Wohlfarth model of ferromagnetism. *Euro J Phys.* **2008,** *29* (3), 475-487.

18.   Vestal, C. R., Zhang, Z.J., Synthesis and Magnetic Characterization of Mn and Co Spinel Ferrite-Silica Nanoparticles with Tunable Magnetic Core. *Nano Letters* **2003,** *3* (12), 1739-1743.

19.   Tartaj, P., Serna, C.J., Synthesis of Monodisperse Superparamagnetic Fe/Silica Nanospherical Composites. *J Am Chem Soc* **2003,** *125*, 15754-15755.

20.   Vestal, C. R., Zhang, Z.J., Effects of Surface Coordination Chemistry on the Magnetic Properties of MnFe2O4 Spinel Ferrite Nanoparticles. *J Am Chem Soc* **2003,** *125*, 9828-9833.

CHAPTER 3: SYNTHESIS OF MIXED COMPOSITION NICKEL BASED SPINEL FERRITE NANOPARTICLES (NI$_{1-X}$M$_X$FE$_2$O$_4$) AND THEIR FERROMAGNETIC RESONANCE PROPERTIES

3.1 Introduction

Magnetic nanocrystals have been researched intensively to further the fundamental understanding of nanomagnetism for various applications such as magnetic recording media, catalysis, drug delivery, biomedical imaging, sensors, and telecommunication devices.[1-6] The magnetic properties of nanocrystals can be manipulated through synthetic control of the size, morphology, and chemical composition.[7] Superparamagnetism is a size-dependent magnetic behavior that as the nanoparticle volume increases so does the thermal activation barrier for transitioning to a superparamagnetic state.[8, 9] Substitution of metal cations into the chemical composition can alter the magnetocrystalline anisotropy energy manipulating the coercivity, saturation, and remanent magnetizations.[10] Synthesis of high-quality single domain nanocrystals is essential for developing fundamental understanding of nanomagnetism.

Modern society has become increasingly interconnected with a plethora of wireless technologies becoming integrated into everyday life, but with this increased connectivity brings technological obstacles. Available frequencies for devices to operate on are limited and the increased reliance on wireless devices is crowding these available signals. Microwave ferrites are a class of magnetic materials including spinel ferrites, hexaferrites,

and garnets that absorb electromagnetic radiation in the desirable microwave frequencies.[11] Magnetic materials compose vital components to wireless devices such as antennae, circulators, isolators, and filters.[11] Spinel ferrites are a flexible microwave ferrite with nanomagnetic properties capable of being controlled through size, morphology, and chemical composition.[12, 13] To study the fundamental properties of microwave absorption with nanomagnetic materials through synthetic control of magnetic properties investigated with ferromagnetic resonance spectroscopy.

Ferromagnetic resonance is a spectroscopic analysis technique similar to electron spin resonance (ESR) and nuclear magnetic resonance (NMR) in which a ferromagnetic sample is subjected to a set microwave frequency while sweeping an applied magnetic field, upon reaching the resonance field for the material the precession frequency is absorbed by excitation of an unpaired electron.[3] Ferromagnetic resonance studies have been largely performed on bulk/thin films microwave ferrites that are subject to domain wall movement, field orientation, and crystal defects.[11, 14, 15] Yttrium-iron garnet (YIG) nanocrystals have been studied as microwave components for microelectronics.[11] In flexible electronics copper ferrite thin films have been utilized as antennae sensor for motion detection, via orientation of the films for in-of-plane/out-of-plane ferromagnetic resonance.[15] Previous, ferromagnetic resonance studies of microwave ferrites have yet to establish a link between the intrinsic magnetic properties of a material with its ferromagnetic resonance properties due to complex material factors such as magnetic domain wall movement, porosity, crystallinity, and chemical impurities.[14, 16, 17] Nickel-zinc ferrites are a family of microwave ferrites that have been utilized for ultra-high

frequency applications such as transformer cores thanks to their high permeability, low loss, and high resistance.[18]

We have developed a novel aminolytic method to synthesis single crystalline spinel ferrite nanocrystals of controlled size and chemical compositions. Utilizing the aminolytic method we have synthesized mixed solid-solution $Ni_{1-x}M_xFe_2O_4$ (M = Zn^{2+} and Co^{2+}) nanocrystals with x corresponding to the molar concentration of divalent metal cations. The unique magnetic properties of mixed solid solution $Ni_{1-x}M_xFe_2O_4$ nanocrystals have been investigated via superconducting quantum interference device (SQUID) magnetometry. Ferromagnetic resonance spectroscopy was utilized to establish a link between the intrinsic magnetic properties of nanoscale spinel ferrites and the absorption of ultra-high frequency microwaves. The results of these investigations show that mixed solid solutions $Ni_{1-x}M_xFe_2O_4$ (M = Zn^{2+} and Co^{2+}) nanocrystals provide a class of microwave ferrites with tunable precession frequency properties that can be synthesized to meet specific device needs for ultra-high frequency applications.

3.2 Experimental

3.2.1 Metal Acetate Precursor

Metal acetate precursors for the aminolytic method were synthesized through the reaction of metal hydroxides with acetic acid. A typical preparation for $NiFe_2O_4$ synthesis begins by dissolving a 1:1:4 ratio of metal salts such as $NiCl_2 \bullet 6(H_2O)$ (3 mmol), MCl_2 (3 mmol) and $FeCl_3$ (12 mmol) in 150 mL of DI water while vigorously stirred. Once all the metal salts are dissolved in solution, 150 mL of 5 M NaOH solution was added causing the precipitation of metal hydroxide complexes, the solution was stirred for 2 hours. The metal

hydroxide mixture was collected via centrifugation; the mixture was washed 4 times with DI water to remove excess NaOH and Na^+ from the solid mixture. The metal hydroxide mixture was transferred to a 1000 mL beaker with stir bar, approximately 200 mL of glacial acetic acid was added dissolving the metal hydroxides. Stir the solution overnight while applying 100°C heat to promote the formation of metal acetates while removing excess moisture. The dried metal acetate mixture was collected the following day, and ground with mortar and pestle to promote thorough mixing of the metal acetate precursors in the desired stoichiometric ratio.

3.2.2 Modified Aminolytic Synthesis

To prepare 5 nm $Ni_{1-x}M_xFe_2O_4$ nanocrystals, 12 mmol of mixed metal acetate precursor, 20 mL of oleylamine, and 60 mL of dibenzyl ether to a 3-neck round bottom flask. The reaction mixture is stirred and refluxed at 140°C for 1 hour. After 1 hour of mixing a flow of O_2 gas to the reaction vessel and refluxed at 220°C for 1 hour. The reaction is cooled and collected via centrifuge and washed with ethanol to remove excess organics from the synthesized nanocrystals. Synthesis of complex mixed solid solution $Ni_xM_{1-x}Fe_2O_4$ nanocrystals is simple though preparation of appropriate stoichiometric mixed metal acetate precursors.

3.2.3 Instrumentation

Sample crystallinity and phase purity was measured with powder x-ray diffraction on a Bruker D8 Advance diffractometer. Chemical analysis was performed with total reflection x-ray fluorescence (T-XRF) using a Bruker S2 PICOFOX. A superconducting quantum inference device (SQUID) magnetometer (Quantum Design MPMS-5S) with an

applied magnetic field up to 5 T at temperature range of 2-400 K was used to perform both temperature and magnetic field dependent magnetization measurements. The temperature range was measured from 5 to 315 K. Field-dependent magnetic measurements were prepared by dispersing the dry nanocrystal powder in eicosane (Aldrich, 99%) to stabilize and eliminate interparticle interaction effects.

3.3 Results and Discussion

3.3.1 Physical and Magnetic Properties

Mixed solid solution $Ni_{1-x}M_xFe_2O_4$ (M= Zn^{2+} and Co^{2+}) nanocrystals were synthesized through the modified aminolyitc method to be of single spinel crystal phase via XRD pattern analysis (**Figure 3-1**) . XRD patterns were consistent with formation of nanocrystals from observed peak broadening and the crystallite grain size was calculated with the Scherrer equation. Elemental analysis of each sample was performed via total reflection x-ray fluorescence to determine the molar concentration ratio of the transition metal components (**Table 3-1**).

Mixed solid solution $Ni_{1-x}Zn_xFe_2O_4$ and $Ni_{1-x}Co_xFe_2O_4$ nanoparticle systems were also investigated for their temperature dependent magnetic susceptibility (**Figures 3-2A,B**). The maximum magnetic susceptibility at T_B increased with increased molar concentration of zinc in the $Ni_{1-x}Zn_xFe_2O_4$ but the thermal stability is largely unperturbed by the substitution. The blocking temperature of $Ni_{1-x}Co_xFe_2O_4$ nanocrystals demonstrates an evident correlation between increased molar concentration of cobalt and increased thermal stability resulting in a maximum $T_B = 245$ K for 6.0 nm $CoFe_2O_4$ nanoparticles (**Figure 3-2B**).[13]
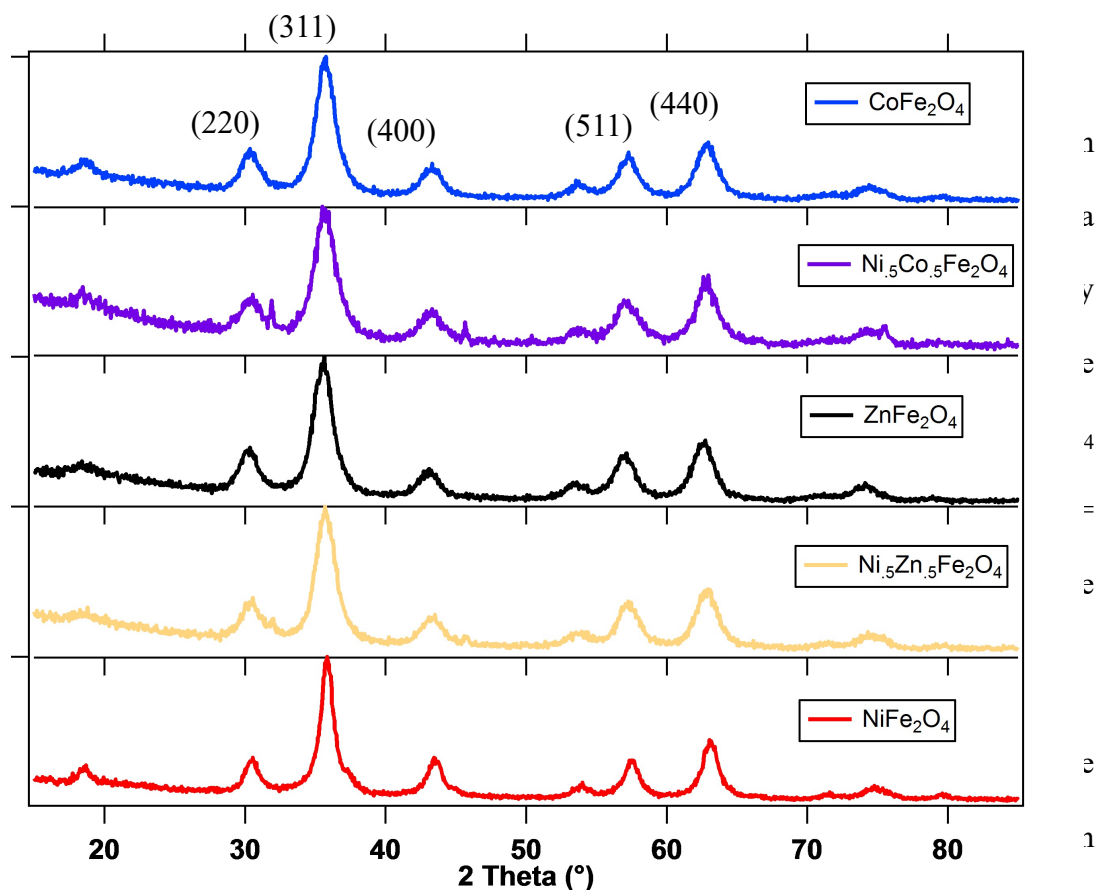
Figure 3-1: XRD patterns for pure spinel phase for select nickel-based spinel ferrite nanocrystals.

of cobalt cations into the soft ferrimagnet lattice of $NiFe_2O_4$ increases the H_C with increased cobalt concentration as the spin-orbit coupling of the crystal lattice increases to $CoFe_2O_4$ $H_C = 9,800$ Oe. **Figure 3-3** shows the increase in coercivity of $Ni_xCo_{1-x}Fe_2O_4$ nanocrystals correlates with increased substitution of strong S-L coupled Co^{2+} cations resulting increased magnetocrystalline anisotropy.[10] With similarly sized $CoFe_2O_4$ possessing a coercivity 30-fold larger than the magnetically soft $NiFe_2O_4$ nanocrystals. The saturation and remanent magnetizations also increased with higher molar concentrations of cobalt (**Figure 3-3**). The substitution of Zn^{2+} cations into the $Ni_xZn_{1-x}Fe_2O_4$ nanocrystals results in the reduction of coercivity and remanent magnetization, but
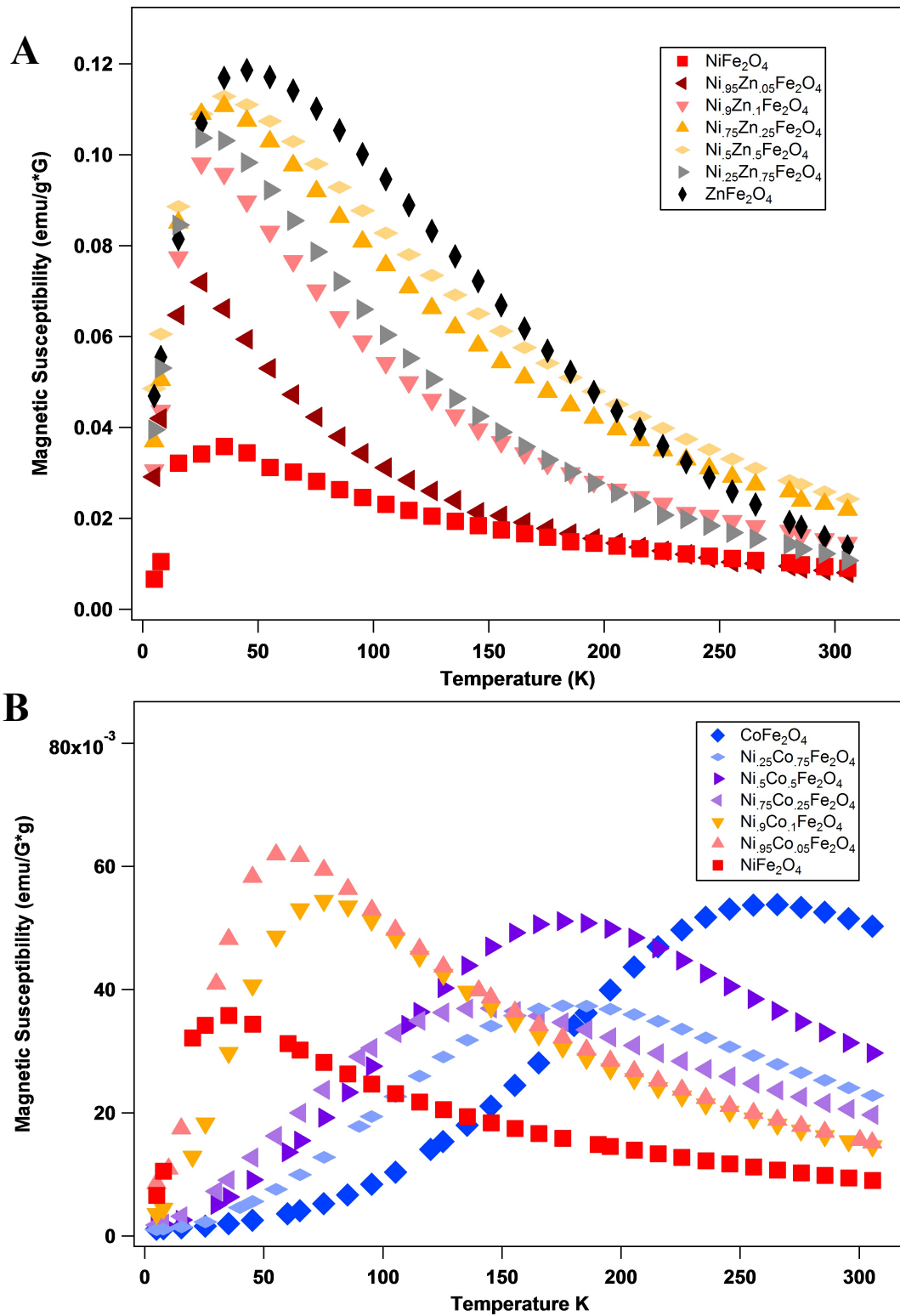
Figure 3-2A,B: Temperature dependent magnetic susceptibility of mixed solid solution (A) $Ni_{1-x}Zn_xFe_2O_4$ and (B) $Ni_{1-x}Co_xFe_2O_4$ nanocrystals measured from 5 to 315 K under an 100 Oe applied field.

also a large increase in saturation magnetization. The reduced H_C and M_r values are the result of weaker spin-orbit coupling with Zn^{2+} cations, the increased saturation magnetization is most likely the product of partially mixed cation distribution resulting in increased Fe^{3+} super-exchange interactions.

The nanoparticulate systems of $NiFe_2O_4$, $Ni_{1-x}Zn_xFe_2O_4$, and $Ni_{1-x}Co_xFe_2O_4$ all exhibit superparamagnetic behavior with blocking temperatures below room temperature. Mixed solid-solution spinel ferrites $Ni_{1-x}M_xFe_2O_4$ of similar sizes can yield vastly different magnetic properties depending on the molar concentration of the divalent species and the A-B site divalent cationic distribution. Spinel ferrite crystal structure consists of cubic lattice with metal cations occupying tetrahedral (A sites) and octahedral (B sites), the superexchange coupling between the A-B sites gives rise to the ferrimagnetic moment of the nanoparticle. Divalent zinc has a $3d^{10}$ electronic structure that contributes no spins to ferrimagnetic structure of the spinel ferrite potentially weakening the net magnetic moment.[19] Substitution of Co^{2+} cations introduces strong spin-orbit L-S coupling into the $Ni_{1-x}Co_xFe_2O_4$ crystal lattice allows for tuning of the anisotropy energy of the nanoparticle to manipulate desired magnetic properties. In single domain nanocrystals the magnetic anisotropy is representative of the accumulative contributions of the individual magnetic cations within the crystal lattice.[20]

Bulk $ZnFe_2O_4$ possesses a normal spinel crystal structure with divalent Zn^{2+} cations preferentially occupying tetrahedral A-sites of the spinel lattice breaking in superexchange coupling.[19] The temperature-dependent magnetic behavior of $Ni_{1-x}Zn_xFe_2O_4$ nanoparticles for all chemical compositions are blocked below 100 K with no correlation between the molar concentration of zinc and the thermal stability (**Figure 3-2A**). The field-dependent
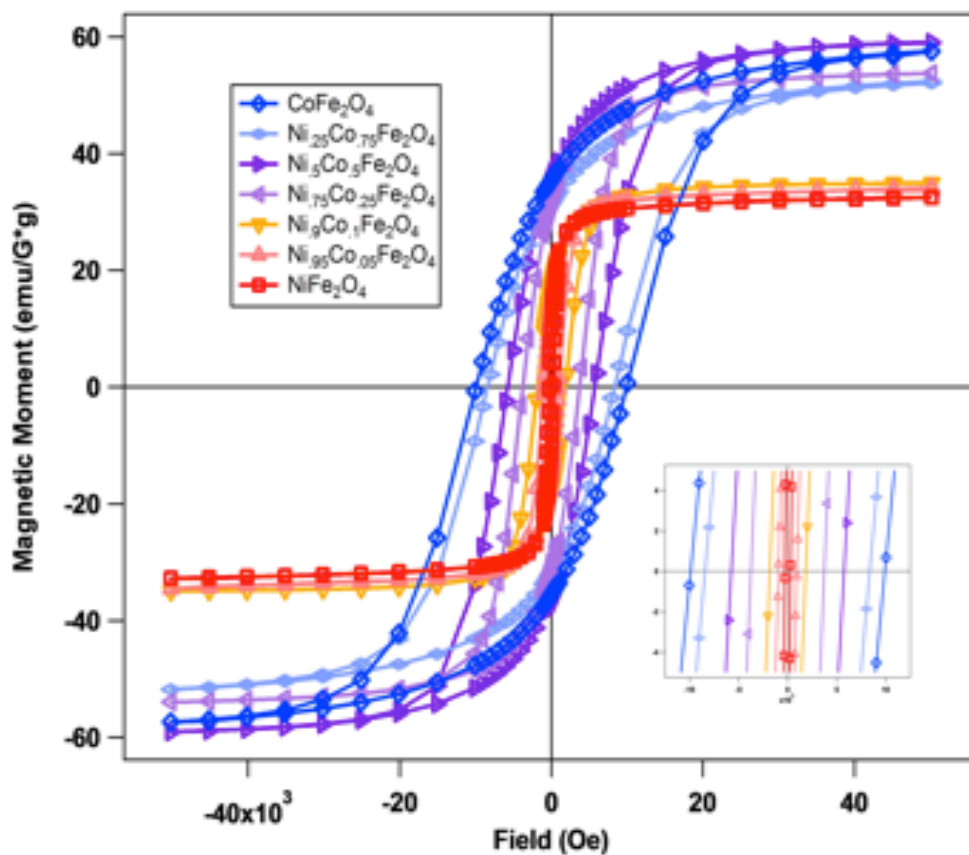
Figure 3-3: Field-dependent magnetic hysteresis measurements of mixed solid solution $Ni_{1-x}Co_xFe_2O_4$ nanocrystals measured at 5 K with applied field ranging from $\pm$ 5 T.

magnetization (**Figure 3-4**) shows increasing the molar concentration of zinc increases the saturation with decreased remanent magnetizations and coercivity. The increased M_s and M_r values correspond to an increase in the net magnetic moment of $ZnFe_2O_4$ nanoparticles that is counter to the expected weakening of superexchange coupling observed for bulk samples. Nanoscale $Ni_{1-x}Zn_xFe_2O_4$ synthesized via the aminolytic method must possess a unique mixed distribution of Zn^{2+} cations within the spinel crystal lattice that promotes strong A-B coupling of the Fe^{3+} cations.
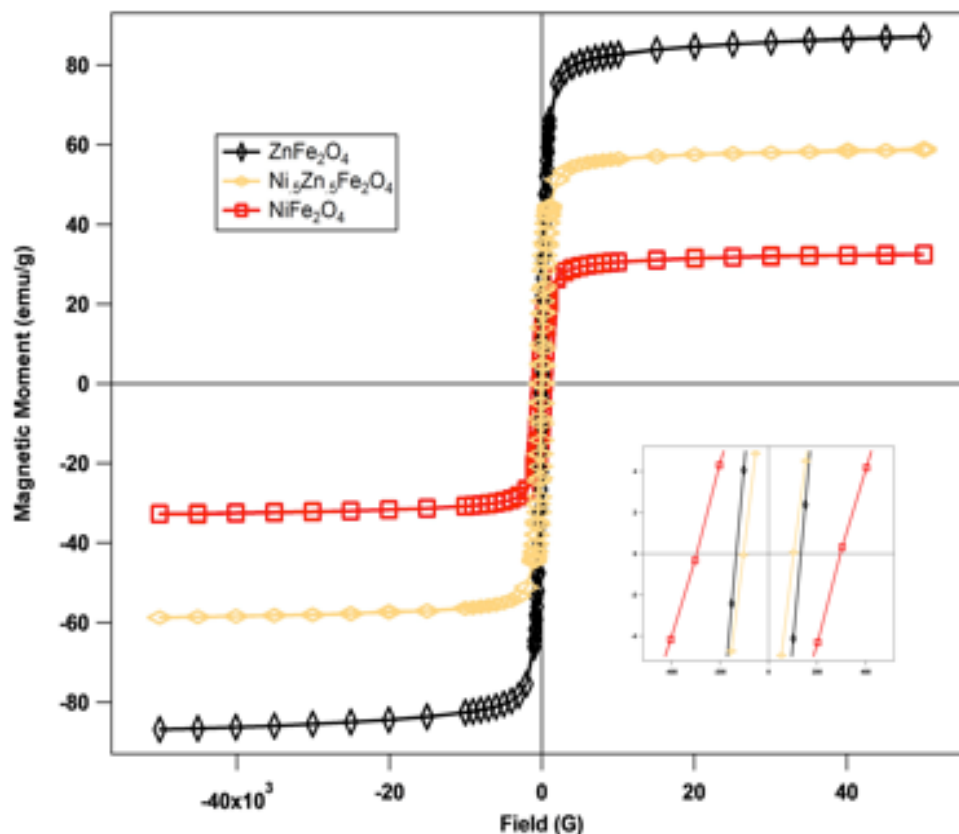
Figure 3-4: **Field-dependent magnetic hysteresis measurements of mixed solid solution $Ni_{1-x}Zn_xFe_2O_4$ nanocrystals measured at 5 K with applied field ranging from $\pm$ 5 T.**

The temperature-dependent behavior of similarly sized (6.0 nm) mixed solid-solution $Ni_{1-x}Co_xFe_2O_4$ nanoparticles is dependent on the anisotropy constant of the chemical composition. The maximum blocking temperature for 6.0 nm diameter $Ni_{1-x}Co_xFe_2O_4$ system is $T_B = 245$ K for $CoFe_2O_4$ and T_B decreases as the molar concentration of cobalt decreases (**Figure 3-2B**). The increased thermal stability of $CoFe_2O_4$ can be attributed to the strong spin-orbit S-L coupling of Co^{2+} cations increasing the anisotropy constant K. The anisotropy energy of magnetic nanocrystals is also related to the coercivity of the ferrimagnetic state. Coercivity is a measure of the field strength required to overcome anisotropy energy barrier and flip the magnetic spin.[9] There is a direct correlation between the molar concentration of cobalt and the coercivity of $Ni_{1-x}Co_xFe_2O_4$

nanocrystals (**Figure 3-3**). The ability to chemically tune the superparamagnetic properties of spinel ferrite nanoparticles provides a strategy to tailor nanomaterials for specific application demands.

3.3.2 Ferromagnetic Resonance Spectroscopy

The room temperature (9.88 GHz) ferromagnetic resonance spectrums for spinel ferrites nanocrystals of $NiFe_2O_4$, $ZnFe_2O_4$, $CoFe_2O_4$ and mixed solid solution composition samples are shown in **Figures 3-5, 3-6**. **Table 3-1** displays the resonance field (H) and the linewidth (ΔH) for each sample within addition to their magnetic properties of blocking temperature (T_B), room temperature magnetic susceptibility (X), coercivity (H_C), saturation (M_S), and remanent (M_r) magnetizations. The ferromagnetic resonance spectrums of $Ni_{1-x}Zn_xFe_2O_4$ and $Ni_{1-x}Co_xFe_2O_4$ nanoparticulate systems are shown in **Figures 3-5, 3-6**, the spectra are normalized with respect to absorption intensity to highlight the variations of absorption field and linewidth for the different samples. **Figure 3-7** shows the FMR spectrum without normalization for $Ni_{1-x}Co_xFe_2O_4$ as the increased molar concentration of cobalt weakens absorption intensity.

Magnetic properties measured by ferromagnetic resonance spectroscopy consists of the resonance field (H) which is the applied magnetic field required for the precession frequency to be absorbed, linewidth (ΔH), which is the full-width half-maximum of the absorption peak, and absorption intensity. The absorption of the resonance frequency arises from the spin-orbit interactions and can be approximated by Zeeman splitting:

$$\Delta E = h\nu = g\mu_B H_0 \tag{8}$$
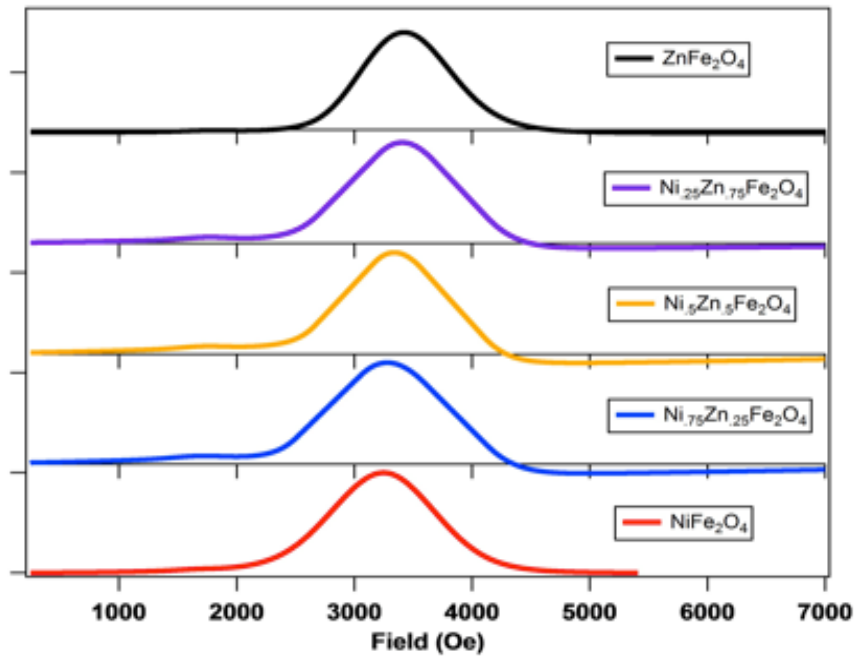
Figure 3-5: Normalized integrated ferromagnetic resonance spectra of mixed composition $Ni_{1-x}Zn_xFe_2O_4$ nanoparticles measured frequency of 9.88 GHz with applied field swept from 250 to 10,000 Oe
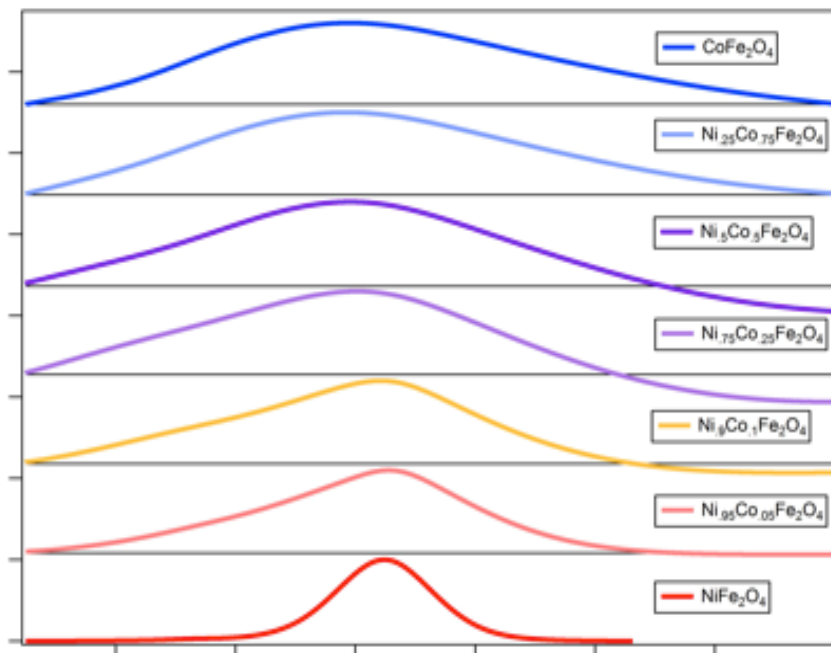
Figure 3-6: Normalized integrated ferromagnetic resonance spectra of mixed composition $Ni_{1-x}Co_xFe_2O_4$ nanoparticles measured frequency of 9.88 GHz with applied field swept from 250 to 10,000 Oe
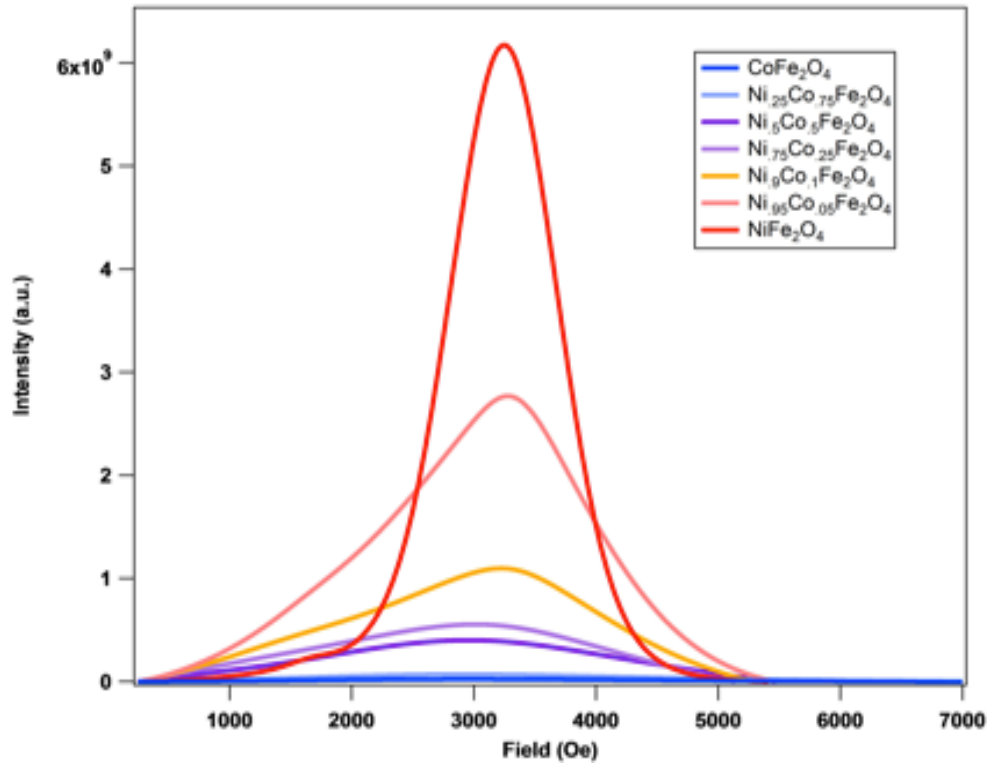
Figure 3-7: Integrated ferromagnetic resonance spectra of mixed composition Ni$_{1-x}$Co$_x$Fe$_2$O$_4$ nanoparticles measured frequency of 9.88 GHz with applied field swept from 250 to 10,000 Oe

where h is Plank's constant, ν is the frequency, g is the g-factor, μ is the Bohr magneton, and B is the applied magnetic field.[21] The ferromagnetic resonance field corresponds to the absorbed energy necessary to excite electrons for Zeeman splitting to occur. Low resonance field materials (Ni$_{1-x}$Co$_x$Fe$_2$O$_4$ nanocrystals) require less energy to excite spin states, which corresponds to higher frequencies. High resonance field materials (Ni$_{1-x}$Zn$_x$Fe$_2$O$_4$ nanoparticles) require more energy to excite spin states, corresponding to lower frequencies.

The ferromagnetic resonance spectra of Ni$_{1-x}$M$_x$Fe$_2$O$_4$ nanoparticles can be divided into low anisotropy (Ni$_{1-x}$Zn$_x$Fe$_2$O$_4$) and high anisotropy (Ni$_{1-x}$Co$_x$Fe$_2$O$_4$) systems. Low anisotropy Ni$_{1-x}$Zn$_x$Fe$_2$O$_4$ series the FMR field correlates with increased molar

69
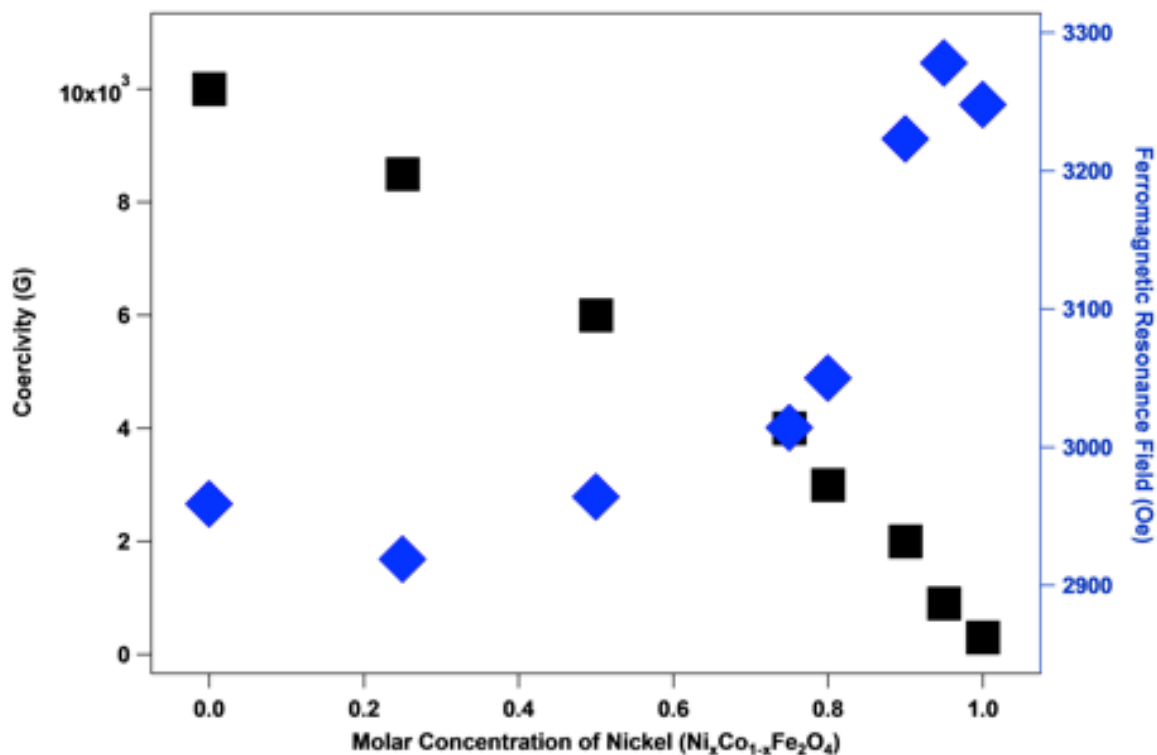
Figure 3-8: Plots the coercivity and ferromagnetic resonance field as a factor of molar concentration of nickel in mixed composition Ni$_{1-x}$Co$_x$Fe$_2$O$_4$ nanocrystals.

concentration of zinc shifting from lower resonance field of H = 3200 Oe for NiFe$_2$O$_4$ to higher field H = 3400 Oe for ZnFe$_2$O$_4$ (**Figure 3-5**). The entire nickel-zinc ferrite series demonstrated high absorption intensities with narrow linewidths (ΔH < 1100 Oe). The FMR properties of high anisotropy Ni$_{1-x}$Co$_x$Fe$_2$O$_4$ nanocrystals correlate strongly with the increased molar concentration of cobalt causing weakened absorption intensity broadening of linewidth, and resonance field shifts from 3200 Oe to 2400 Oe (**Figure 3-6**). The strong S-L coupling of Co^{2+} cations increases the linewidth and shifts the resonance field to lower fields can be attributed to increased magnetocrystalline anisotropy energy of Ni$_{1-x}$Co$_x$Fe$_2$O$_4$ nanocrystals. **Figure 3-8** shows a correlation between the FMR properties of linewidth and absorption intensity with the magnetic coercivity of Ni$_{1-x}$Co$_x$Fe$_2$O$_4$ nanocrystals. The magnetocrystalline anisotropy energy of a superparamagnetic nanoparticle can be used to

predict ferromagnetic resonance properties and design materials to meet technological needs.

Table 3-1: Ferromagnetic resonance and magnetic data for mixed composition $Ni_{1-x}M_xFe_2O4$ (M = Zn^{2+} and Co^{2+})

Sample	Stoichiometry T-XRF	Crystallite Size XRD (nm)	T_B	H_C (Oe)	M_S (emu/g)	M_R (emu/g)	Resonance Field (Oe)	Linewidth (Oe)
$ZnFe_2O_4$	$Zn_1{:}Fe_2$	5.8	45	150	87.1	16.7	3444	795
$Ni_{.25}Zn_{.75}Fe_2O_4$	$Ni_{.31}{:}Zn_{.63}{:}Fe_{2.06}$	6.5	45	N/A	N/A	N/A	3309	1144
$Ni_{.5}Zn_{.5}Fe_2O_4$	$Ni_{.6}{:}Zn_{.45}{:}Fe_{1.95}$	5.5	35	100	58.5	9.8	3308	965
$Ni_{.75}Zn_{.25}Fe_2O_4$	$Ni_{.83}{:}Zn_{.26}{:}Fe_{1.9}$	6.0	35	N/A	N/A	N/A	3279	970
$NiFe_2O_4$	$Ni_{.97}{:}Fe_{2.06}$	6.0	45	300	32.4	11.5	3248	705
$Ni_{.75}Co_{.25}Fe_2O_4$	$Ni_{.78}{:}Co_{.23}{:}Fe_{1.93}$	5.8	135	3700	53.7	31.4	3015	2700
$Ni_{.5}Co_{.5}Fe_2O_4$	$Ni_{.5}{:}Co_{.45}{:}Fe_{2.05}$	5.7	175	5700	59.1	35.5	2965	2775
$Ni_{.25}Co_{.75}Fe_2O_4$	$Ni_{.3}{:}Co_{.72}{:}Fe_{1.98}$	5.6	185	8500	52.4	31.5	2919	3260
$CoFe_2O_4$	$Co_{.96}{:}Fe_{2.07}$	5.1	225	10,000	62.9	35.4	2850	3460

3.4 Conclusions

In summary, we have systematically characterized the superparamagnetic and ferromagnetic resonance properties of $NiFe_2O_4$ and a series of mixed solid solutions $Ni_xM_{1-x}Fe_2O_4$ (M = Zn^{2+} and Co^{2+}). Native $NiFe_2O_4$ nanocrystals exhibit size-dependent increases in blocking temperature below 100 K. The substitution of d^{10} Zn^{2+} cations into $Ni_xZn_{1-x}Fe_2O_4$ nanocrystals has little effect on the blocking temperature but upon field-dependent magnetization measurements at 5 K the increased molar concentrations of zinc increased the saturation and remanent magnetizations. For similarly sized nanoparticles substitution of strong L-S coupled Co^{2+} cations into the $Ni_xCo_{1-x}Fe_2O_4$ nanocrystals increases the magnetocrystalline anisotropy increasing the blocking temperatures and magnetic susceptibility of the samples. These nanoparticles also show Co^{2+} concentration dependent increases to coercivity, saturation, and remanent magnetizations.
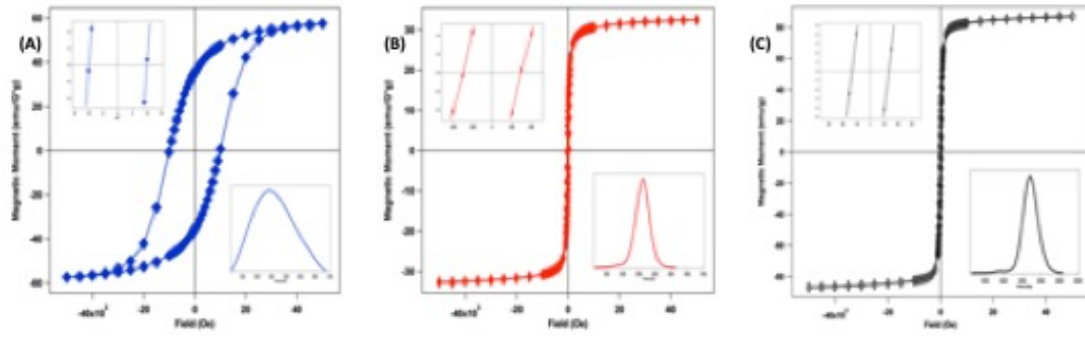
Figure 3-9: Field dependent magnetic hysteresis loops with ferromagnetic resonance profile inlaid for $CoFe_2O_4$ (A), $NiFe_2O_4$ (B), and $ZnFe_2O_4$ (C) nanocrystals

Ferromagnetic resonance measurements of these single domain nanocrystals showed trends that link the resonance field and linewidth with the magnetocrystalline anisotropy of the material.   Nanoparticles with large magnetocrystalline anisotropy energies as shown by the SQUID measurements such as $CoFe_2O_4$ shift the resonance field to lower fields, but with increased losses (broad linewidth and suppressed the absorption intensity).   Low magnetocrystalline anisotropy energy samples ($Ni_{1-x}Zn_xFe_2O_4$ nanocrystals) absorb at higher resonance fields with increased absorption intensity and narrow linewidths.   This study shows that through fundamental studies of low and high anisotropy single-domain magnetic nanocrystals a greater understanding of superparamagnetism and ferromagnetic resonance can be applied to the selection of materials for the development of novel telecommunication technologies.

3.5 REFERENCES

1.   David R. Baselt, G. U. L., Mohan Natesan, Steven W. Metzger, Paul E. Sheehan, Richard J. Colton, A Biosensor Based on Magnetoresistance Technology. *Biosens Bioelectron.* **1998,** *13*, 731-739.

2.   Jang, J. T.; Nah, H.; Lee, J. H.; Moon, S. H.; Kim, M. G.; Cheon, J., Critical enhancements of MRI contrast and hyperthermic effects by dopant-controlled magnetic nanoparticles. *Angew Chem Int Ed Engl* **2009,** *48* (7), 1234-8.

3.   Von Sovskii, S. V., Ferromagnetic Resonance: The Phenomenon of Resonant Absorption of a High-Frequency Magnetic Field Ferromagnetic Substances. *Elsevier, LTD.* **2016**, 1-340.

4.   Tiano, A. L.; Papaefthymiou, G. C.; Lewis, C. S.; Han, J.; Zhang, C.; Li, Q.; Shi, C.; Abeykoon, A. M. M.; Billinge, S. J. L.; Stach, E.; Thomas, J.; Guerrero, K.; Munayco, P.; Munayco, J.; Scorzelli, R. B.; Burnham, P.; Viescas, A. J.; Wong, S. S., Correlating Size and Composition-Dependent Effects with Magnetic, Mössbauer, and Pair Distribution Function Measurements in a Family of Catalytically Active Ferrite Nanoparticles. *Chem Mater.* **2015,** *27* (10), 3572-3592.

5.   Young-Wook Jun, J.-W. S., Jinwoo Chen, Nanoscaling Laws of Magnetic Nanoparticles and Their Applicabilities in Biomedical Sciences. *Acc Chem Res.* **2007,** *41* (2), 179-189.

6.   Young, C. C.; Blackley, B. W.; Porter, M. D.; Granger, M. C., Frequency-Domain Approach To Determine Magnetic Address-Sensor Separation Distance Using the Harmonic Ratio Method. *Anal Chem* **2016,** *88* (4), 2015-20.

7.   Chao Liu, B. Z., Adam J. Rondinone, and Z. John Zhang, Chemical Control of Superparamagnetic Properties of Magnesium and Cobalt Spinel Ferrite Nanoparticles through Atomic Level Magnetic Couplings. *J Am Chem Soc* **2000,** *122*, 6263-6267.

8.   Tannous, C.; Gieraltowski, J., The Stoner–Wohlfarth model of ferromagnetism. *Euro J Phys.* **2008,** *29* (3), 475-487.

9.   O'Handley, R. C., Modern Magnetic Materials: Principles and Applications. *John Wiley & Sons, INC.* **2000**, 764.

10.   Song, Q.; Zhang, Z. J., Correlation between Spin-Orbital Coupling and the Superparamagnetic Properties of Magnetite and Cobalt Ferrite Spinel Nanocrystals. *J Phys Chem B.* **2006,** *110*, 11205-11209.

11.   Özgür, Ü.; Alivov, Y.; Morkoç, H., Microwave ferrites, part 1: fundamental properties. *J Mat Sci: Mat Electron.* **2009,** *20* (9), 789-834.

12.   Hongseok Yun, X. L., Taejong Paik, Duraivelan Palanisamy, Jungkwun Kim, William D. Vogel, Arthur J. Viescas, Jun Chen, Georgia C. Papefthymiou, James M. Kikkawa, Mark G. Allen, and Christopher B. Murray, Size- and Composition-Dependent Radio Frequency Magnetic Permeability of Iron Oxide Nanocrystals. *ACS Nano* **2014,** *8* (12), 12323-12337.

13.   Chen, H. W., Aminolytic Synthesis and Ferromagnetic Resonance of Cobalt and Manganese Based Spinel Ferrite Nanoparticles. **2018**, 148.

14.   McMichael, R. D.; Stiles, M. D.; Chen, P. J.; Egelhoff, W. F., Ferromagnetic resonance linewidth in thin films coupled to NiO. *Journal of Applied Physics* **1998,** *83* (11), 7037-7039.

15.   Liu, W.; Liu, M.; Ma, R.; Zhang, R.; Zhang, W.; Yu, D.; Wang, Q.; Wang, J.; Wang, H., Mechanical Strain-Tunable Microwave Magnetism in Flexible CuFe2O4Epitaxial Thin Film for Wearable Sensors. *Advanced Functional Materials* **2018,** *28* (10).

16.   De Biasi, E.; Ramos, C. A.; Zysler, R. D.; Romero, H., Ferromagnetic resonance in amorphous nanoparticles. *Physica B: Condensed Matter* **2004,** *354* (1-4), 286-289.

17.   Chen, Y.; Fan, X.; Zhou, Y.; Xie, Y.; Wu, J.; Wang, T.; Chui, S. T.; Xiao, J. Q., Designing and tuning magnetic resonance with exchange interaction. *Adv Mater* **2015,** *27* (8), 1351-5.

18.   Mattei, J.-L.; Le Guen, E.; Chevalier, A.; Tarot, A.-C., Experimental determination of magnetocrystalline anisotropy constants and saturation magnetostriction constants of NiZn and NiZnCo ferrites intended to be used for antennas miniaturization. *Journal of Magnetism and Magnetic Materials* **2015,** *374*, 762-768.

19.   Babu, K. V.; Sailaja, B.; Jalaiah, K.; Shibeshi, P. T.; Ravi, M., Effect of zinc substitution on the structural, electrical and magnetic properties of nano-structured Ni 0.5 Co 0.5 Fe 2 O 4 ferrites. *Physica B: Condensed Matter* **2018,** *534*, 83-89.

20.   Rondinone, A. J.; Liu, C.; Zhang, Z. J., Determination of Magnetic Anisotropy Distribution and Anisotropy Constant of Manganese Spinel Ferrite Nanoparticles. *The Journal of Physical Chemistry B* **2001,** *105* (33), 7967-7971.

21.   Kittel, C., Introduction to Solid State Physics, 8th Edition. **2004**, 704.

CHAPTER 4: FERROMAGNETIC RESOANNCE STUDIES OF EXCHANGE-COUPLED HARD/SOFT FERRIMAGNETIC CORE@SHELL SPINEL FERRITE NANOCRYSTALS

4.1 Introduction

Core@shell architecture has been extensively studied in nanoparticle systems to elicit fundamental scientific understanding of material interactions. Typical nanoparticle design routes such as varying the size, morphology, or chemical composition are restricted by uniformity in magnetic structure. Through consideration of material combinations and structural ordering of core/shell phase synthesis of magnetic core@shell nanoparticles can address competing technical requirements of magnetic properties such as coercivity and the thermal stability of magnetization.[1, 2]   Exchange spring magnets designed with core@shell architectures have been researched to improve energy product of rare-earth free permanent magnets.[3-6] Core@shell nanoparticles have also been explored as a solution "superparamagnetic limitations" in magnetic recording media applications through
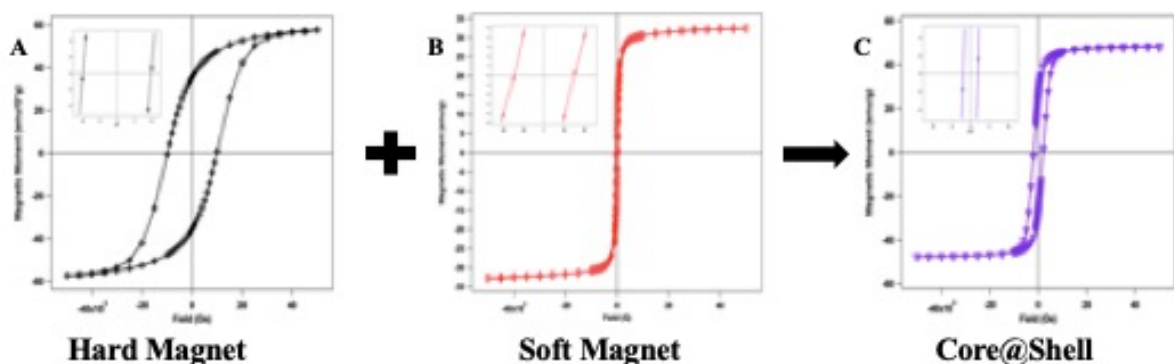
Figure 4-1: Field dependent magnetic hysteresis loops measured at 5 K of CoFe$_2$O$_4$ (A), NiFe$_2$O$_4$ (B), and CoFe$_2$O$_4$@NiFe$_2$O$_4$ (C) nanoparticles

overcoming the thermal stability issues of nanoscale ferromagnets.[4, 7] Exploration of various core@shell combinations of magnetic materials will provide better fundamental understanding of magnetic interactions and further synthetic design approaches for desired characteristics across a myriad of applications from permanent magnets, hyperthermia treatments, and catalysis.[8, 9]

Reports on the synthesis of bimagnetic core@shell nanoparticles have been achieved through reduction-surface oxidation and seed-mediated thermal decomposition.[1, 10] Reductive synthesis method of metallic nanocrystals with controlled surface oxidation have yielded core@shell nanocrystals (Co@CoO, Ni@NiO, $Fe@Fe_2O_3$ and etc.) that exhibit unique exchange bias magnetic behavior arising from the spin-spin interactions of the ferromagnetic metallic cores with the antiferromagnetic monoxide surface.[11-13] This method is extremely limited in combination of materials available and core/shell structure ordering and additionally the process of surface oxidation is difficult to control yielding nanoparticles lacking uniformity in core/shell volume ratios.[10] Seed-mediated thermal decomposition synthesis opens the design window to a wider range of material combinations allowing for research into various core@shell nanoparticle combinations such as hard/soft spinel ferrites, hard/soft metals/alloys, and metal core with metal oxide shell.[1, 5, 9, 10, 14] The vast research contributions on novel core@shell nanoparticles from various synthetic methods makes it difficult to draw conclusions on the magnetic properties of various core@shell material combinations.[15, 16] Approaching core@shell nanoparticles through a systematic study of core-shell material combinations and dimensions is essential to provide insight into the interaction of hard and soft magnetic phases.

Spinel ferrites are heavily research class of ferrimagnetic materials with well-established knowledge demonstrating control of nanoscale magnetic properties by varying size, morphology, and chemical composition.[14, 17-19]   For this study we have chosen to investigate a magnetically hard spinel ferrite of $CoFe_2O_4$ that possesses a large magnetocrystalline anisotropy constant of $k > 10^5$ J/m^3 and magnetically soft $NiFe_2O_4$ with a smaller magnetocrystalline anisotropy constant $k \sim 10^3$ J/m^3.[20]   The largely uniform crystallographic structure among different composition spinel ferrites lends to epitaxially growth of core@shell nanocrystals through seeded growth methods.   Additionally, we reported a systematic study of mixed solid solution $Ni_{1-x}Co_xFe_2O_4$ nanocrystals for their magnetic and ferromagnetic resonance properties by varying parameter of size and chemical composition (**Chapter III**).   Studying various combinations of bimagnetic core@shell architecture nanocrystals can further the fundamental understanding of magnetic spin-spin interactions in interfaced hard/soft magnetic materials.

Microwave ferrites are a technologically important class of high resistance magnetic materials including hexaferrites, garnets, and spinel ferrites that absorb radio frequencies.[21] Ferromagnetic resonance spectroscopy studies of hard/soft spinel ferrite nanocrystals of various chemical compositions have established correlations between the absorption of microwave and the magnetocrystalline anisotropy energy of the material.[19]   Probing core@shell architecture nanocrystals through ferromagnetic resonance spectroscopy could elicit further fundamental understanding of exchange coupled magnetic materials and establish advanced synthetic design for novel materials for antennae and sensors.

Herein, we report the systematic study of bimagnetic core@shell nanocrystals composed of hard/soft $CoFe_2O_4/NiFe_2O_4$ via the seed-mediated aminolytic methodology.

The synthesized $NiFe_2O_4$@$CoFe_2O_4$ and inverted $CoFe_2O_4$@$NiFe_2O_4$ nanocrystals exhibit unique magnetic properties derived from the ordering of the core/shell architecture. The volume of the hard/soft magnetic phases has been varied in both core/shell systems in order to further study exchange coupling interactions of the core/shell materials. Magnetic properties such as the blocking temperature (T_B) and coercivity (H_C) can be tailored by inversion of the core/shell order and by varying the volume of core/shell materials. We can also demonstrate that the ferromagnetic resonance properties such as resonance field and linewidth are dependent on the magnetic structure of the shell phase and can be tuned in a similar manner to the coercivity.

4.2 Experimental

4.2.1 Synthesis of Spinel Ferrite core nanocrystals

To prepare 5 nm $NiFe_2O_4$ and $CoFe_2O_4$ nanocrystals, 12 mmol of mixed metal acetate precursor, 20 mL of oleylamine, and 60 mL of dibenzyl ether to a 3-neck round bottom flask. The reaction mixture is stirred and refluxed at 140°C for 1 hour. After 1 hour of mixing a flow of O_2 gas to the reaction vessel and refluxed at 220°C for 1 hour. The reaction is cooled and collected via centrifuge and washed with ethanol to remove excess organics from the synthesized nanocrystals.

4.2.2 Seed-Mediated growth of large core@shell nanoparticles

To prepare core@shell architecture nanocrystals, 500 mg of $NiFe_2O_4$ core nanoparticles, 12 mmol of metal acetate ($CoFe_2$) precursor, 20 mL of oleylamine, and 60 mL of dibenzyl ether to a 3-neck round bottom flask. Repeat the synthetic procedure for

the core nanoparticles and interchange core nanocrystals and shell reagents for variable core/shell combinations.

4.2.3   Instrumentation

Sample crystallinity and phase purity was measured with powder x-ray diffraction on a Bruker D8 Advance diffractometer. A superconducting quantum inference device (SQUID) magnetometer (Quantum Design MPMS-5S) with an applied magnetic field up to 5 T at temperature range of 2-400 K was used to perform both temperature and magnetic field dependent magnetization measurements. The temperature range was measured from 5 to 315 K. Field-dependent magnetic measurements were prepared by dispersing the dry nanocrystal powder in eicosane (Aldrich, 99%) to stabilize and eliminate interparticle interaction effects.

4.3 Results and Discussion

Bimagnetic core@shell nanocrystals were synthesized via a seed-mediated aminolytic technique allowing for various combinations of core@shell materials. Powder x-ray diffraction confirms all seeds and core@shell nanocrystals are of spinel ferrite crystal structure (**Figure 4-2**). The Scherrer equation confirmed the size of the seed and the core@shell nanoparticles.

The temperature dependence of magnetic susceptibility of $NiFe_2O_4@CoFe_2O_4$ and inverted $CoFe_2O_4@NiFe_2O_4$ nanoparticles from 5 to 305 K are shown in **Figures 4-3, 4-4**. All core@shell nanoparticle samples of both architectures demonstrate a single maximum or blocking temperature (T_B) concluding successful exchange coupling interaction between
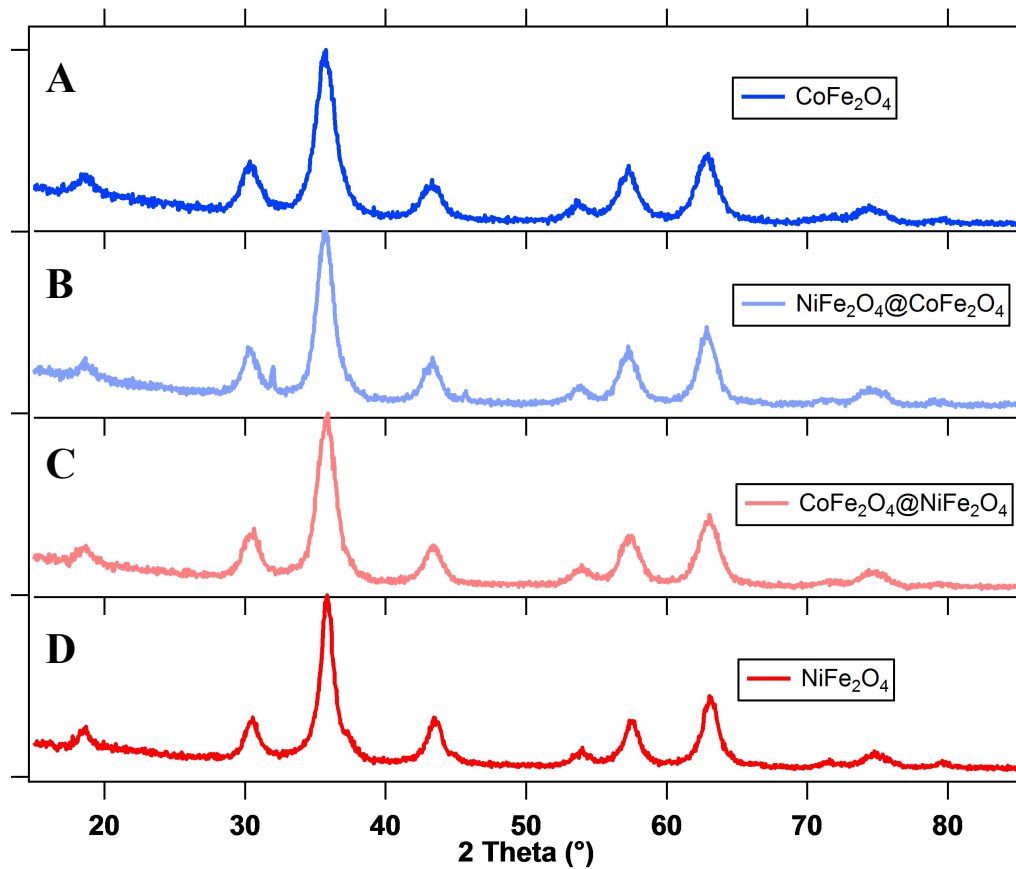
Figure 4-2: XRD pattern of core nanocrystals (A) CoFe$_2$O$_4$ and (D) NiFe$_2$O$_4$ and the core@shell architecture nanoparticles (B) NiFe$_2$O$_4$@CoFe$_2$O$_4$ and (C) CoFe$_2$O$_4$@NiFe$_2$O$_4$.

the core and shell materials. The seed NiFe$_2$O$_4$ nanocrystals exhibit a blocking temperature of 45 K, which was elevated with the introduction of a CoFe$_2$O$_4$ shell. The blocking temperature of NiFe$_2$O$_4$@CoFe$_2$O$_4$ nanoparticles increases with increased molar ration of CoFe$_2$O$_4$ shell (**Figure 4-4**). As shown in **Figure 4-3** seed CoFe$_2$O$_4$ nanocrystals

possess a higher blocking temperature of 245 K that increases with the initial introduction of ferrimagnetically soft NiFe$_2$O$_4$ shell but does decline upon increased shell-to-core molar ratio.
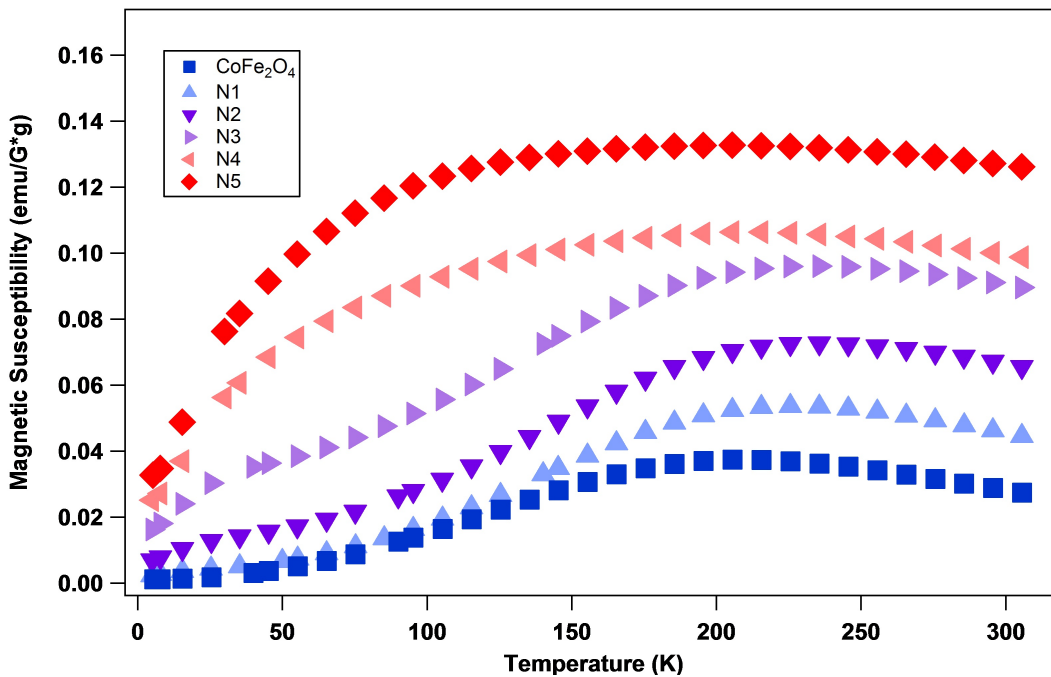
Figure 4-3: Temperature dependent magnetic susceptibility measurement of CoFe₂O₄ and CoFe₂O₄@NiFe₂O₄ nanoparticles with increasing shell thickness (N1-N5) measured from 5 to 305 K under 100 Oe applied field
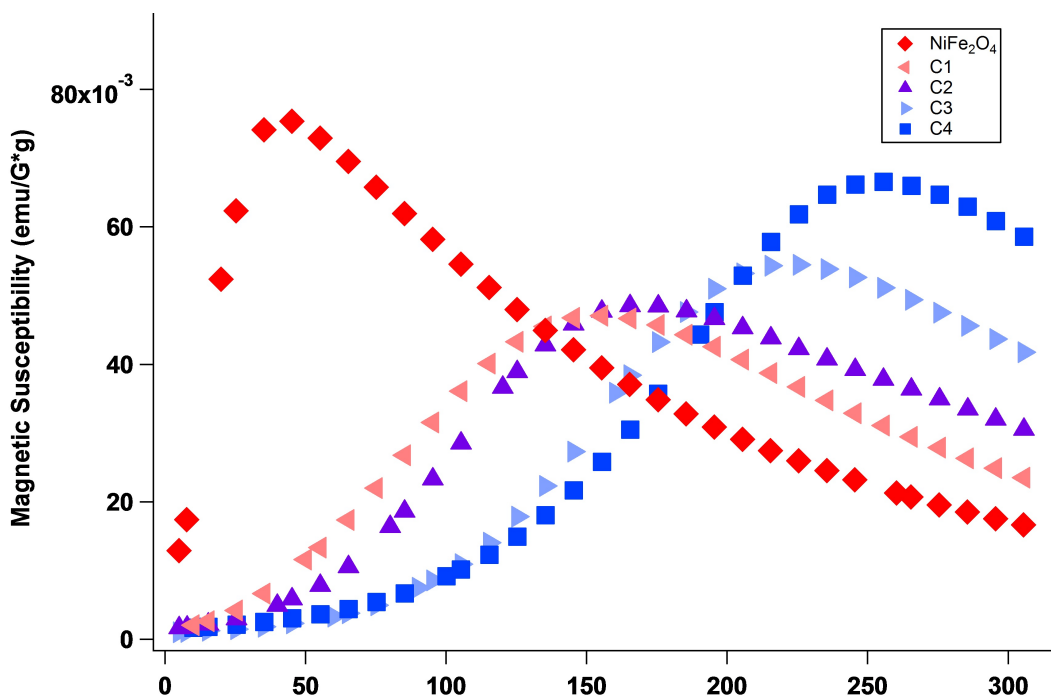
Figure 4-4: Temperature dependent magnetic susceptibility measurement of NiFe₂O₄ and NiFe₂O₄@CoFe₂O₄ nanoparticles with increasing shell thickness in order of C1-C4 measured from 5 to 305 K under 100 Oe applied field

Field-dependent magnetization measurements of $NiFe_2O_4@CoFe_2O_4$ and inverted $CoFe_2O_4@NiFe_2O_4$ nanoparticles measured at 5 K are shown in **Figures 4-5, 4-6**. The introduction of a hard ferrimagnetic $CoFe_2O_4$ shell to $NiFe_2O_4$ core results in increased coercivity, saturation, and remanent magnetizations over the native $NiFe_2O_4$ nanoparticle (**Figure 4-5**). Inversion of the core@shell architecture results in the reduction of coercivity, saturation, and remanent magnetizations in $CoFe_2O_4@NiFe_2O_4$ nanoparticles (**Figure 4-6**).

Ferromagnetic resonance (9.88 GHz) spectrums of both core@shell architecture nanoparticle systems measured at room temperature are shown in **Figures 4-7 and 4-8**. For $NiFe_2O_4@CoFe_2O_4$ nanoparticles with increased volume fraction of $CoFe_2O_4$ shell the ferromagnetic resonance field shifts to lower resonance fields, broadened linewidth, and reduces signal intensity (**Figures 4-7**). The inverted architecture of $CoFe_2O_4@NiFe_2O_4$ exhibits the exact opposite effect on ferromagnetic resonance properties as the volume fraction of the $NiFe_2O_4$ shell increases the resonance field shift higher, reduced linewidth, and increased signal intensity are observed (**Figures 4-8**).

The bimagnetic core@shell nanoparticle systems synthesized exhibit properties consistent with exchange coupled bilayers of magnetic materials such as a single blocking temperature and symmetrical magnetic hysteresis loops.

The $NiFe_2O_4$ core nanoparticles are a soft ferrimagnetic material with low magnetocrystalline anisotropy energy resulting in a coercivity of approximately 300 Oe with saturation magnetization of 32.4 emu/g. They also exhibit size-dependent superparamagnetic properties but for the seed size diameter of 5.5 nm the blocking
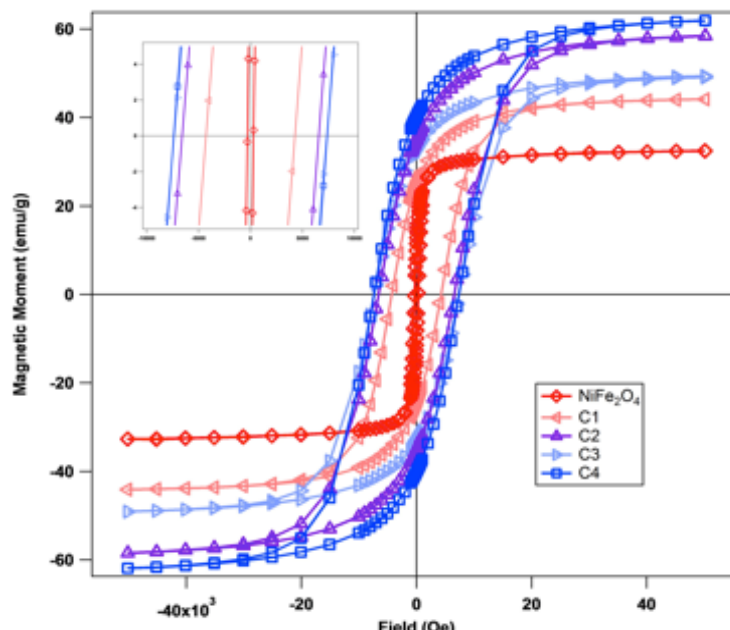
Figure 4-5: Field dependent magnetic hysteresis measurement of $NiFe_2O_4$ and $NiFe_2O_4@CoFe_2O_4$ nanoparticles with increasing shell thickness measured at 5 K with applied fields ranging from + 5 Telsa
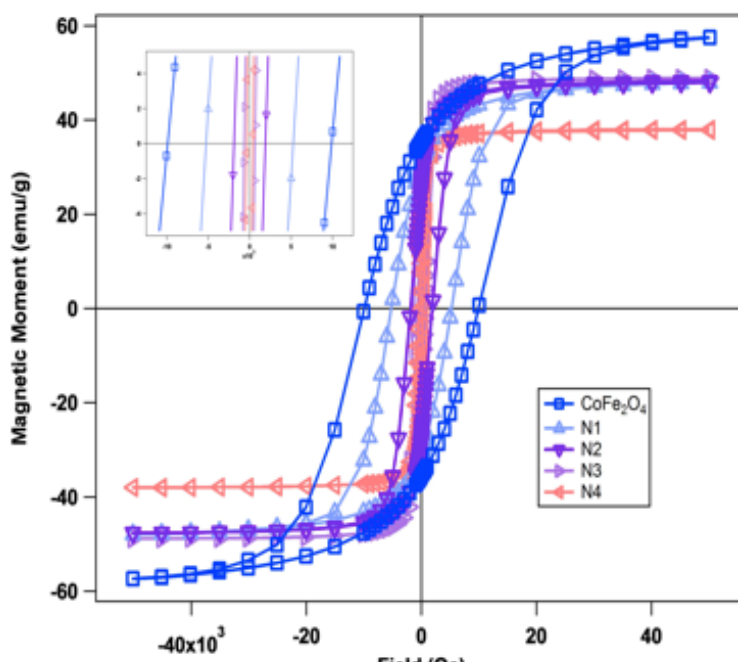
Figure 4-6: Field dependent magnetic hysteresis measurement of $CoFe_2O_4$ and $CoFe_2O_4@NiFe_2O_4$ nanoparticles with increasing shell thickness measured at 5 K with applied fields ranging from ± 5 Telsa

temperatures (T_B) of 45 K (**Figure 4-4**). Cobalt ferrite serves as a contrast being a hard ferrimagnet with strong spin-orbit coupling resulting in large magnetocrystalline anisotropy energy, a coercivity of 10,000 Oe, and saturation magnetization around 56.6 emu/g.[20, 22] Seed-mediated aminolytic synthesis allows for the epitaxial growth of hard $CoFe_2O_4$ shell onto the $NiFe_2O_4$ core nanoparticle with a strong interface between the hard/soft magnetic phases promoting exchange coupling. This technique can be applied various materials compatible with the synthetic method as well as inversion of the core@shell architecture to further investigate the roll of structure in exchange coupled nanomaterials.

Synthesis of a series of core@shell $NiFe_2O_4@CoFe_2O_4$ nanoparticles with variable thickness of $CoFe_2O_4$ shell was investigated for temperature dependent magnetic susceptibility in **Figure 4-4**. The introduction of any $CoFe_2O_4$ shell considerably elevates the T_B of the $NiFe_2O_4$ core nanoparticles, increased $CoFe_2O_4$ shell thickness results in further elevated blocking temperatures. The $CoFe_2O_4$ core of the inverted $CoFe_2O_4@NiFe_2O_4$ nanoparticles possesses a higher initial T_B = 225 K due to the larger magnetocrystalline anisotropy energy. The addition of the soft ferrimagnetic $NiFe_2O_4$ shell has little impact on the thermal stability of the $CoFe_2O_4$ core nanoparticle with only a slight T_B increase observed (**Figure 4-3**). The increased magnetic volume of both core@shell nanoparticle systems increases the magnetic susceptibility at 300 K. The thermal stability of the core@shell nanoparticles is independent of the architecture but instead dictated by the volume fraction with the largest magnetocrystalline anisotropy energy such as $CoFe_2O_4$ for the systems presented in the study.
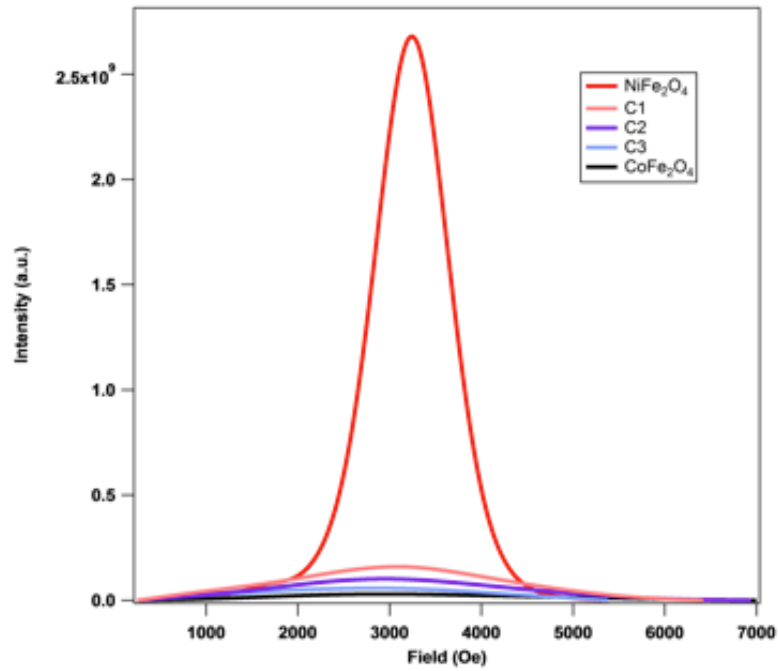
Figure 4-7: Overlaid integrated ferromagnetic resonance spectra of NiFe₂O₄, NiFe₂O₄@CoFe₂O₄, and CoFe₂O₄ nanoparticles measured frequency of 9.88 GHz with applied field swept from 250 to 10,000 Oe
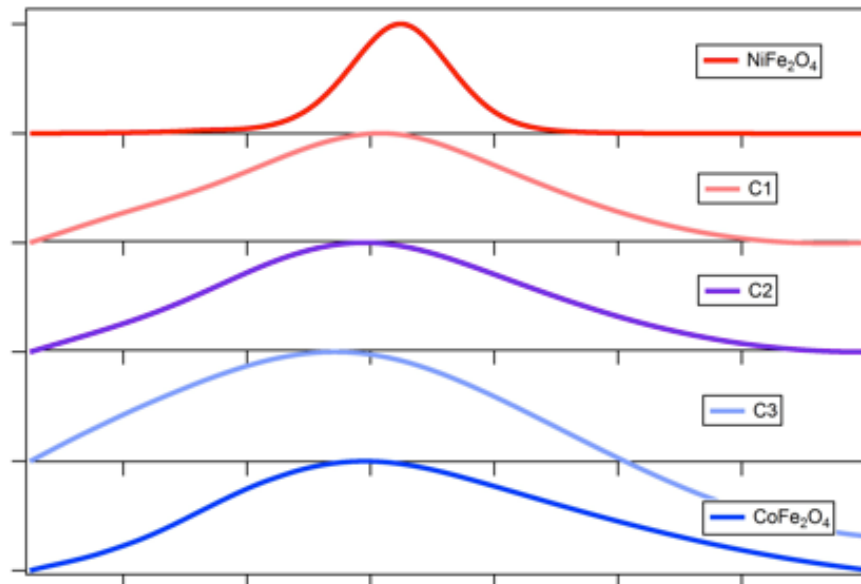
Figure 4-8: Normalized integrated ferromagnetic resonance spectra of NiFe₂O₄, NiFe₂O₄@CoFe₂O₄, and CoFe₂O₄ nanoparticles measured frequency of 9.88 GHz with applied field swept from 250 to 10,000 Oe
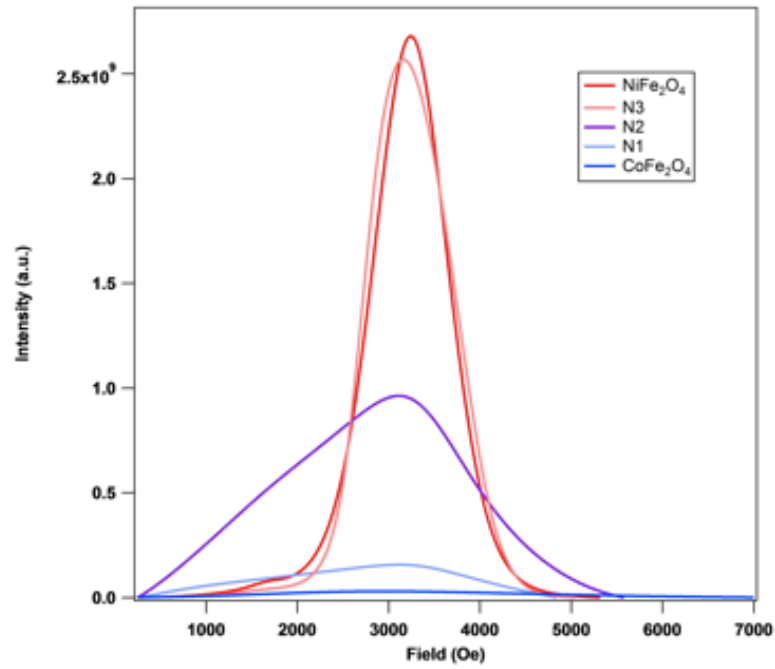
Figure 4-9: Overlaid integrated ferromagnetic resonance spectra of NiFe₂O₄, NiFe₂O₄@CoFe₂O₄, and CoFe₂O₄ nanoparticles measured frequency of 9.88 GHz with applied field swept from 250 to 10,000 Oe
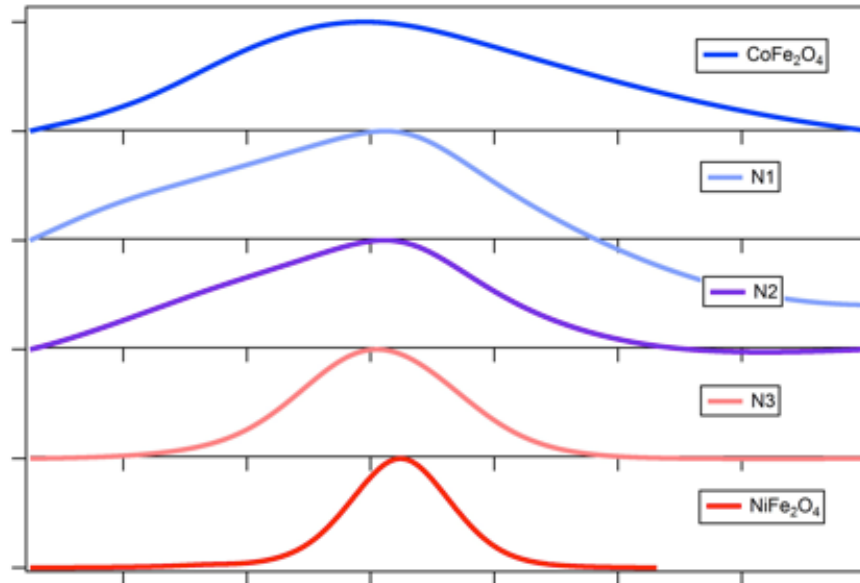
Figure 4-10: Normalized integrated ferromagnetic resonance spectra of NiFe₂O₄, NiFe₂O₄@CoFe₂O₄, and CoFe₂O₄ nanoparticles measured frequency of 9.88 GHz with applied field swept from 250 to 10,000 Oe

Field-dependent magnetization measurements of core@shell nanoparticles exhibit magnetic hysteresis loops consistent with single-phase magnetic material concluding strong core@shell exchange coupling interaction. For $NiFe_2O_4$@$CoFe_2O_4$ nanoparticle the soft $NiFe_2O_4$ core possesses a $H_C = 300$ Oe, $M_s = 32.4$ emu/g, and $M_r = 11.5$ emu/g (**Figure 4-5**). As shown in **Figure 4-5** the introduction of $CoFe_2O_4$ shell increases the coercivity, saturation, and remanent magnetizations and correlates with increased shell volume fraction. A thin $CoFe_2O_4$ shell (<0.5 nm) enhances the coercivity of the core $NiFe_2O_4$ considerably with sequentially thicker shells further increasing the coercivity of the system. The magnetic properties of $NiFe_2O_4$@$CoFe_2O_4$ are a product of exchange coupling interaction between the two materials providing yielding hybrid magnetic properties that can be tuned through control of the shell volume fraction.

The inverted $CoFe_2O_4$@$NiFe_2O_4$ demonstrate the opposite trend for coercivity, saturation, and remanent magnetizations with all three properties decreasing as the shell volume fraction of $NiFe_2O_4$ increases (**Figure 4-6**). A critical shell thickness (> 6.0 nm) was achieved for sample **N4** in which exchange-coupling interaction of the core/shell weakens resulting the magnetic spin relaxation mechanism reverting to that of native $NiFe_2O_4$ nanoparticle. The thermal stability of sample **N4** ($T_B = 240$ K) is consistent with the $CoFe_2O_4$ core. Bimagnetic core@shell nanoparticles possess an exchange coupled dominated spin relaxation mechanism until the shell thickness exceeds a critical point the relaxation mechanism of the shell phase becomes dominate as observed in samples **N4/5**. Spin-spin interactions produced in exchange coupled magnetic layers has effective ranges that can be exceeded as demonstrated in sample **N4** as these samples spin relaxation mechanism is reflective of native $NiFe_2O_4$ while the thermal stability of the $CoFe_2O_4$ core

Table 4-1: **Magnetic and ferromagnetic resonance properties of NiFe₂O₄@CoFe₂O₄ nanoparticles**

Sample	Shell Depth (nm)	T_B (K)	X @ 300 K (emu/G*g)	H_C (Oe)	Resonance Field (Oe)	ΔH (Oe)
NiFe₂O₄		40	0.019	300	3248	705
C1	0.3	155	0.023	4000	3084	2802
C2	0.6	165	0.048	6500	2953	2955
C3	1.7	225	0.042	7000	2709	3020
C4	2.5	255	0.059	7000	2807	3140
CoFe₂O₄		210	0.029	10,000	2846	3460
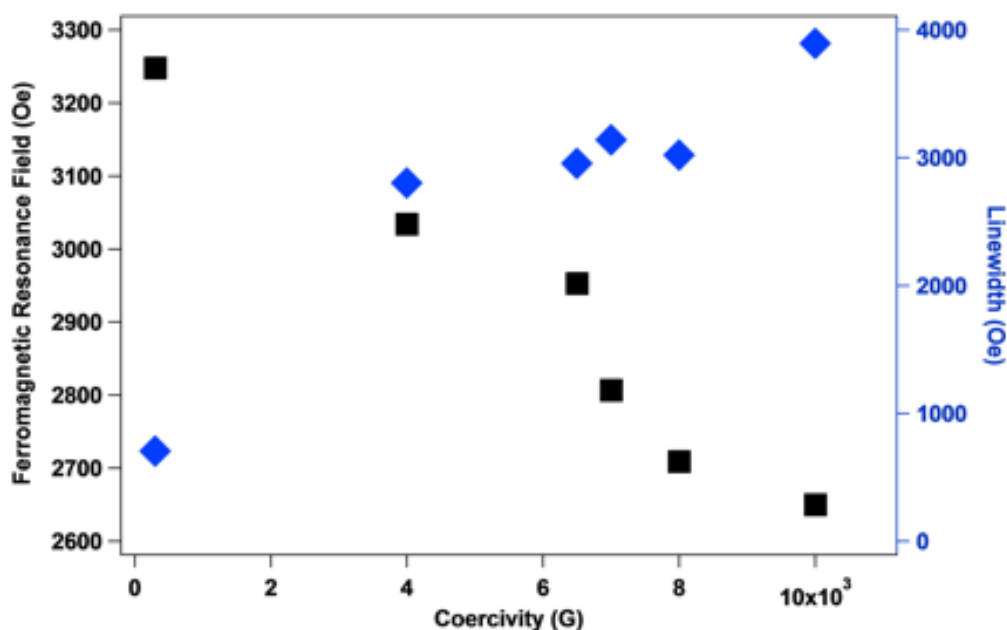
Figure 4-11: **Ferromagnetic resonance field and linewidth of NiFe₂O₄@CoFe₂O₄ nanoparticles as a function of coercivity.**

is maintained. The field-dependent magnetic properties of coercivity, saturation, and remanent magnetizations are heavily subject to the order of core/shell materials with the shell material properties dictate the magnetic spin relaxation mechanism of the core@shell architecture.

Table 4-2: Magnetic and ferromagnetic resonance properties of CoFe$_2$O$_4$@NiFe$_2$O$_4$ nanoparticles

Sample	Shell Depth (nm)	T$_B$ (K)	X @ 300 K (emu/G*g)	H$_C$ (Oe)	Resonance Field (Oe)	ΔH (Oe)
CoFe$_2$O$_4$		210	0.029	10,000	2846	3460
N1	1.9	225	0.045	5000	3116	2630
N2	4.8	235	0.066	4000	3110	2474
N3	6.8	235	0.090	650	3051	1510
N4	7.1	215	0.077	400	3151	1109
NiFe$_2$O$_4$		40	0.019	300	3248	705
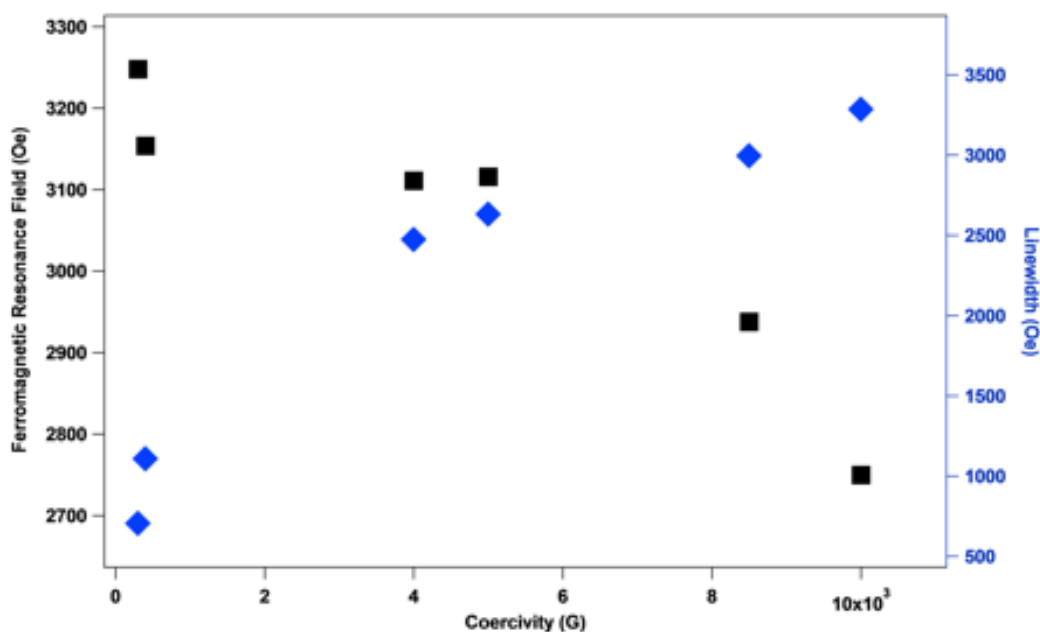
Figure 4-12: Ferromagnetic resonance field and linewidth of inverted-CoFe$_2$O$_4$@NiFe$_2$O$_4$ nanoparticles as a function of coercivity.

Ferromagnetic resonance spectroscopy probes unique magnetic behavior by subjecting a sample to a set microwave frequency while sweeping the applied magnetic field until the precision conditions are met for excitation of magnetic spins in the sample. The magnetic structure of a material will produce a unique FMR spectrum with distinct resonance field, linewidth, and absorption intensity. Mixed solid-solution Ni$_{1-x}$Co$_x$Fe$_2$O$_4$

have previously been reported revealing a correlation between the coercivity with the linewidth and absorption intensity of the FMR spectrum (**Chapter III**). For NiFe$_2$O$_4$@CoFe$_2$O$_4$ nanoparticles with increasing CoFe$_2$O$_4$ shell thickness the FMR spectra shifts toward CoFe$_2$O$_4$ dominate nature with low resonance field, broad linewidth, and suppressed absorption intensity (**Figure 4-7**). The large magnetocrystalline anisotropy energy of CoFe$_2$O$_4$ has a dominate effect over NiFe$_2$O$_4$ core even with a small volume fraction (shell < 0.5 nm) causing broadened the linewidth and reduced absorption intensity of the NiFe$_2$O$_4$@CoFe$_2$O$_4$ nanoparticles as in sample **C1**.

Inverted CoFe$_2$O$_4$@NiFe$_2$O$_4$ nanoparticles demonstrate the opposite magnetic behavior with increased NiFe$_2$O$_4$ shell thickness shifting the FMR properties toward that of native NiFe$_2$O$_4$ nanoparticles such as high resonance field, narrow linewidth, and increased absorption intensity (**Figure 4-8**). Samples that exceed the critical shell thickness in CoFe$_2$O$_4$@NiFe$_2$O$_4$ nanoparticles as observed in field-dependent magnetization measurements such as sample **N4** show a limitation to microwave absorption as the core/shell exchange coupled interaction is exceeded. Sample **N4** demonstrates similar FMR properties and field-dependent magnetization properties to native NiFe$_2$O$_4$ while possessing thermal stability properties of the CoFe$_2$O$_4$ core. The unique magnetic properties achievable via exchange-coupled core@shell nanoparticles opens the design space for novel materials that meet opposed technical demands.

4.4 Conclusion

We have demonstrated the controlled synthesis of NiFe$_2$O$_4$@CoFe$_2$O$_4$ and inverted CoFe$_2$O$_4$@NiFe$_2$O$_4$ core/shell nanoparticles. These core@shell architecture nanocrystals

provide a novel strategic design to generate unique magnetic properties capable of meeting technological demands. Thermal stability of core@shell nanoparticles is determined by the magnetocrystalline anisotropy energy of the hard phase $CoFe_2O_4$ and is independent of ordering of core/shell materials. The coercivity, saturation, and remanent magnetizations of a core@shell nanoparticle are hybridized properties produced by exchange coupling of the core/shell phases. Ordering of core/shell materials effects the magnetic spin relaxation mechanism observed in exchange coupled core@shell nanoparticles dictated by the material composition of the shell phase. Exchange coupled magnetic bilayers are subject to dynamic coupling range at which exchange coupling interactions weaken and the soft ferrimagnetic phase retains its magnetic properties. Ferromagnetic resonance probes demonstrate unique magnetic properties of resonance field, linewidth, and absorption intensity are tunable through exchange coupling of $NiFe_2O_4$@$CoFe_2O_4$ and inverted $CoFe_2O_4$@$NiFe_2O_4$ nanoparticles. The magnetic structure of the core@shell nanoparticle will surface determines the magnetic spin relaxation mechanism and interaction with microwave radiation. The core@shell architecture of bimagnetic nanoparticles provides a synthetic approach to achieve materials with magnetic properties for technology such as spring exchange magnets, sensors, and telecommunications.

4.5 REFERENCES

1.   Song, Q.; Zhang, Z. J., Controlled synthesis and magnetic properties of bimagnetic spinel ferrite CoFe2O4 and MnFe2O4 nanocrystals with core-shell architecture. *J Am Chem Soc* **2012,** *134* (24), 10182-90.

2.   Fabris, F.; Lima, E.; De Biasi, E.; Troiani, H. E.; Vasquez Mansilla, M.; Torres, T. E.; Fernandez Pacheco, R.; Ibarra, M. R.; Goya, G. F.; Zysler, R. D.; Winkler, E. L., Controlling the dominant magnetic relaxation mechanisms for magnetic hyperthermia in bimagnetic core-shell nanoparticles. *Nanoscale* **2019,** *11* (7), 3164-3172.

3.   Granados-Miralles, C.; Saura-Muzquiz, M.; Andersen, H. L.; Quesada, A.; Ahlburg, J. V.; Dippel, A. C.; Canevet, E.; Christensen, M., Approaching Ferrite-Based Exchange-Coupled Nanocomposites as Permanent Magnets. *ACS Appl Nano Mater* **2018,** *1* (7), 3693-3704.

4.   Manjura Hoque, S.; Srivastava, C.; Kumar, V.; Venkatesh, N.; Das, H. N.; Saha, D. K.; Chattopadhyay, K., Exchange-spring mechanism of soft and hard ferrite nanocomposites. *Materials Research Bulletin* **2013,** *48* (8), 2871-2877.

5.   Li, D.; Wang, H.; Ma, Z.; Liu, X.; Dong, Y.; Liu, Z.; Zhang, T.; Jiang, C., FePt/Co core/shell nanoparticle-based anisotropic nanocomposites and their exchange spring behavior. *Nanoscale* **2018,** *10* (8), 4061-4067.

6.   Eric E. Fullerton, J. S. J., S.D. Bader, Hard/soft Magnetic Heterostructures: Model Exchange-spring Magnets. *Journal of Magnetism and Magnetic Materials* **1999,** *200*, 392-404.

7.   López-Ortega, A.; Estrader, M.; Salazar-Alvarez, G.; Roca, A. G.; Nogués, J., Applications of exchange coupled bi-magnetic hard/soft and soft/hard magnetic core/shell nanoparticles. *Physics Reports* **2015,** *553*, 1-32.

8.   Lee, J. H.; Jang, J. T.; Choi, J. S.; Moon, S. H.; Noh, S. H.; Kim, J. W.; Kim, J. G.; Kim, I. S.; Park, K. I.; Cheon, J., Exchange-coupled magnetic nanoparticles for efficient heat induction. *Nat Nanotechnol* **2011,** *6* (7), 418-22.

9.   Gavrilov-Isaac, V.; Neveu, S.; Dupuis, V.; Taverna, D.; Gloter, A.; Cabuil, V., Synthesis of Trimagnetic Multishell MnFe2 O4 @CoFe2 O4 @NiFe2 O4 Nanoparticles. *Small* **2015,** *11* (22), 2614-8.

10.   Lima, E.; Winkler, E. L.; Tobia, D.; Troiani, H. E.; Zysler, R. D.; Agostinelli, E.; Fiorani, D., Bimagnetic CoO Core/CoFe2O4 Shell Nanoparticles: Synthesis and Magnetic Properties. *Chemistry of Materials* **2012,** *24* (3), 512-516.

11.   Rinaldi-Montes, N.; Gorria, P.; Martínez-Blanco, D.; Fuertes, A. B.; Fernández Barquín, L.; Puente-Orench, I.; Blanco, J. A., Bridging exchange bias effect in NiO and Ni(core)@NiO(shell) nanoparticles. *Journal of Magnetism and Magnetic Materials* **2016,** *400*, 236-241.

12.   Kavich, D. W.; Dickerson, J. H.; Mahajan, S. V.; Hasan, S. A.; Park, J. H., Exchange bias of singly invertedFeO/Fe3O4core-shell nanocrystals. *Physical Review B* **2008,** *78* (17).

13.   González, J. A.; Andrés, J. P.; López Antón, R.; De Toro, J. A.; Normile, P. S.; Muñiz, P.; Riveiro, J. M.; Nogués, J., Maximizing Exchange Bias in Co/CoO Core/Shell Nanoparticles by Lattice Matching between the Shell and the Embedding Matrix. *Chemistry of Materials* **2017,** *29* (12), 5200-5206.

14.   Song, Q., Size and Shape Controlled Synthesis and Superparamagnetic Properties of Spinel Ferrites Nanocrystals. **2005**.

15.   Lenaic lartigue, P. H., Damien Alloyeau, Sarah P. Clarke, Michael Levy, Jean-Claude Bacri, Rana Bazzi, Dermot F. Brougham, Claire Wihelm, and Florence Gazeau, Cooperative Organization in Iron Oxide Multi-Core Nanoparticles Potentiates Their Efficiency as Heating Mediators and MRI Contrast Agents. *ACS Nano* **2012,** *6* (12), 10935-10949.

16.   Masala, O.; Hoffman, D.; Sundaram, N.; Page, K.; Proffen, T.; Lawes, G.; Seshadri, R., Preparation of magnetic spinel ferrite core/shell nanoparticles: Soft ferrites on hard ferrites and vice versa. *Solid State Sciences* **2006,** *8* (9), 1015-1022.

17.   Han, M. H., Development of Synthesis Method for Spinel Ferrite Magnetic Nanoparticle and Its Superparamagnetic Properties. **2008**.

18.   Sabo, D. E., Novel Synthesis of Metal Oxide Nanoparticles via the Aminolytic Method and the Investigation of Their Magnetic Properties. **2012**, 158.

19.   Chen, H. W., Aminolytic Synthesis and Ferromagnetic Resonance of Cobalt and Manganese Based Spinel Ferrite Nanoparticles. **2018**, 148.

20.   Mattei, J.-L.; Le Guen, E.; Chevalier, A.; Tarot, A.-C., Experimental determination of magnetocrystalline anisotropy constants and saturation magnetostriction constants of NiZn and NiZnCo ferrites intended to be used for antennas miniaturization. *J Magn Magn Mat.* **2015,** *374*, 762-768.

21.   Harris, V. G., Modern Microwave Ferrites. *IEEE Trans Magn.* **2012,** *48* (3), 1075-1104.

22.   Rondinone, A. J.; Liu, C.; Zhang, Z. J., Determination of Magnetic Anisotropy Distribution and Anisotropy Constant of Manganese Spinel Ferrite Nanoparticles. *J Phys Chem B.* **2001,** *105* (33), 7967-7971.

CHAPTER 5: DISORDERED SURFACE STATES OF ANTIFERROMAGNETIC (NIO, COO, AND NI$_5$CO$_5$O) NANOPARTICLES CONTRIBUTES TO EXCHANGE BIAS AND SUPERPARAMAGNETISM

5.1 Introduction

The novel synthesis of magnetic nanoparticles has generated increased interest due to their unique magnetic properties and the expanding demands of their technological applications. Research in antiferromagnetic (AFM) materials has increased over the past few decades since giant magnetoresistance (GMR) sensors revolutionized magnetic recording media in 1989.[1, 2]   Since the onset of GMR devices has also lead to the development of other spin-based electronics such as spin valves and magnetic tunneling junctions that furthering the need to understand the fundamental properties of antiferromagnetic nanomaterials as essential components in these growing technologies.[3] Antiferromagnetic nanoparticles have been known to exhibit ferromagnetic moments since the early work by Néel yet the origin of this atypical magnetism is still largely unexplained.[4] Néel predicted that fine particles of antiferromagnetic materials would exhibit similar magnetic phenomena to nanoscale ferromagnetic materials such as spin-glass states and superparamagnetism.[5, 6] Furthering the fundamental understanding in antiferromagnetic nanoparticle systems is further complicated by the variety of synthetic strategies that result in samples of varied quality.

Previous reports on AFM nanoparticles have attributed the anomalous magnetic properties to either stoichiometric defects in the crystal lattice resulting in charge imbalance or the presence of ferromagnetic metallic impurities.[4, 7, 8] Most commonly CoO and NiO nanocrystals have shown ferromagnetic moments and superparamagnetism that is typically explained as the result of crystal defects unbalancing the net charge or from ferromagnetic metallic atom cluster impurities.[9-12] Kodama et al. reported the observation of exchange bias in NiO nanocrystals diameter 5-80 nm and theorized this behavior arises from uncompensated surface spins as a result of finite size effects.[13] The uncompensated surface spins found in nanoscale antiferromagnets materials such as NiO and CoO can form a spin-glass surface state that can contribute to the net magnetic moment of the particle causing superparamagnetism and exchange coupling with the AFM core spins.[14-16]

In this report, we have synthesized and magnetically characterized NiO, CoO, and $Ni_{.5}Co_{.5}O$ nanoparticles 5-7 nm in diameter observing superparamagnetism with blocking temperatures well below their respective bulk Néel temperatures, large coercivities, and exchange bias. We report evidence of core/shell heterostructure in antiferromagnetic nanoparticles that consists of an antiferromagnetically ordered core surrounded by a shell of uncompensated surface spins that contributes to these anomalous magnetic properties. In this study, we investigated the unique phenomenon of exchange bias originating from the exchange-coupling of interfacial antiferromagnetic core spins and uncompensated spins of the disordered surface layer. These magnetic properties are increasingly more relevant with the increased study of AFM materials as nonvolatile components of exchange bias systems in microelectronics and magnetic media recording.

5.2 Experimental

5.2.1   Synthesis of Antiferromagnetic nanocrystals

The modified aminolytic synthesis method outlined in **Chapter 2** was utilized in the synthesis of all antiferromagnetic nanocrystals. To prepare 5 nm NiO nanocrystals, 12 mmol of metal acetate precursor, 20 mL of oleylamine, and 60 mL of dibenzyl ether to a 3-neck round bottom flask. The reaction mixture is stirred and refluxed at 140°C for 1 hour. After 1 hour of mixing, begin to flow O_2 gas into the reaction vessel and reflux at 220°C for 1 hour. The reaction is cooled and collected via centrifuge and washed with ethanol to remove excess organics from the synthesized nanocrystals, this step was repeated 4 times. This procedure can be utilized to synthesize NiO, CoO, and mixed composition $Ni_{1-x}Co_xO$ nanocrystals.

5.2.2   Characterization

Sample crystallinity and phase purity was measured with powder x-ray diffraction on a Bruker D8 Advance diffractometer. *Transmission electron microscopy (TEM) studies were performed using JEOL 100C operating at 100 kV.* A superconducting quantum inference device (SQUID) magnetometer (Quantum Design MPMS-5S) with an applied magnetic field up to 5 T at temperature range of 2-400 K was used to perform both temperature and magnetic field dependent magnetization measurements. The temperature range was measured from 5 to 315 K. Field-dependent magnetic measurements were prepared by dispersing the dry nanocrystal powder in eicosane (Aldrich, 99%) to stabilize and eliminate interparticle interaction effects.

5.3 Results and Discussion

The as-synthesized nanoparticles were characterized by X-ray diffraction (XRD). The as-synthesized NiO, $Ni_{.5}Co_{.5}O$, and CoO nanoparticles show typical diffraction peaks of face-centered cubic (FCC) rock salt crystal structure without impurities (**Figure 5-1**). The crystallite size was estimated with the Scherrer's formula to be respectively for the various compositions (**Equation 5**).[17]

$$d = \frac{K\lambda}{Bcos(\theta)} \tag{9}$$

Temperature-dependent magnetic susceptibility measurements were performed under an external field of 500 Oe. **Figure 5-2** shows that all samples demonstrate superparamagnetic behavior well below the respective Néel temperatures (T_N) of these
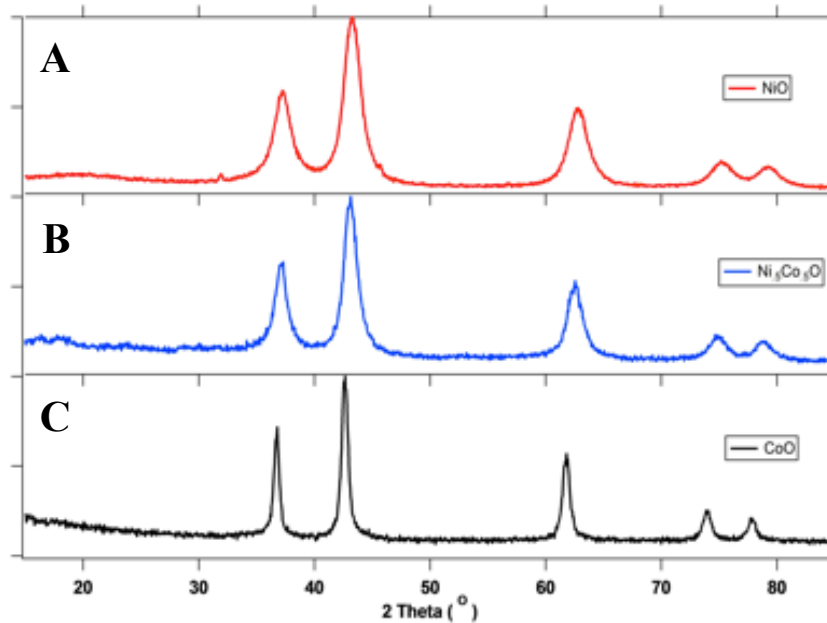
Figure 5-1: XRD pattern of core nanocrystals (A) NiO, (B) $Ni_{.5}Co_{.5}O$, and (C) CoO nanocrystals.
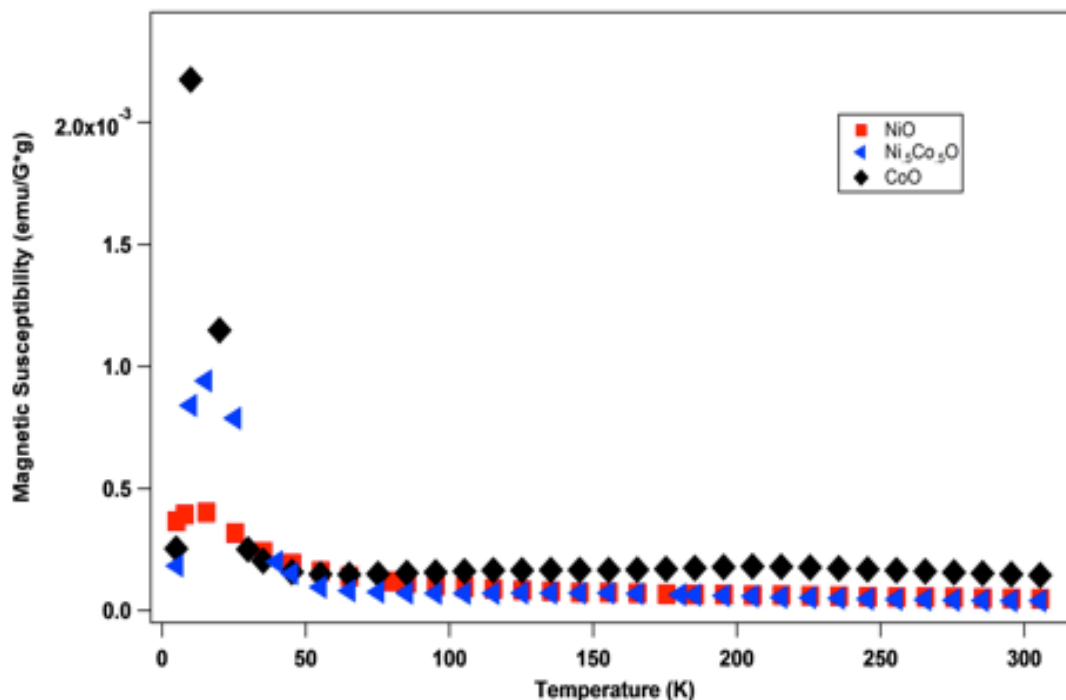
Figure 5-2: Temperature dependent magnetic susceptibility measurement of NiO, Ni$_5$Co$_5$O, and CoO nanoparticles measured from 5 to 305 K under 100 Oe applied field

materials. CoO (7.0 nm) nanoparticles have T$_B$ at 10 K below bulk T$_N$ of 293 K. NiO (5.4 nm) nanoparticles also exhibit a similar trend with their T$_B$ = 15 K well below NiO bulk T$_N$ = 525 K. The superparamagnetic behavior of NiO and CoO nanoparticles is indicative of uncompensated surface spins aligning with the applied field at low temperatures. The uncompensated surface spins contribute considerably in nanoscale AFM due to finite size effects; this disordered surface has a low barrier for thermal activation resulting in the

transition to a superparamagnetic state at low temperatures zero field-cooled and field-cooled field-dependent magnetization measurements were performed on all samples at 5 K field ranging from 5 to -5 T as shown in **Figures 5-3,4,5**. These results show unexpectedly large coercivity (H_C) values for all samples with Ni$_5$Co$_5$O having exceptionally large H_C of 7000 Oe, NiO having H$_C$ = 2000 Oe, and CoO having the smallest
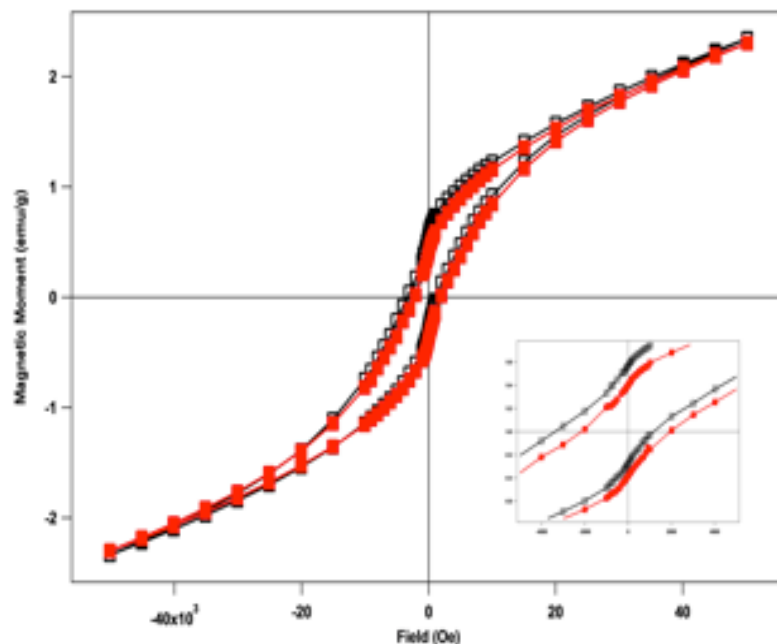
Figure 5-3: Zero-field cooled and field-cooled field dependent magnetic hysteresis measurement of NiO nanoparticles measured at 5 K with applied fields ranging from ± 5 Telsa, field-cooled from 305 K under field applied field of 1T
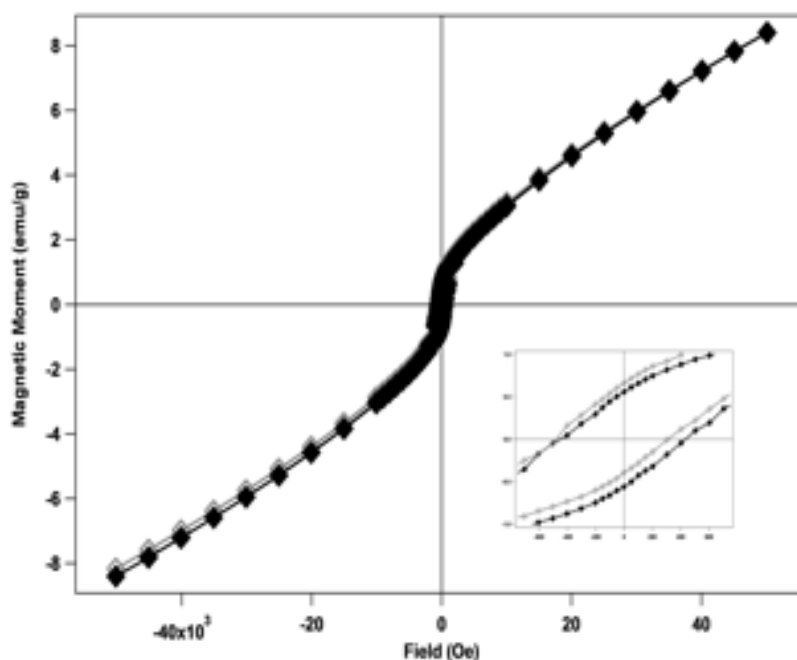
Figure 5-4: Zero-field cooled and field-cooled field dependent magnetic hysteresis measurement of CoO nanoparticles measured at 5 K with applied fields ranging from ± 5 Telsa, field-cooled from 305 K under field applied field of 1T
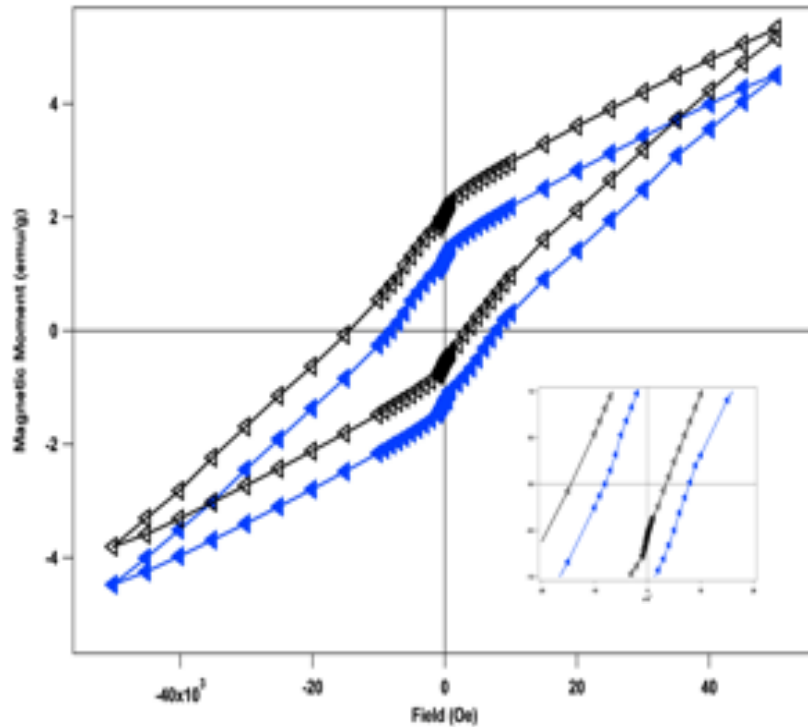
Figure 5-5: Zero-field cooled and field-cooled field dependent magnetic hysteresis measurement of Ni.5Co.5O nanoparticles measured at 5 K with applied fields ranging from ± 5 Telsa, field-cooled from 305 K under field applied field of 1T

H_C = 400 Oe. The large coercivity of Ni.5Co.5O nanocrystals can be attributed to increased surface disorder from the lattice mismatch between the NiO/CoO components. The larger contribution from uncompensated spins is also reflected in elevated T_B = 15 K and larger saturation M_S = 4.5 emu/G•g and remanent M_r = 1.3 emu/G•g magnetizations than either NiO or CoO samples. The CoO nanocrystals are more structurally ordered than the other samples evidenced by the lower magnetic moment observed in temperature dependent measurements and the relatively small coercivity observed here.

Exchange bias shifts are the product of interfacial exchange coupling between hard antiferromagnetic and soft ferromagnetic materials, upon field-cooling through the T_N of

the AFM phase the AFM spins will pin the FM spins altering the magnetic reversal mechanism resulting in a hysteresis loop shift. All samples exhibit some degree of exchange bias primarily as vertical magnetization shifts instead of field shifts further evidence of exchange coupling between two spin sublattices. The $Ni_{.5}Co_{.5}O$ nanocrystal demonstrates the largest exchange bias field shift of 8000 Oe which is consistent with it possessing more uncompensated spins in the shell due to structural disorder. In addition to the typical field shift observed in exchange biased systems a vertical magnetization shifts but the origin has been largely unknown. The vertical magnetization shift is the product of the uncompensated surface spins in AFM nanocrystals. These surface spins align with the applied magnetic field upon field-cooling and become exchange biased below the blocking temperature of the AFM nanocrystals.[13] The exchange biased surface spins increase the remanent magnetization in the field-cooled M-H curves, the vertical magnetization shift increases the effective exchange bias field shift of the sample. This phenomenon is most notable in the $Ni_{.5}Co_{.5}O$ sample which has more uncompensated spins in the disordered surface state than the NiO or CoO nanocrystals. The vertical magnetization shift can only be observed in AFM nanomaterials with uncompensated surface spins.

Table 5-1: Magnetic and Exchange Bias properties of NiO, $Ni_{.5}Co_{.5}O$, and CoO nanocrystals

Sample	Crystallite Size (nm)	T_B (K)	H_C (Oe)	ZFC M_R (emu/G•g)	H_E (Oe)	FC M_R (emu/G•g)
NiO	5.4	15	2000	0.40	1360	0.57
Ni_5Co_5O	7.2	15	8000	1.30	7000	2.10
CoO	7.3	10	450	0.56	30	0.70

5.4 Conclusions

In summary, we report a novel synthesis method for nanoscale NiO, CoO, and Ni$_5$Co$_5$O nanocrystals that exhibit superparamagnetism and unique exchange bias. Finite size effects result in the presence of large coercivities and vertical magnetization shifts can be explained by the presence of uncompensated spins on the surface of the AFM nanoparticles and not to metallic contaminates. Under field-cooled conditions these spins align with the applied magnetic field causing a net increase in magnetic moment (vertical shift), these surface spins become pinned via exchange bias interactions with the antiferromagnetically ordered core of the nanoparticle resulting in shifted hysteresis loop. The large coercivity values observed for these AFM nanoparticles can also be attributed to this exchange bias interaction between the AFM core and uncompensated surface spins as these spins produce the available spins for magnetic moment. This exchange bias interaction at the surface is very weak but can be observed in nanoscale particles such as those in this study and is emphasized more in disordered structured nanoparticles such as mixed solid solution Ni$_5$Co$_5$O nanocrystals. The existence of the uncompensated surface spins and exchange bias in nanoscale antiferromagnetic nanoparticles has implications for the advanced design of exchange biased nanomaterial systems such as GMR and spintronics applications.

5.5 REFERENCES

1. Baibich, M. N.; Broto, J. M.; Fert, A.; Nguyen Van Dau, F.; Petroff, F.; Etienne, P.; Creuzet, G.; Friederich, A.; Chazelas, J., Giant magnetoresistance of (001)Fe/(001)Cr magnetic superlattices. *Phys Rev Lett* **1988,** *61* (21), 2472-2475.

2. Binasch, G.; Grunberg, P.; Saurenbach, F.; Zinn, W., Enhanced magnetoresistance in layered magnetic structures with antiferromagnetic interlayer exchange. *Phys Rev B Condens Matter* **1989,** *39* (7), 4828-4830.

3. Jungwirth, T.; Marti, X.; Wadley, P.; Wunderlich, J., Antiferromagnetic spintronics. *Nat Nanotechnol* **2016,** *11* (3), 231-41.

4. Tiwari, S. D.; Rajeev, K. P., Effect of distributed particle magnetic moments on the magnetization of NiO nanoparticles. *Solid State Communications* **2012,** *152* (12), 1080-1083.

5. Bedanta, S.; Kleemann, W., Supermagnetism. *J Phys D: Appl Phys.* **2009,** *42*, 1-28.

6. Tannous, C.; Gieraltowski, J., The Stoner–Wohlfarth model of ferromagnetism. *Euro J Phys.* **2008,** *29* (3), 475-487.

7. Shim, H.; Dutta, P.; Seehra, M. S.; Bonevich, J., Size dependence of the blocking temperatures and electron magnetic resonance spectra in NiO nanoparticles. *Solid State Communications* **2008,** *145* (4), 192-196.

8.   Roca, A. G.; Golosovsky, I. V.; Winkler, E.; Lopez-Ortega, A.; Estrader, M.; Zysler, R. D.; Baro, M. D.; Nogues, J., Unravelling the Elusive Antiferromagnetic Order in Wurtzite and Zinc Blende CoO Polymorph Nanoparticles. *Small* **2018,** *14* (15), e1703963.

9.   Ghosh, M.; Sampathkumaran, E. V.; Rao, C. N. R., Synthesis and Magnetic Properties of CoO Nanoparticles. *Chem Mat.* **2005,** *17* (9), 2348-2352.

10.   Tadic, M.; Nikolic, D.; Panjan, M.; Blake, G. R., Magnetic properties of NiO (nickel oxide) nanoparticles: Blocking temperature and Neel temperature. *J Alloys Compd.* **2015,** *647*, 1061-1068.

11.   Ichiyanagi, Y., Magnetic properties of NiO nanoparticles. *Physica B: Condensed Matter* **2003,** *329-333*, 862-863.

12.   Richardson, J. T.; Yiagas, D. I.; Turk, B.; Forster, K.; Twigg, M. V., Origin of superparamagnetism in nickel oxide. *J Appl Phys.* **1991,** *70* (11), 6977-6982.

13.   R.H. Kodama, S. A. M., and A.E. Berkowitz, Finite Size Effects in Antiferromagnetic NiO Nanoparticles. *Phys Rev Let.* **1997,** *79* (7), 1393-1396.

14.   Tadic, M.; Panjan, M.; Markovic, D.; Stanojevic, B.; Jovanovic, D.; Milosevic, I.; Spasojevic, V., NiO core–shell nanostructure with ferromagnetic-like behavior at room temperature. *J Alloys Compd.* **2014,** *586*, S322-S325.

15.   Tiwari, S. D.; Rajeev, K. P., Signatures of spin-glass freezing in NiO nanoparticles. *Phys Rev B.* **2005,** *72* (10).

16.   Proenca, M. P.; Sousa, C. T.; Pereira, A. M.; Tavares, P. B.; Ventura, J.; Vazquez, M.; Araujo, J. P., Size and surface effects on the magnetic properties of NiO nanoparticles. *Phys Chem Chem Phys.* **2011,** *13* (20), 9561-7.

17.   Cullity, B. D., Stock, S.R., Elements of X-Ray Diffraction, Third Edition. *Pearson.* **2001**, 696.

CHAPTER 6: TUNING EXCHANGE BIAS PROPERTIES OF BIMAGNETIC CORE-SHELL NANOPARTICLES

6.1 Introduction

Bimagnetic core-shell nanocrystals provide a design strategy to study fundamental science and achieve relevant magnetic properties for technological applications.[1] The core-shell architecture enables exchange coupling between complex core-shell combinations that expands nanomagnetism design beyond size, morphology, and chemical composition.[2] Exchange-coupled core-shell nanoparticles have been shown to improve the energy product of rare-earth free permanent magnets and also beat "superparamagnetic limitations" by increasing the thermal stability of magnetic nanoparticles.[3]

The further exploration of various core-shell combinations in nanoparticulate systems resulted in the discovery by Bean and Meklekoff of a new exchange coupling interaction between the ferromagnetic cobalt core and the antiferromagnetic CoO shell of core-shell
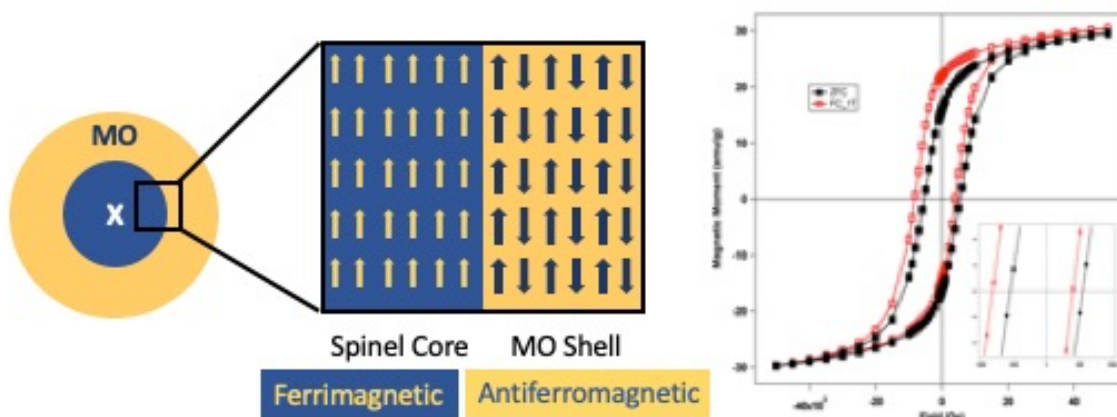

Figure 6-1: Core@shell architecture nanoparticle design to study exchange bias in bimagnetic ferrimagnetic-antiferromagnetic exchange bias systems.

Co@CoO nanoparticles.[4, 5]   The exchange coupling interaction between ferromagnetic (FM) and antiferromagnetic (AFM) bilayered materials is known as exchange bias and manifests as a field shift of the magnetic hysteresis loop under field-cooled measurements, enhancement of the coercivity, and increased thermal stability.[4-8]   Microelectronic devices require extensive electromagnetic shielding to protect volatile components from stray magnetic fields: exchange-coupled components with antiferromagnetic materials improves the stability of these delicate components without excess shielding.[9]   Thin film devices consisting of exchange-coupled magnetic bilayers have become the backbone of many technological applications since Kope revolutionized magnetic recording media with the discovery of giant magnetoresistance (GMR) in 1989.[10]   An essential component of GMR device is the "pinned" magnetic spins of ferromagnetic/antiferromagnetic bilayer in which exchange coupling of spins at the FM/AFM interface restricts magnetic relaxation mechanism of the system.[10, 11]   Magnetic multilayered films are the building block for advancing electronics and computer technology through research in spintronics and other exchange bias devices.[12, 13]

Despite the initial discovery of exchange bias in core-shell nanocrystals the vast majority of research has been restricted to bilayered thin films due to synthetic obstacles to complex core-shell nanoparticles.[4, 9, 14, 15]   Those fundamental studies of exchange bias in nanoparticulate systems have been dominated by partially oxidized metal nanoparticles limiting FM-AFM combinations such as studies of Co@CoO, Ni@NiO, and Fe_2O_3@Fe_3O_4 nanocrystals.[5, 16-20]   The development of seed-mediated synthetic methods has broadened the scope of material compositions and combinations available to be studied in core-shell architectures.[21]   Inverted AFM-FM core-shell architectures have been heavily investigated

with antiferromagnetic nanocrystals serving as the scaffold for complex exchange biased systems.[22-24] Recently, Lavorato et al. have investigated inverted $CoO@Co_xZn_{1-x}Fe_2O_4$ AFM@FM nanoparticles demonstrating exchange bias properties dependent on available FM spins for interfacial coupling.[25] These inverted AFM@FM systems allow for more flexible chemical compositions/variety of ferromagnetic materials for exchange-biased composites.

Herein, we report a novel seed-mediated synthetic method for bimagnetic core-shell nanocrystals of ferrimagnetic@antiferromagnetic architecture. We have previously utilized this method to synthesize size controlled $Ni_{1-x}M_xFe_2O_4$ (M = Co^{2+}, Zn^{2+}, and Fe^{2+}) nanocrystals and antiferromagnetic monoxide (NiO, CoO, and $Ni_xCo_{1-x}O$) nanoparticles (**Chapters II-V**). Utilizing this seed-mediated synthesis technique we investigate $NiFe_2O_4@CoO$ core-shell nanoparticles with variable core size, shell thickness, and variable chemical compositions of both the FM core and AFM shell. The results demonstrate that exchange bias properties are dependent on the anisotropy energies of the FM and AFM phases. The anisotropy energies of both FM/AFM phases can be tuned through the synthetic control of surface area to volume ratio of the FM core and through selection of core-shell material combinations. Bimagnetic FM@AFM nanoparticles produce strong exchange bias properties are strong candidates for nanoscale magnetic recording media and spintronic applications.

6.2 Experimental

6.2.1 Synthesis of Spinel Ferrite core nanocrystals

To prepare 5 nm $Ni_xM_{1-x}Fe_2O_4$ nanocrystals, 12 mmol of mixed metal acetate precursor, 20 mL of oleylamine, and 60 mL of dibenzyl ether to a 3-neck round bottom flask. The reaction mixture is stirred and refluxed at 140°C for 1 hour. After 1 hour of mixing a flow of O_2 gas to the reaction vessel and refluxed at 220°C for 1 hour. The reaction is cooled and collected via centrifuge and washed with ethanol to remove excess organics from the synthesized nanocrystals.

6.2.2 Seed-Mediated Synthesis of core@shell nanoparticles

To prepare core/shell $NiFe_2O_4$@MO nanoparticles, 500 mg of $NiFe_2O_4$ core nanoparticles, 12 mmol of metal acetate precursor, 20 mL of oleylamine, and 60 mL of dibenzyl ether to a 3-neck round bottom flask. Repeat the synthetic procedure for the core nanoparticles.

6.2.3 Characterization

Sample crystallinity and phase purity was measured with powder x-ray diffraction on a Bruker D8 Advance diffractometer. *Transmission electron microscopy (TEM) studies were performed using JEOL 100C operating at 100 kV.* A superconducting quantum inference device (SQUID) magnetometer (Quantum Design MPMS-5S) with an applied magnetic field up to 5 T at temperature range of 2-400 K was used to perform both temperature and magnetic field dependent magnetization measurements. The temperature range was measured from 5 to 315 K. Field-dependent magnetic measurements were

prepared by dispersing the dry nanocrystal powder in eicosane (Aldrich, 99%) to stabilize and eliminate interparticle interaction effects.

6.3 Results and Discussion

Monodispersed core-shell nanoparticles of ferrimagnetic core ($Ni_{1-x}Co_xFe_2O_4$) with an antiferromagnetic shell ($Ni_{1-x}Co_xO$) were synthesized by modified aminolytic method coupled with seed-mediate growth. The size of the spinel ferrite cores were controlled from 4.4 to 10.0 nm in diameter while the antiferromagnetic shells were grown from 0.5 to 2.0 nm in thickness. **Figure 6-2** shows the powder X-ray diffraction patterns with characteristic peaks for 5.5 nm native $NiFe_2O_4$ nanoparticles, CoO phase, and core@shell
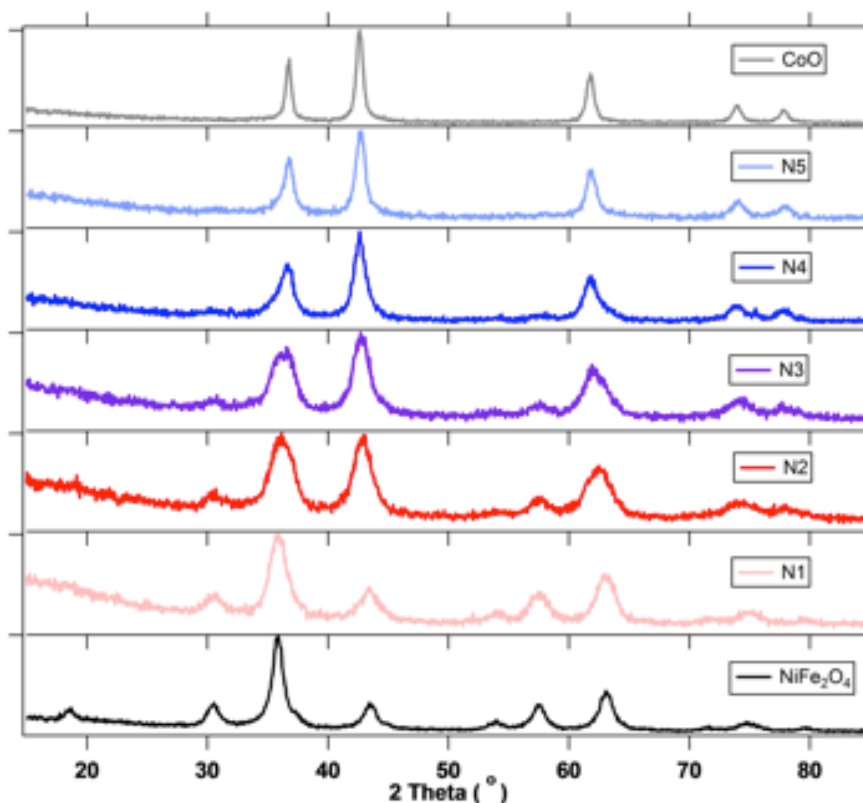
Figure 6-2: Powder XRD patterns of NiFe₂O₄, NiFe₂O₄@CoO (N1-N5), and CoO nanoparticles

NiFe$_2$O$_4$@CoO with variable CoO shell thickness (N1-N5). The XRD patterns for core-shell nanocrystals both reflection patterns for the core NiFe$_2$O$_4$ and shell CoO materials and samples with thicker CoO shells show higher intensity CoO reflection peaks. The expected bulk reflection patterns of NiFe$_2$O$_4$ (COD-1011032) and CoO (COD-9008618). The average crystallite size for the core NiFe$_2$O$_4$ nanocrystals was calculated by using the Scherrer formula.

The temperature dependence of magnetic susceptibility measurements of magnetic properties of NiFe$_2$O$_4$@CoO of variable core-shell dimensions are shown in **Figures 6-3, 6-4**. The volume of the antiferromagnetic phase was also investigated for correlations with the blocking temperature of NiFe$_2$O$_4$@CoO nanoparticles by maintaining the same core size of 5.5 nm and varying the CoO shell thickness from 0.5 to 2.0 nm. **Figure 6-3** shows
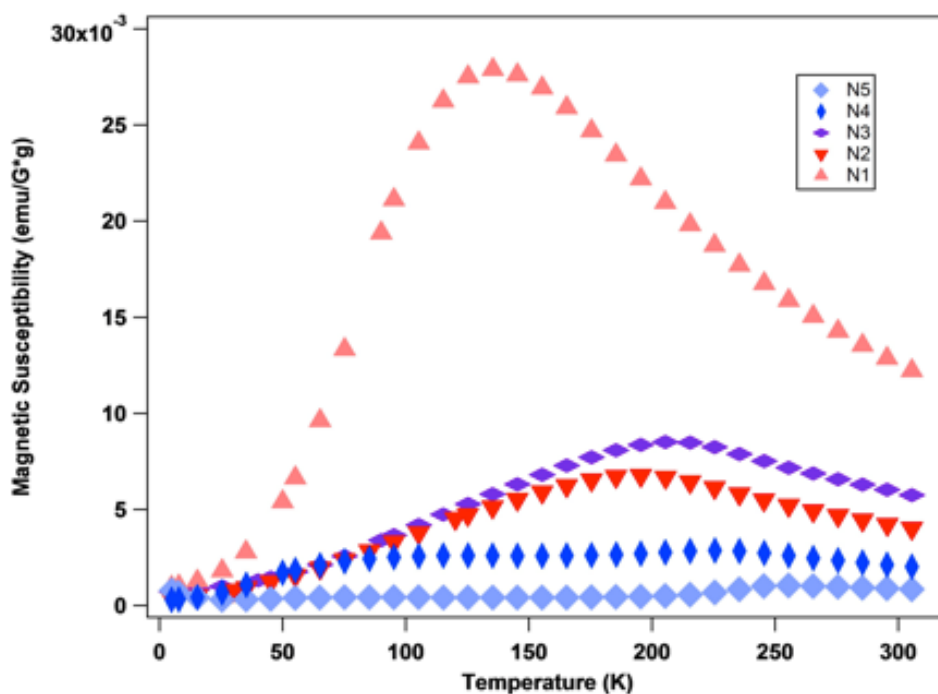
Figure 6-3: Temperature dependent magnetic susceptibility measurement of NiFe$_2$O$_4$@CoO nanoparticles with increasing CoO shell thickness N5>N1 measured from 5 to 305 K under 100 Oe applied field

temperature dependent magnetization under 100 Oe applied magnetic field for the NiFe$_2$O$_4$@CoO of variable shell thickness. The blocking temperature increases with increased CoO shell thickness, but the magnetic susceptibility is greatly reduced. The correlation between the size of the NiFe$_2$O$_4$ core with the blocking temperature of NiFe$_2$O$_4$@CoO nanoparticles was investigated by synthesizing NiFe$_2$O$_4$ seeds of varying sizes from 4.4 to 10.0 nm in diameter and then growing 1.0 nm CoO shells. **Figure 6-4** shows the temperature dependence of magnetization under 100 Oe applied magnetic field for the NiFe$_2$O$_4$@CoO. The blocking temperature of variable core size NiFe$_2$O$_4$@CoO system increases with increased core NiFe$_2$O$_4$ size approaching T$_B$ of 245 K for 10.0 nm core.
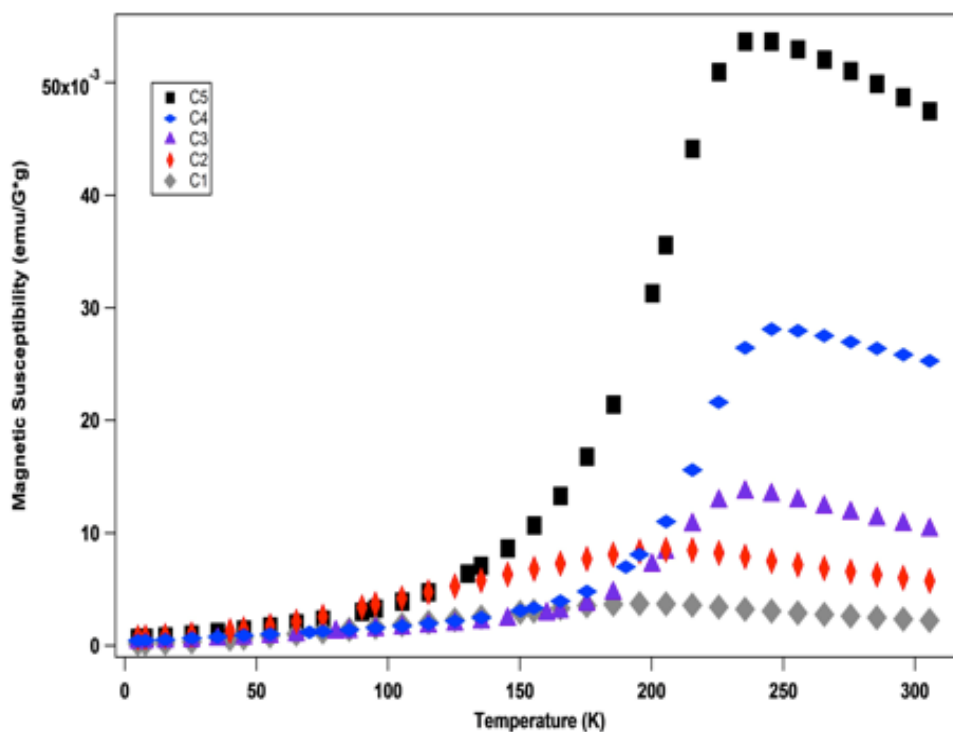
Figure 6-4: **Temperature dependent magnetic susceptibility measurement of NiFe$_2$O$_4$@CoO nanoparticles (4.4 to 9.6 nm cores) measured from 5 to 305 K under 100 Oe applied field**
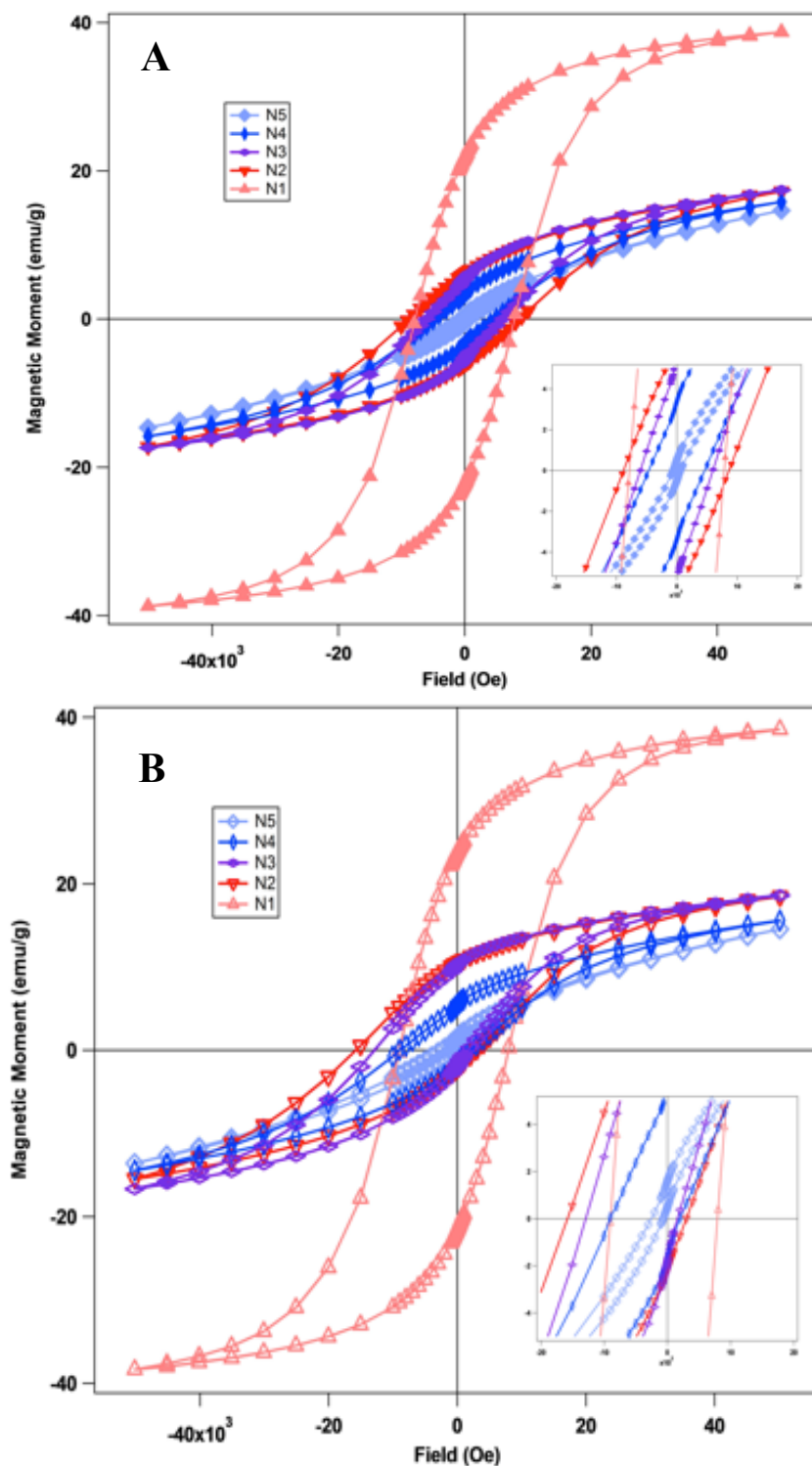
Figure 6-5: (A) Zero-field cooled and (B) field-cooled field dependent magnetic hysteresis measurement of NiFe$_2$O$_4$@CoO nanoparticles with a 5.4 nm NiFe$_2$O$_4$ core and increasing CoO shell thickness (<0.5 to 6.3 nm) measured at 5 K with applied fields ranging from $\pm$ 5 Telsa, field-cooled from 305 K under field applied field of 1T
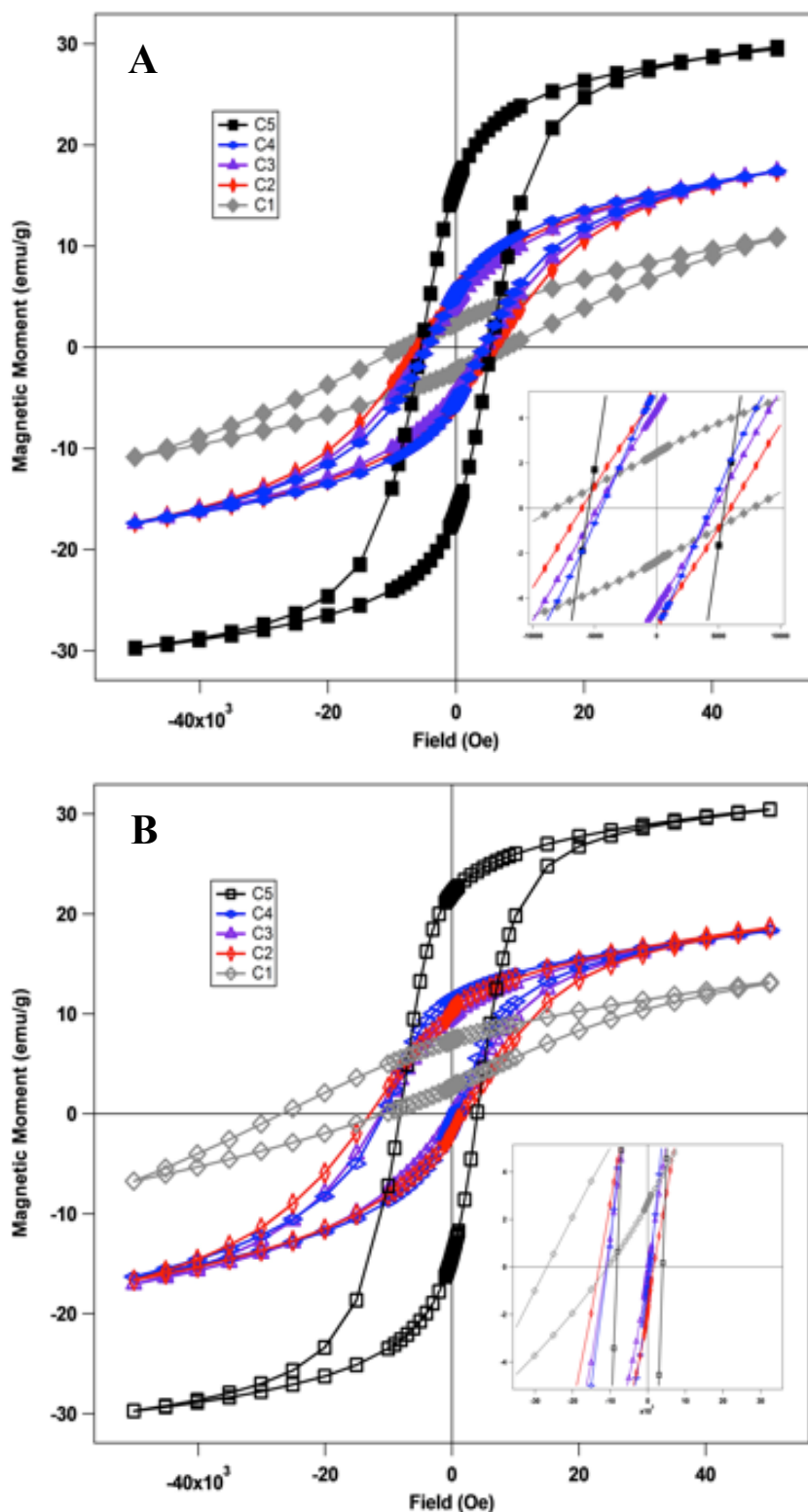
Figure 6-6: **(A) Zero-field cooled and (B) field-cooled field dependent magnetic hysteresis measurement of NiFe₂O₄@CoO nanoparticles with cores 4.4 to 10.0 nm in diameter measured at 5 K with applied fields ranging from ± 5 Telsa, field-cooled from 305 K under field applied field of 1T**

Table 6-1: Magnetic properties of NiFe$_2$O$_4$@CoO with variable CoO shell thickness (N1-N5).

Sample	Shell (nm)	T$_B$ (K)	H$_C$ (Oe)	H$_E$ (Oe)
N1	<0.5	135	7800	1200
N2	<0.5	190	8700	7300
N3	0.5	205	6000	7000
N4	2.2	225	4600	4400
N5	6.3	255	600	1900

The magnetic field dependence of magnetization of NiFe$_2$O$_4$@CoO of variable core-shell dimensions are shown in **Figure 6-5A,B and Figure 6-6A,B**. The introduction of a CoO shell can enhance the coercivity of native NiFe$_2$O$_4$ nanoparticles by close to 30-fold from 0.3 KOe to 9.4 KOe (**Table 6-1**). The coercivity of the core-shell nanoparticulate system decreases with increased core diameter (**Figure 6-6A**). The sample with the largest
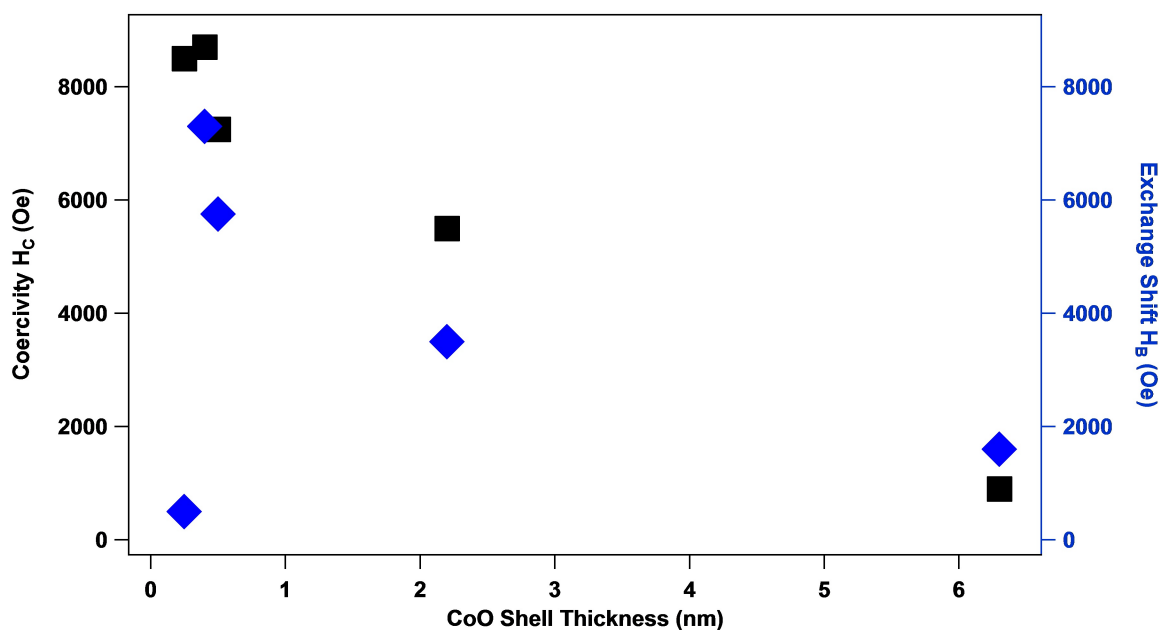
Figure 6-7: Coercivity (left axis) and exchange bias (right axis) as function of the CoO shell thickness (nm).

Table 6-2: Magnetic properties of NiFe₂O₄@CoO with variable NiFe₂O₄ core diameter (C1-C5).

Sample	Core Size (nm)	T_B Core (K)	T_B (K)	H_C (Oe)	H_E (Oe)
C1	4.4	25	195	8100	18650
C2	5.5	35	205	6000	7000
C3	7.0	55	235	4750	6500
C4	8.2	70	245	4450	6250
C5	9.6	85	240	5470	2680

surface area to volume ratio (4.4 nm diameter core) has the largest enhance coercivity, H_C = 9.4 KOe. In **Figure 6-5A** we observed that increasing the CoO shell thickness initially increases the coercivity of the core-shell system but increasing the thickness of the AFM shell reduces coercivity, saturation, and remanent magnetizations of the NiFe₂O₄@CoO system (**Table 6-1**). Exchange bias field shifts is reduced in samples with CoO shells beyond 1.0 nm in thickness, following a similar trend in behavior coercivity (**Figure 6-7**).
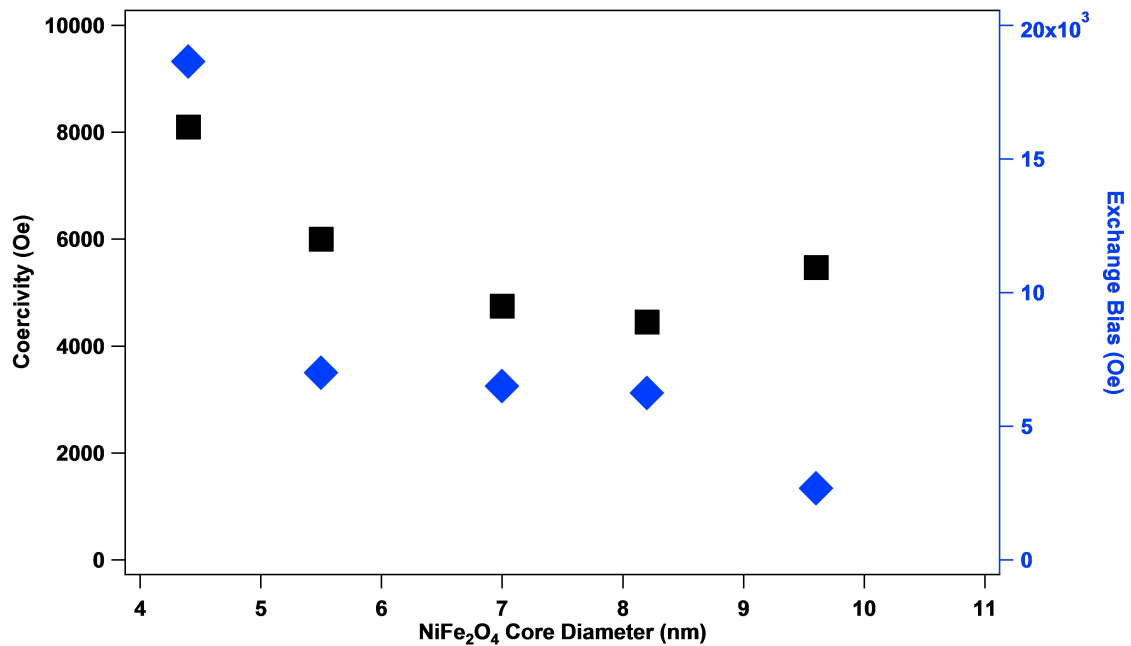

Figure 6-8: Coercivity (left axis) and exchange bias (right axis) as function of the NiFe₂O₄ core diameter (nm).

The field-cooled magnetic field dependence of magnetization cooled from 305 to 5 K under 1 Tesla applied magnetic field of $NiFe_2O_4@CoO$ nanoparticles (**Figures 6-5B, 6-6B**). All samples of $NiFe_2O_4@CoO$ exhibit exchange bias under field-cooled conditions, the magnitude of exchange bias correlates with reduced core diameter (**Figure 6-8**). The $NiFe_2O_4@CoO$ nanoparticle sample with a 4.4 nm diameter core exhibits the largest coercivity enhancement and exchange bias field shift of investigated samples (**Figure 6-14**).

The chemical composition of the core/shell materials were also varied to determine the contribution of the magnetocrystalline anisotropy constant of the interfaced materials on exchange bias. Core@shell nanocrystals of mixed shell composition $NiFe_2O_4@Ni_{1-x}Co_xO$ were characterized by powder x-ray diffraction (**Figure 6-9**). The chemical composition variation (x) is based on the Co molar concentration from ranging from 0 to 1. The temperature dependent magnetic susceptibility for $NiFe_2O_4@Ni_{1-x}Co_xO$ nanocrystals demonstrate an increase in thermal stability with increased molar concentration of cobalt in the antiferromagnetic shell phase (**Figure 6-10**). The introduction of a NiO shell suppresses the thermal stability of $NiFe_2O_4$ nanocrystal from $T_B = 45$ K to $T_B = 25$ K for $NiFe_2O_4@NiO$.

The temperature dependent and FC/ZFC magnetic field dependent magnetization for mixed solid solution $NiFe_2O_4@Ni_{1-x}Co_xO$ core-shell nanoparticles are shown in **Figure 6-11A,B**. **Figure 6-13A,B** shows the FC/ZFC magnetic field dependent magnetization of $CoFe_2O_4@CoO$ core-shell nanoparticles with core sizes of 4.4 and 6.0 nm in diameter.
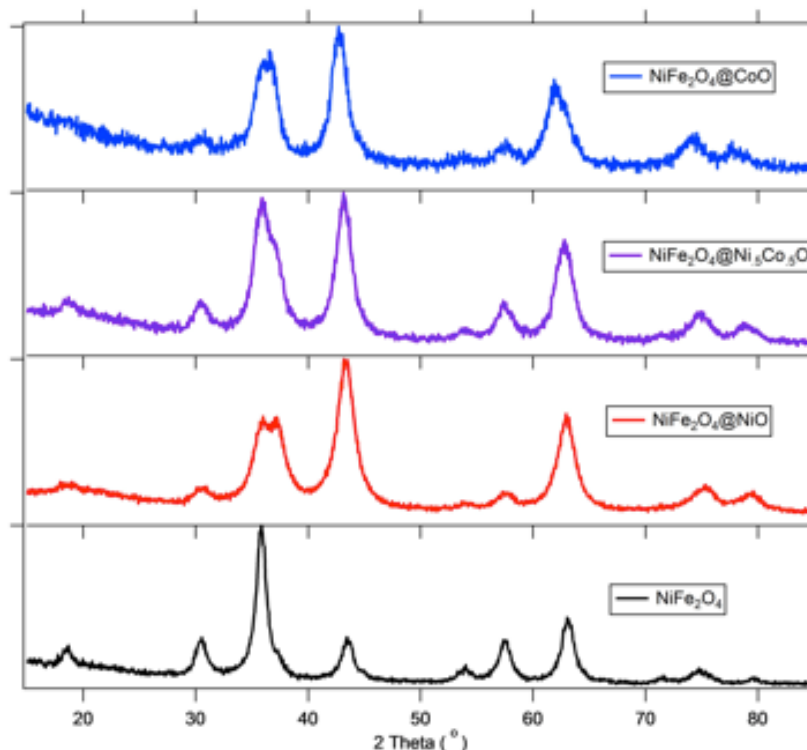
Figure 6-9: Powder XRD patterns of NiFe$_2$O$_4$, NiFe$_2$O$_4$@NiO, NiFe$_2$O$_4$@Ni$_{.5}$Co$_{.5}$O, and NiFe$_2$O$_4$@CoO nanoparticles

We carried out systematic studies on the magnetic properties of a series of ferrimagnetic-antiferromagnetic core-shell nanoparticulate systems, these studies include controlling various parameters of the core-shell system such as varying the size of the FM core, AFM shell thickness, and FM-AFM material combination through chemical composition of the FM core and AFM shell. To study the effects of dimensional parameters on exchange biased systems NiFe$_2$O$_4$@CoO nanoparticles will be investigated.   The chemical composition of both the spinel ferrite core and antiferromagnetic shell can be manipulated through the synthetic method, and this flexibility will enable the investigation of the magnetic properties of various combinations of core-shell magnetic materials. but we will focus on Ni$_{1-x}$Co$_x$Fe$_2$O$_4$ for the FM core and Ni$_{1-x}$Co$_x$O for the AFM shell.

All of the spinel ferrite core nanoparticles in all of the systems investigated follow the Stoner-Wohlfarth model for superparamagnetic nanocrystals with the blocking temperature (T_B) increasing with increased particle volume.[26] The Stoner-Wohlfarth model for single domain nanoparticles can be used to estimate the anisotropy energy of the ferrimagnetic cores from the blocking temperature:

$$E_A = KV\sin^2(\theta) = k_B T_B V \qquad (10)$$

Where K is the anisotropy constant, V is the volume of the ferrimagnetic nanoparticle, k_B is the boltzman constant, and T_B is the blocking temperature.[26] The introduction of an antiferromagnetic shell to superparamagnetic nanoparticles should increases the thermal stability of the system up to the bulk Néel temperature of the antiferromagnetic component of the system, $T_N = 293$ K for CoO and $T_N = 523$ K for NiO.[27, 28]

As shown in **Figure 6-10** NiO shells do not increase the thermal stability of the core-shell nanoparticles because of the low anisotropy energy of NiO. The substitution of strong L-S coupled Co^{2+} cations into the NiO crystal structure of the shell increases the anisotropy energy of the AFM phase raising the T_B. Exchange bias requires that the antiferromagnetic component to have larger anisotropy energy than the ferrimagnetic component for spin "pinning" to occur. This requirement anisotropy energy requirement can be expressed **Equation 7**:

$$K_{AFM}V_{AFM} > K_{FM}V_{FM} \qquad (7)$$

Where K is the anisotropy constant and V is the volume of the respective contributing antiferromagnetic or ferrimagnetic phase.[25] This equation establishes the minimal requirement for exchange bias in ferrimagnetic-antiferromagnetic material combinations.

The field-cooled magnetic hysteresis of $CoFe_2O_4@CoO$ does not exhibit typical exchange bias but instead has an asymmetrical hysteresis loop (**Figure 6-13A,B**). This phenomenon is the product of an exchange coupling interaction between the antiferromagnetic shell and the disordered surface state of the core-shell nanoparticle. As shown in antiferromagnetic nanocrystals the disordered surface state of an AFM phase can
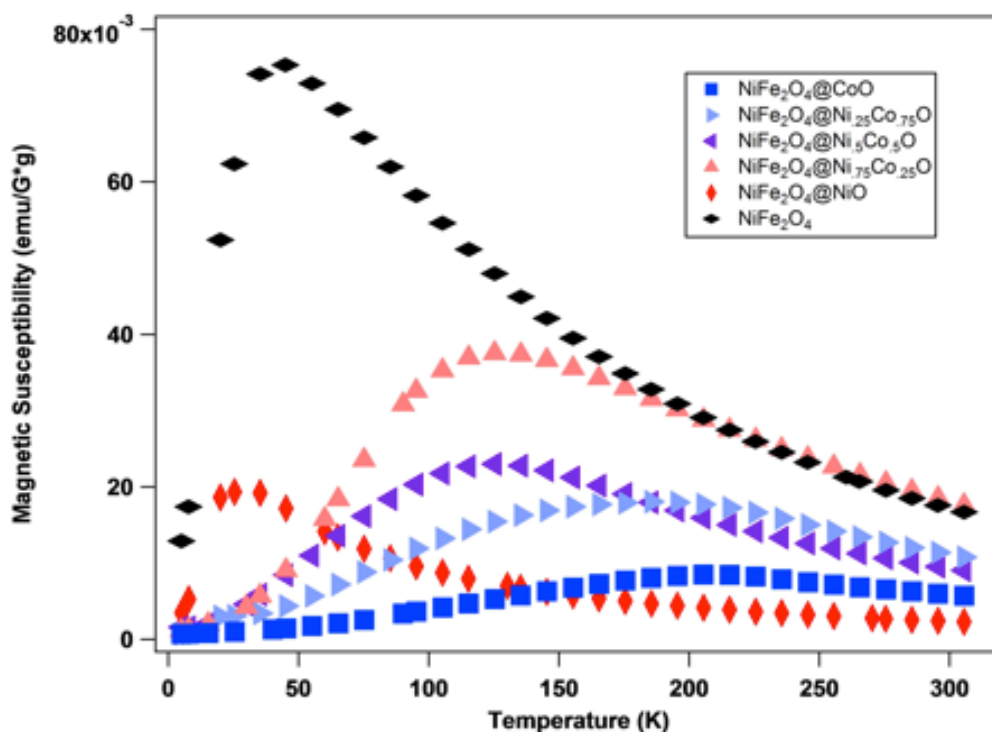
Figure 6-10: Temperature dependent magnetic susceptibility measurement of $NiFe_2O_4@Ni_{1-x}Co_XO$ nanoparticles measured from 5 to 305 K under 100 Oe applied field.
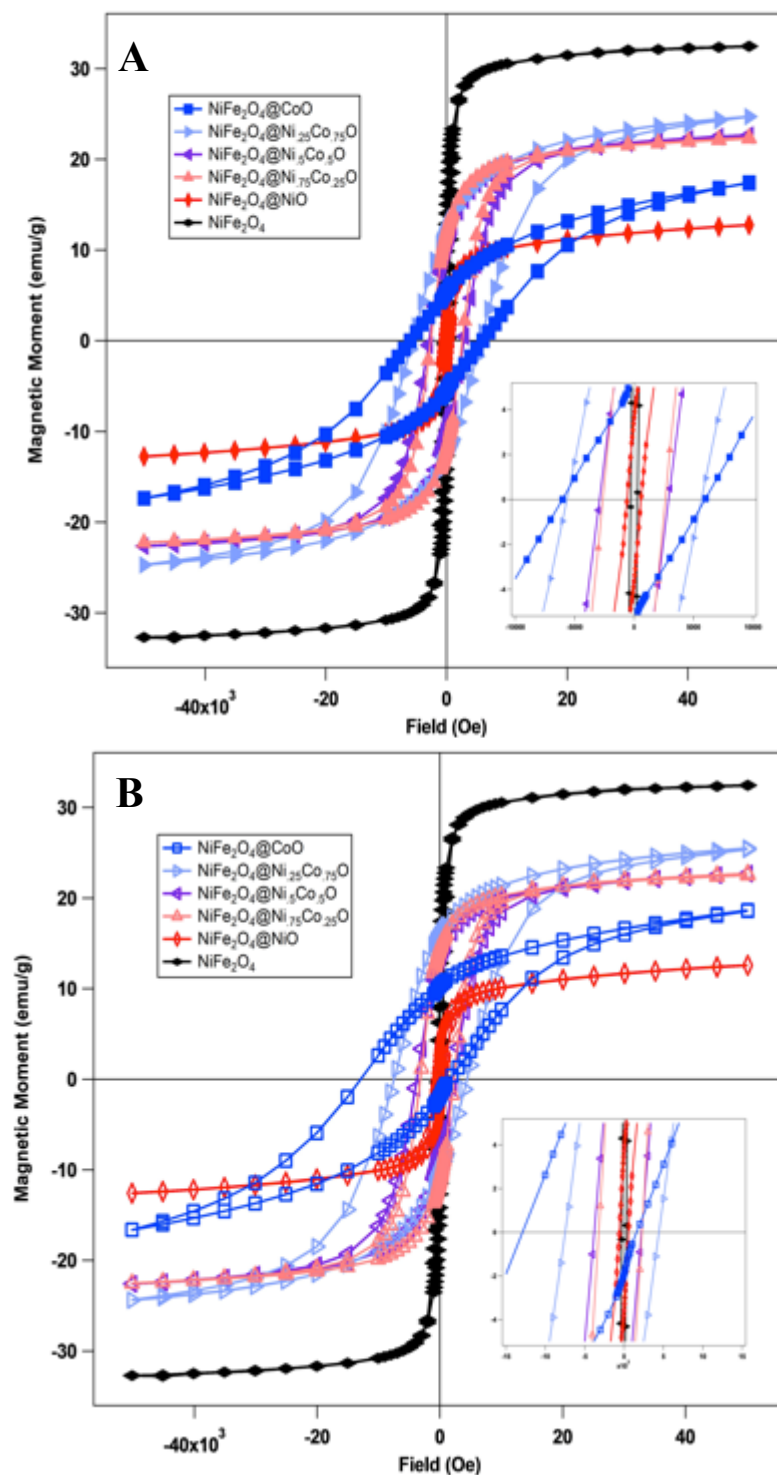
Figure 6-11 (A) Zero-field cooled and (B) field-cooled field dependent magnetic hysteresis measurement of variable shell composition NiFe₂O₄@Ni₁₋ₓCoₓO nanoparticles measured at 5 K with applied fields ranging from ± 5 Telsa, field-cooled from 305 K under field applied field of 1T

Table 6-3: Magnetic properties of NiFe$_2$O$_4$@Ni$_{1-x}$Co$_x$O nanocrystals.

Shell Composition	T$_N$ (K)	T$_B$ (K)	H$_C$ (Oe)	H$_E$ (Oe)
NiO	525	25	600	0
Ni$_{.75}$Co$_{.25}$O	N/A	125	2600	600
Ni$_{.5}$Co$_{.5}$O	N/A	125	3500	800
Ni$_{.25}$Co$_{.75}$O	N/A	185	5650	1800
CoO	293	205	6000	7000

be magnetized under field-cooled conditions and become exchange coupled with the AFM ordered sublattices. Exchange coupling at the AFM-surface interface results in a net increase of saturation and remanent magnetization as well as exchange bias. Asymmetrical
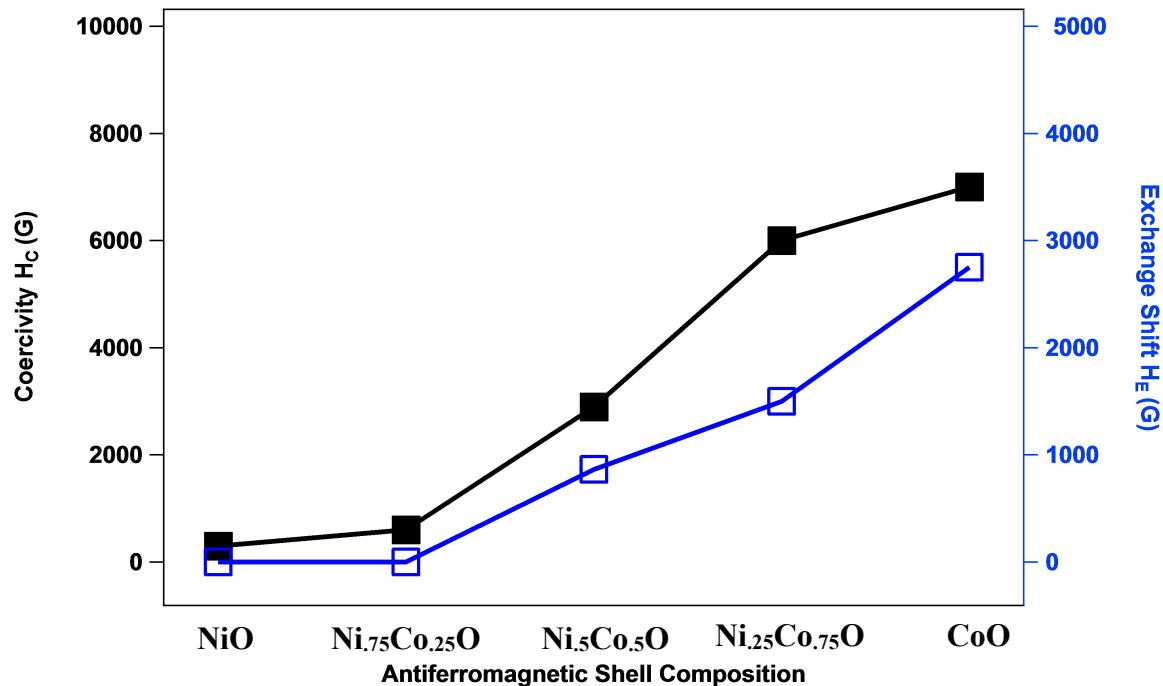
Figure 6-12: Coercivity (left axis) and exchange bias (right axis) as function of the chemical composition of the antiferromagnetic shell.

126

hysteresis is the result of the magnetic relaxation mechanism transitioning through the course of the measurement from the AFM-surface exchange bias mechanism to $CoFe_2O_4$ exchange coupled dominant mechanism. The disordered surface state of the AFM shell contributes to exchange bias shifts through a magnetization shift in the hysteresis loop of all core-shell FM-AFM nanoparticles investigated in this study.

Equation 7 provides a guideline for core-shell material combinations that the anisotropy energy of the AFM phase must exceed the FM phase to exhibit exchange bias properties. **Figure 6-12** shows that the coercivity and exchange bias of $NiFe_2O_4$@$Ni_{1-x}Co_xO$ nanoparticles can be tuned by increasing the anisotropy energy of the antiferromagnetic phase by increasing the molar concentration Co. Maximum coercivity and exchange bias is achieved in core-shell samples with the largest anisotropy energy difference between FM/AFM material phases such as $NiFe_2O_4$@CoO nanocrystals (**Table 6-3**).

The unique exchange bias properties observed for $NiFe_2O_4$@CoO nanocrystals can be further investigated by control of the volume of each material phase (**Equation 6**). Superparamagnetic $NiFe_2O_4$ nanocrystals (4.4 to 10.0 nm) possess a low anisotropy energy resulting in blocking temperatures below 100 K and a coercivity of 300 Oe (**Chapter 2**). Introduction of a high anisotropy energy antiferromagnetic shell such as CoO to $NiFe_2O_4$ nanocrystals results in considerably coercivity enhancement nearly 20-fold from 0.3 KOe to 9.4 KOe (**Figure 6-12**). As exchange bias is known as an interfacial exchange-coupling phenomenon between FM-AFM spins tuning the material interface to volume ratio would result in tuning
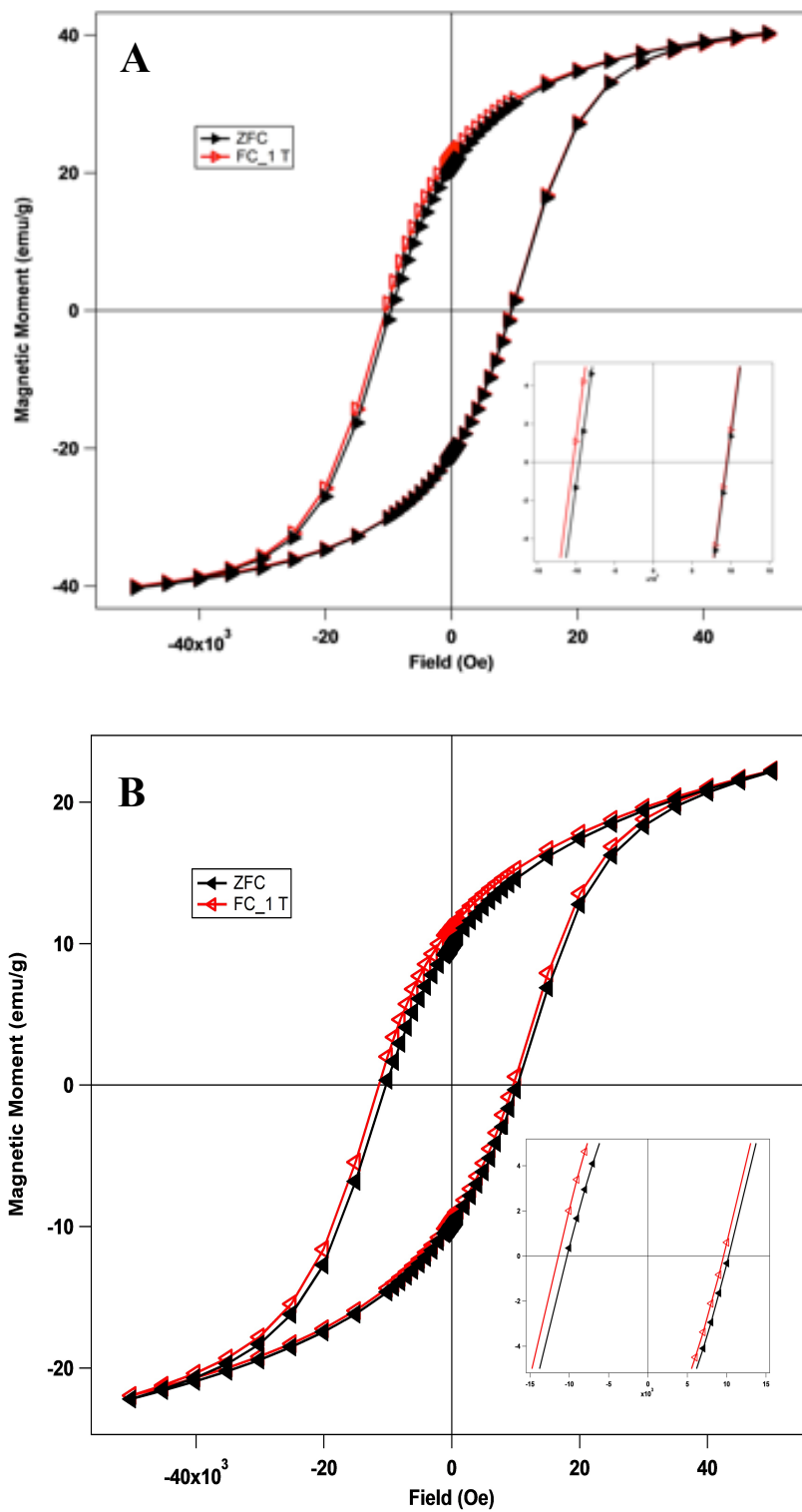
Figure 6-13: Zero-field cooled and field-cooled field dependent magnetic hysteresis measurement of CoFe₂O₄@CoO nanoparticles with CoFe₂O₄ cores (A) 6.0 nm diameter and (B) 4.4 nm diameter measured at 5 K with applied fields ranging from ± 5 Telsa, field-cooled from 305 K under field applied field of 1T.

the magnetic properties of the core-shell system. Through control of the volume of the core NiFe$_2$O$_4$ nanocrystal the interfacial surface area can be tuned as observed in **Table 6-2**. As the volume of the NiFe$_2$O$_4$ core decreases the relative surface area increases and so does the total ferrimagnetic spins available for exchange coupling at the FM-AFM interface. The size-dependent nature of the anisotropy energy can be exploited in to achieve exchange bias in CoFe$_2$O$_4$@CoO nanoparticles by reducing the core CoFe$_2$O$_4$ particles size to 4.4 nm in diameter. This trend collaborates the equation for interfacial exchange energy as reported by Lavorato et al:

$$E_{EX} = \frac{H_E M_S V_{FM}}{A_{int}}$$

(8)
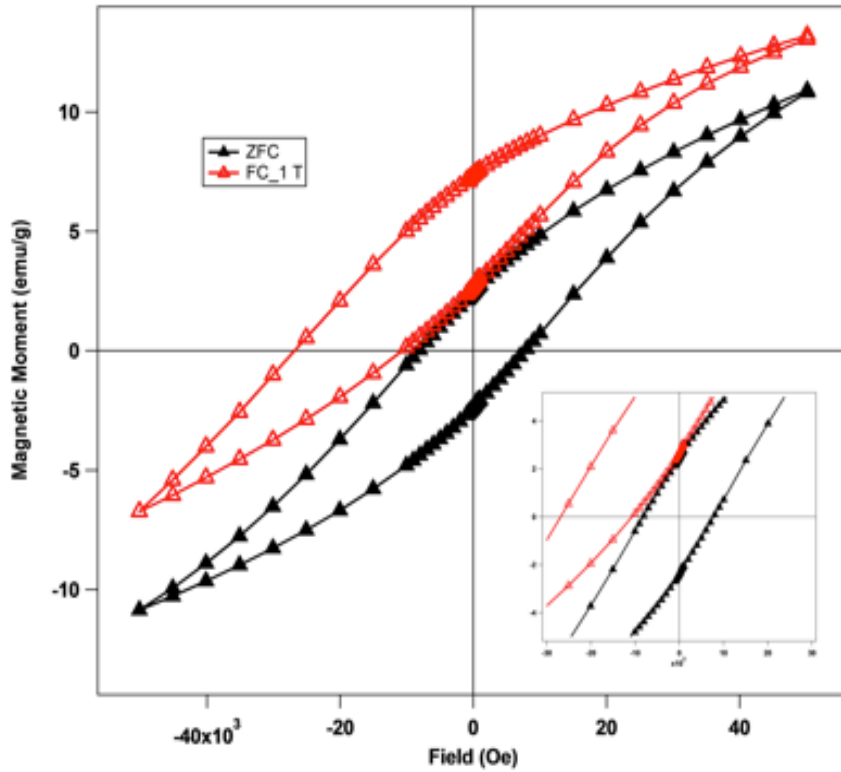
Figure 6-14: Zero-field cooled and field-cooled field dependent magnetic hysteresis measurement of C1 (NiFe$_2$O$_4$@CoO 4.4 nm core) measured at 5 K with applied fields ranging from ± 5 Telsa, field-cooled from 305 K under field applied field of 1T

Where E_{EX} is the interfacial exchange energy, H_E is the exchange field shift, M_S is the saturation magnetization of the ferrimagnet, V_{FM} is the volume of the ferrimagnet, and A_{int} is the interfacial surface area.[25]

Exchange biased core-shell nanoparticles exhibit unique magnetic properties that can overcome "superparamagnetic limitations" of magnetic nanoparticles, but the addition of the antiferromagnetic shell will reduce the magnetization of the core-shell nanoparticle. The addition of an antiferromagnetic shell reduces the saturation and remanent magnetizations in $NiFe_2O_4@CoO$ nanoparticles and as the shell thickness increases the ferrimagnetic volume (V_{FM}) contributions to the net magnetic moment are reduced resulting in decreased magnetic susceptibility, coercivity, saturation, and remanent magnetizations (**Table 6-1**). To optimize exchange bias the antiferromagnetic shell must be thin (~0.5 nm) while maximizing interfacial exchange coupling (**Figure 6-14**). As the antiferromagnetic phase contributes more to the net magnetization of the core-shell $NiFe_2O_4@CoO$ nanoparticle the magnetic properties derived from the interfacial exchange coupling such as coercivity and exchange bias become suppressed.

6.4 Conclusion

We have synthesized bimagnetic core-shell ferrimagnetic-antiferromagnetic nanoparticles with strong exchange coupling between the different magnetic domains yielding tunable exchange bias properties. For bimagnetic FM-AFM nanoparticle to exhibit exchange bias the interfacial AFM spins must "pin" the FM spins ($K_{AFM}V_{AFM} > K_{FM}V_{FM}$). Control of exchange bias properties can be achieved by through tuning the anisotropy energy of the $Ni_{1-x}Co_xO$ antiferromagnetic shell by increasing the molar

concentration of cobalt. Materials with a large difference in anisotropy energy such as NiFe$_2$O$_4$@CoO yield the largest enhancements of coercivity and exchange bias of the chemical compositions studied. By varying the core-shell dimensions of NiFe$_2$O$_4$@CoO nanoparticle system the FM-AFM interfacial exchange coupling energy can be optimized to tune the thermal stability, coercivity, and exchange bias. The interfacial exchange coupling energy is maximized by increasing the surface are to volume ratio of the ferrimagnetic core, while reducing the volume of the antiferromagnetic shell resulting in exchange bias H$_E$ of 18.0 KOe for (4.4 nm) NiFe$_2$O$_4$@CoO nanoparticles. In summary, we have demonstrated a new approach to synthesize variable combinations of FM-AFM core-shell nanoparticles with tunable magnetic properties such as thermal stability, coercivity, and exchange bias that can meet the demands a broad array of technological applications.

6.5 REFERENCES

1.   López-Ortega, A.; Estrader, M.; Salazar-Alvarez, G.; Roca, A. G.; Nogués, J., Applications of exchange coupled bi-magnetic hard/soft and soft/hard magnetic core/shell nanoparticles. *Physics Reports* **2015,** *553*, 1-32.

2.   Song, Q., Size and Shape Controlled Synthesis and Superparamagnetic Properties of Spinel Ferrites Nanocrystals. **2005,** 216.

3.   Manjura Hoque, S.; Srivastava, C.; Kumar, V.; Venkatesh, N.; Das, H. N.; Saha, D. K.; Chattopadhyay, K., Exchange-spring mechanism of soft and hard ferrite nanocomposites. *Mater Res Bull.* **2013,** *48* (8), 2871-2877.

4.   A.E. Berkowitz, K. T., Exchange Anisotropy - A Review. *J Magn Magn Mat.* **1999,** *200*, 522-570.

5.   Meiklejohn, W. H.; Bean, C. P., New Magnetic Anisotropy. *Phys Rev.* **1957,** *105* (3), 904-913.

6.   De Toro, J. A.; Marques, D. P.; Muniz, P.; Skumryev, V.; Sort, J.; Givord, D.; Nogues, J., High Temperature Magnetic Stabilization of Cobalt Nanoparticles by an Antiferromagnetic Proximity Effect. *Phys Rev Lett* **2015,** *115* (5), 057201.

7.   Manna, P. K.; Yusuf, S. M., Two interface effects: Exchange bias and magnetic proximity. *Phys Rep.* **2014,** *535* (2), 61-99.

8.   Jung, M.-S.; Kim, T.-H.; Im, M.-Y.; Hong, J.-I., Overcoming the limits of exchange bias effect in the magnetic thin films by introducing nanostructured internal interfaces. *J Magn Magn Mat.* **2020,** *494*.

9.   Giri, S.; Patra, M.; Majumdar, S., Exchange bias effect in alloys and compounds. *J Phys Condens Matter* **2011,** *23* (7), 073201.

10.   Binasch, G.; Grunberg, P.; Saurenbach, F.; Zinn, W., Enhanced magnetoresistance in layered magnetic structures with antiferromagnetic interlayer exchange. *Phys Rev B Condens Matter* **1989,** *39* (7), 4828-4830.

11.   Baibich, M. N.; Broto, J. M.; Fert, A.; Nguyen Van Dau, F.; Petroff, F.; Etienne, P.; Creuzet, G.; Friederich, A.; Chazelas, J., Giant magnetoresistance of (001)Fe/(001)Cr magnetic superlattices. *Phys Rev Lett* **1988,** *61* (21), 2472-2475.

12.   Claude Chappert, A. F., and Frederic Nguyen Van Dau, The Emergence of Spin Electronics in Data Storage. *Nature Materials* **2007,** *6*, 813-823.

13.   Zutic, I., Spintronic: Fundamentals and Applications. *Rev Modern Phys.* **2004,** *76*, 323-410.

14.   Carey, M. J.; Berkowitz, A. E., Exchange anisotropy in coupled films of Ni81Fe19 with NiO and CoxNi1−xO. *Appl Phys Lett.* **1992,** *60* (24), 3060-3062.

15.   Leighton, C.; Suhl, H.; Pechan, M. J.; Compton, R.; Nogués, J.; Schuller, I. K., Coercivity enhancement above the Néel temperature of an antiferromagnet/ferromagnet bilayer. *J Appl Phys.* **2002,** *92* (3), 1483-1488.

16.	González, J. A.; Andrés, J. P.; López Antón, R.; De Toro, J. A.; Normile, P. S.; Muñiz, P.; Riveiro, J. M.; Nogués, J., Maximizing Exchange Bias in Co/CoO Core/Shell Nanoparticles by Lattice Matching between the Shell and the Embedding Matrix. *Chem Mater.* **2017,** *29* (12), 5200-5206.

17.	Sun, X.; Huls, N. F.; Sigdel, A.; Sun, S., Tuning exchange bias in core/shell FeO/Fe3O4 nanoparticles. *Nano Lett* **2012,** *12* (1), 246-51.

18.	Thakur, M.; Patra, M.; Majumdar, S.; Giri, S., Influence of cooling field on the magnetic properties of Ni/NiO nanostructure. *J Alloys Compd.* **2009,** *480* (2), 193-197.

19.	Gredig, T.; Krivorotov, I. N.; Eames, P.; Dahlberg, E. D., Unidirectional coercivity enhancement in exchange-biased Co/CoO. *Appl Phys Lett.* **2002,** *81* (7), 1270-1272.

20.	Gilbert, D. A.; Olamit, J.; Dumas, R. K.; Kirby, B. J.; Grutter, A. J.; Maranville, B. B.; Arenholz, E.; Borchers, J. A.; Liu, K., Controllable positive exchange bias via redox-driven oxygen migration. *Nat Commun* **2016,** *7*, 11050.

21.	Nogués, J.; Sort, J.; Langlais, V.; Skumryev, V.; Suriñach, S.; Muñoz, J. S.; Baró, M. D., Exchange bias in nanostructures. *Phys Rep.* **2005,** *422* (3), 65-117.

22.	Saha, A.; Sohoni, S.; Viswanatha, R., Interface Modeling Leading to Giant Exchange Bias from the CoO/CoFe2O4 Quantum Dot Heterostructure. *J Phys Chem C.* **2019,** *123* (4), 2421-2427.

23.	Lima, E.; Winkler, E. L.; Tobia, D.; Troiani, H. E.; Zysler, R. D.; Agostinelli, E.; Fiorani, D., Bimagnetic CoO Core/CoFe2O4 Shell Nanoparticles: Synthesis and Magnetic Properties. *Chem Mater.* **2012,** *24* (3), 512-516.

24.	Fontaíña Troitiño, N.; Rivas-Murias, B.; Rodríguez-González, B.; Salgueiriño, V., Exchange Bias Effect in CoO@Fe3O4Core–Shell Octahedron-Shaped Nanoparticles. *Chem Mater.* **2014,** *26* (19), 5566-5575.

25.	Lavorato, G. C.; Lima, E.; Troiani, H. E.; Zysler, R. D.; Winkler, E. L., Tuning the coercivity and exchange bias by controlling the interface coupling in bimagnetic core/shell nanoparticles. *Nanoscale* **2017,** *9* (29), 10240-10247.

26.	Tannous, C.; Gieraltowski, J., The Stoner–Wohlfarth model of ferromagnetism. *Eur J Phys.* **2008,** *29* (3), 475-487.

27.	Ichiyanagi, Y., Magnetic properties of NiO nanoparticles. *Physica B: Condensed Matter* **2003,** *329-333*, 862-863.

28.	Ghosh, M.; Sampathkumaran, E. V.; Rao, C. N. R., Synthesis and Magnetic Properties of CoO Nanoparticles. *Chem Mater.* **2005,** *17* (9), 2348-2352.

CHAPTER 7: FABRICATION OF NANOMAGNETIC FILMS

FOR MICROWAVE TECHNOLOGY APPLICATIONS

7.1 Introduction

Modern society has become ever more interconnected with cell phones and other wireless devices becoming integrated to many aspects of daily life. The increased dependence on wireless technologies has crowded available radio frequencies sparking renewed research into the development of novel approaches to expand access to ultrahigh radio frequencies.[1]   Signal overcrowding and radio frequency interference are compounding issues that require microwave devices such as isolators, conductors, and frequency selective limiters that can mitigate signal noise.[2-6] Frequency selective limiters are of particular interest as they suppress interfering signals allowing the reception of desired signals.[1] FSL devices are typically composed of microwave ferrites, a class of magnetic materials that absorbs microwave radiation consisting of hexaferrites, garnets, and spinel ferrites.[7]

Spinel ferrites standout amongst other microwave ferrites as they possess well-established literature describing both bulk and nanoscale synthesis and characterization of their magnetic properties.[7] The crystallographic structure of spinel ferrites is a bcc unit cell composed of two sublattices AB_2O_4 in which the A sublattice is antiferromagnetically coupled to the B sublattice resulting in net ferrimagnetism.[8] The ferrimagnetic ordering can be modified through substitution of different metal cations into the crystal structure or
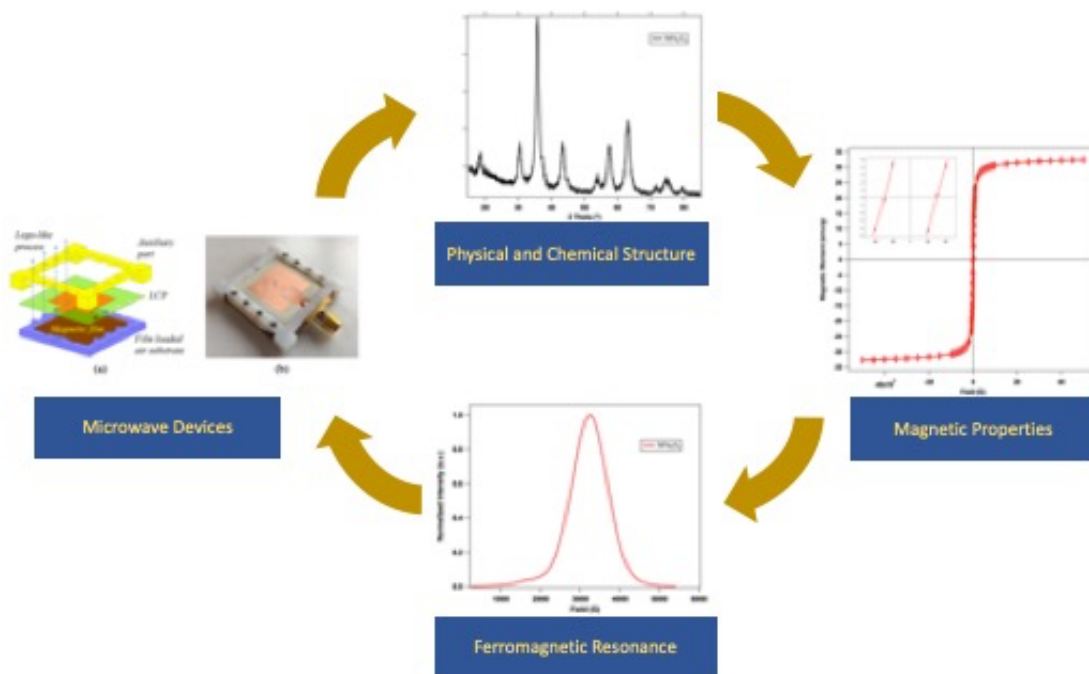
Figure 7-1: Nanomagnetic films project outline, synthesis of spinel ferrite nanocrystals, physical and magnetic characterization, ferromagnetic resonance spectroscopy analysis, and fabrication/implementation into microwave devices.

altering the distribution of metal cations amongst the A/B sites. Magnetic diversity of spinel ferrites is dynamic ranging from hard magnets such as $CoFe_2O_4$ to soft magnets as Fe_3O_4, $MnFe_2O_4$, and $NiFe_2O_4$.[9] Single-domain spinel ferrite nanoparticles provide a simplified model to magnetic properties as considerations such as migration of magnetic domain wall and crystallographic defects are mitigated.[10] We have systematically studied the magnetic and ferromagnetic resonance properties of spinel ferrite nanoparticles including size-dependent properties of $NiFe_2O_4$ nanoparticles, composition dependent properties of mixed solid solution $Ni_{1-x}M_xFe_2O_4$ (M = Zn^{2+} and Co^{2+}), and exchange coupled core@shell nanoparticles ($NiFe_2O_4@CoFe_2O_4$ and inverted $CoFe_2O_4@NiFe_2O_4$).
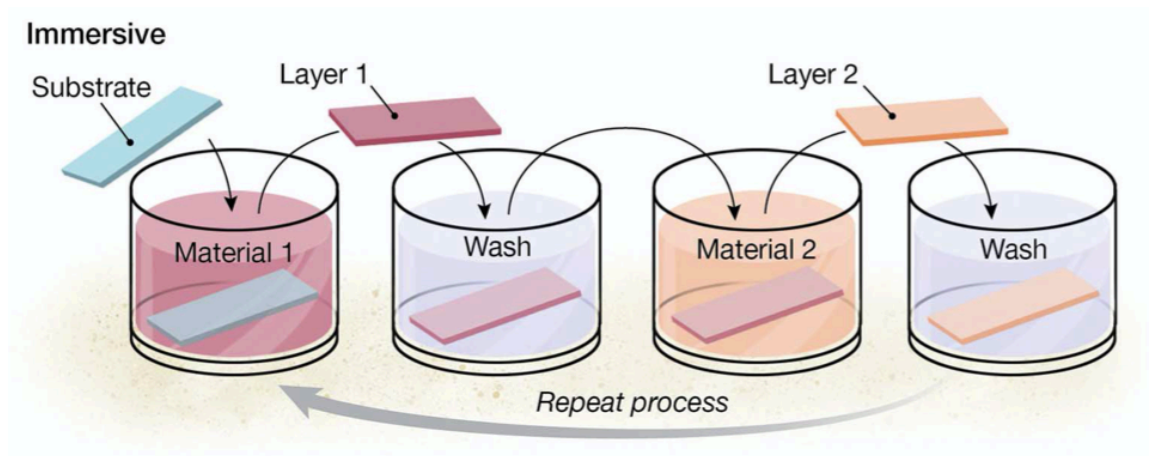
Figure 7-2: Layer-by-layer fabrication method for thin films.[11]

Nanomagnetic films have been fabricated through a myriad of methods such as layer-by-layer, spin-coating, lithography, and solution casting.[11-13] In this report, we have focused our efforts on solution casting technique to efficiently produce micron thick films with large nanoparticle densities. Solution casting method can be broken down into fabrication stages: modification > casting > sealing > annealing. Modification involves the chemical binding of anchor molecules to the surface of the substrate and nanoparticles to stabilize

Figure 7-3: Layer-by-layer polyelectrolyte nanomagnetic film prototype.
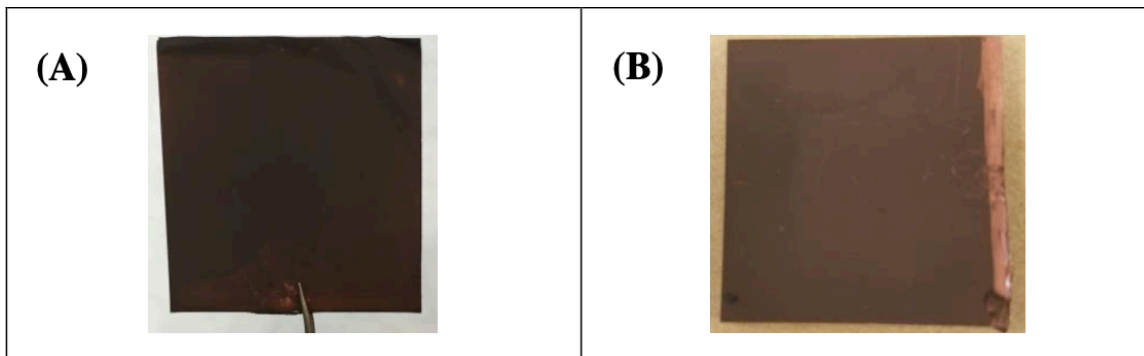
Figure 7-4: Layer-by-layer method fabricated nanomagnetic films on (A) glass and (B) copper substrates

the film.[13, 14] Solution casting of prepared colloidal solutions onto the modified substrate. After evaporation of the solvent and stable formation of the film it is chemically sealed by spin coating a polymer sealant over the film. Final annealing of the film sets the polymer sealant and protecting the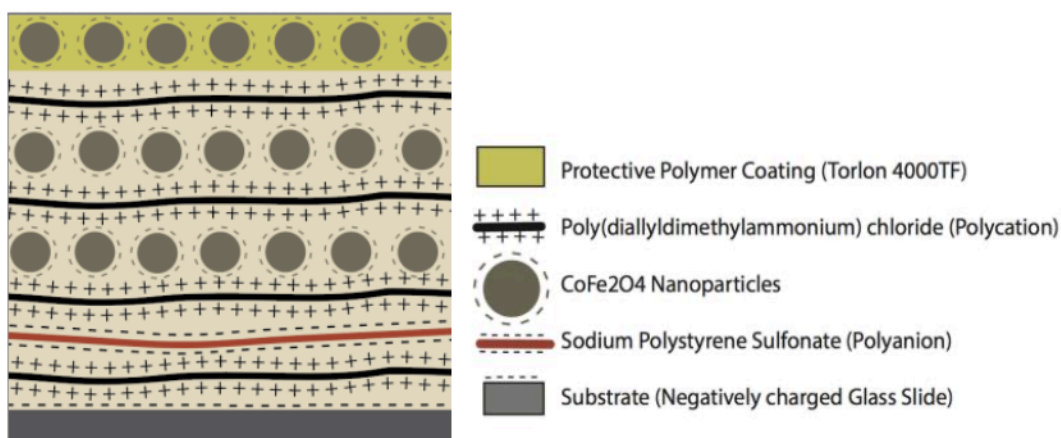 fabricated film from damage. The fabricated films are tested by our collaborating team of engineers at Michigan State University under the direction of Dr. John Papapolymerou.

7.2 Experimental

7.2.1 Synthesis and Characterization of Spinel Ferrite Nanocrystals

All spinel ferrite nanocrystals utilized for fabrication of nanomagnetic films were fabricated via the aminolytic synthetic method as outline in earlier chapters I-V. The size and crystal structure of synthesized nanoparticles was confirmed with powder x-ray diffraction on Bruker D8 Advance diffractometer. Chemical composition was analyzed by total reflection x-ray spectroscopy (T-XRF) with a Bruker S2 Picofox instrument. Temperature and field-dependent magnetization measurements were performed on all

139

sample compositions with on MPMS-5 Superconducting Quantum Interference Device (SQUID). Ferromagnetic resonance spectrums were measured with a Bruker EMX spectrometer operating at X-band frequency (9.88 GHz). The physical and magnetic characterizations of as-synthesized spinel ferrite nanocrystals listed above were also described in great detail in **Chapters I-V** and will not be further explained.

7.2.2 *Surface Modification of Nanoparticles*

As-synthesized nanoparticle batches were first stripped of surface ligands (oleylamine) by preparing a colloidal suspension in a 50/50 solution composed of aqueous 10 M NaOH solution and 180-proof ethanol. The nanoparticle suspension was sonicated for 1 hour after which the nanoparticles were collected via strong magnet to decant the cleaning solution. This procedure is repeated five times to ensure complete removal of the oleylamine surface ligands with hydroxyl functional groups. Successfully stripped nanoparticles can be noted by ability to form colloids in aqueous solutions.
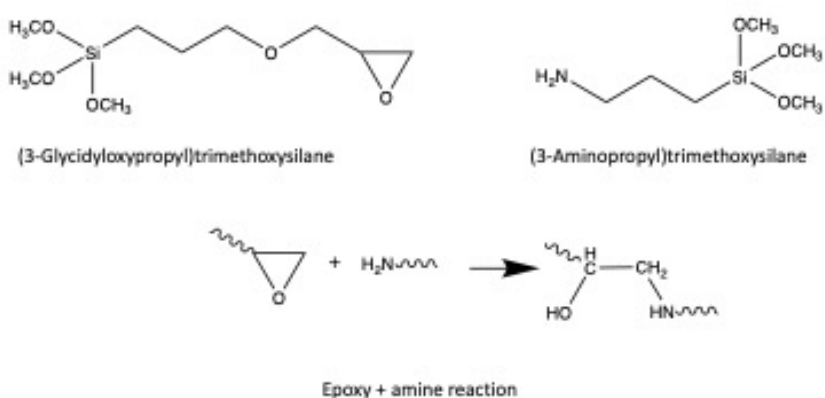
Figure 7-5: Reaction scheme of surface ligands undergoing an epoxide amine reaction to create interparticle and nanoparticle to surface cross-linkages.

The half of the stripped nanoparticles will be suspended in 5% v/v solution of (3-glycidyloxypropyl) trimethoxysilane in ethanol and undergo sonication for 2 hours. After sonication the nanoparticles are collected via magnet and excess solution is removed. The silane will bond to the hydroxyl functionalized surface resulting in new (3-glycidyloxypropyl) trimethoxysilane coated nanoparticles. This procedure is repeated on the second half of the nanoparticles to with 3-aminotriethoxysilane to produce 3-aminotriethoxysilane coated nanoparticles.

Silane-modified nanoparticles are suspended in 10% solution of PMMA (polymethyl methacrylate) in DCM (dichloromethane). It is necessary to apply low heat ~80°C to solubilize PMMA in DCM, necessary precautions must be taken to avoid

Figure 7-6: Normalized integrated ferromagnetic resonance spectra of varied spinel ferrite nanoparticles measured frequency of 9.88 GHz with applied field swept from 250 to 10,000 Oe.

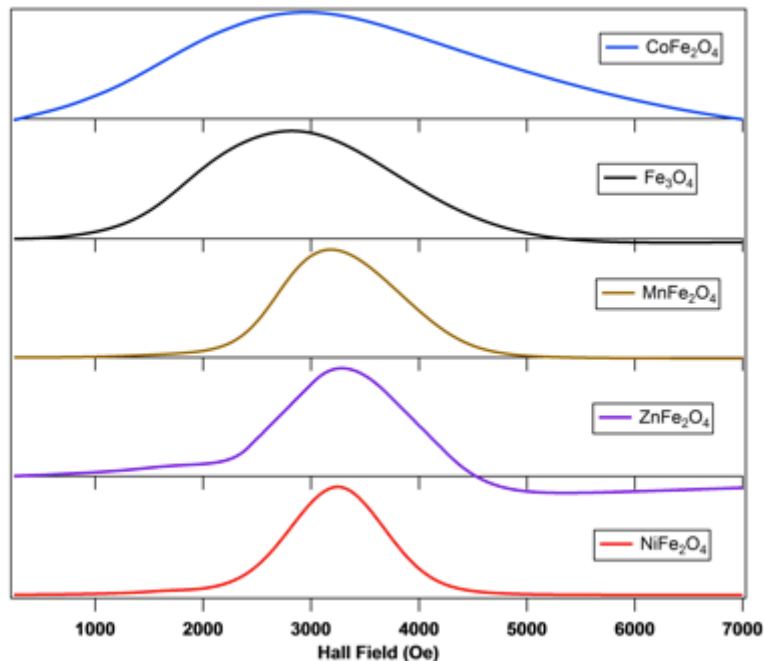inhalation of DCM vapors. This colloidal suspension is ready to be utilized in solution casting procedure.

7.2.3   Substrate Modification

Substrates are suspended in a 1 M NaOH aqueous solution for 1 hour to clean the surface. The substrates are removed and allowed to dry before suspending in a 5% v/v solution of (3-glycidyloxypropyl) trimethoxysilane in ethanol for 1 hour. After drying the substrates are ready for solution casting procedure. Some substrates require further preparation and modification that are unique to each substrate design/surface.

7.2.4   Solution Casting Procedure

Film substrate is modified in the fashion to serve as a well for colloid suspension to be cast into. Mix both 3-aminotriethoxysilane and (3-glycidyloxypropyl) trimethoxysilane colloid suspensions together and apply to the substrate well with a syringe. Allow the solvent to evaporate and the film to set for approximately 30 minutes. Repeat procedure to achieve desired film thickness.

Upon achieving desired film thickness a 10% solution of PMMA in DCM is spin-coated onto the surface. The film is annealed at 150°C for 1 hour to seal the finished film.

7.3 Results

Physical characterization of fabricated nanomagnetic films is limited due to the technical demand of testing microwave device testing requires intact films. Nanoparticle loading density of finished nanomagnetic film was determined by thermogravimetric
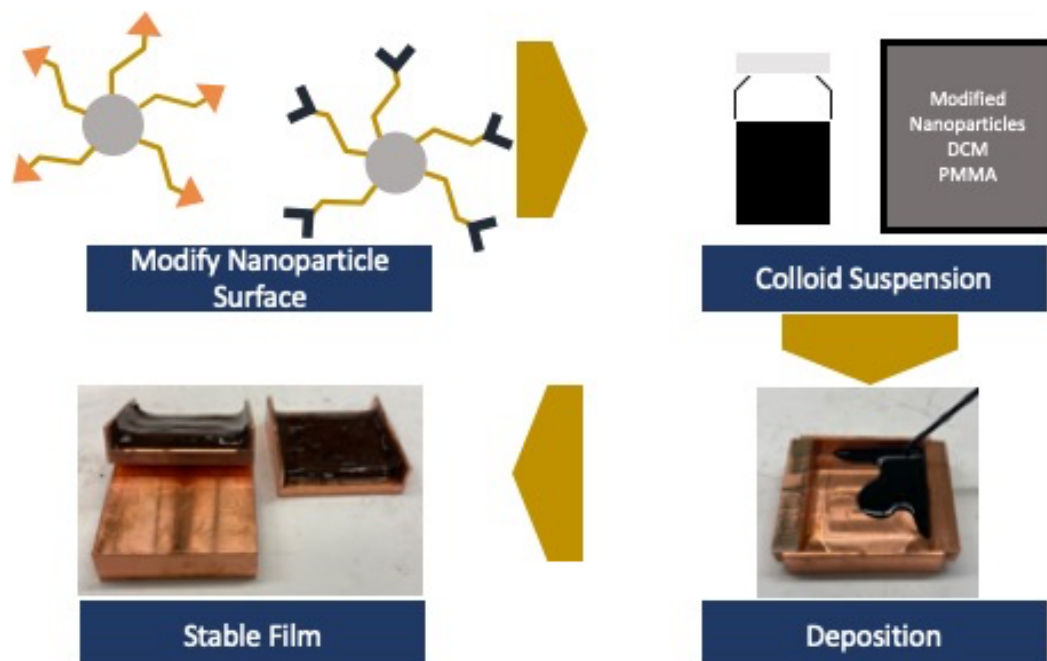
142

Figure 7-7: Solution cast fabrication method for to produce stable micron-millimeter thick nanomagnetic films.

analysis (TGA) by calculating weight loss percentage. Approximately 50 mg samples of

nanomagnetic films sample was placed in the TGA balance and heated at 5°C per minute

from $22 - 400^\circ$C. Nanomagnetic film thicknesses and surface roughness were measured

Table 7-1: Magnetic and ferromagnetic resonance properties of mixed composition spinel ferrite nanocrystals and core@shell nanoparticles

Sample	Stoichiometry T-XRF	Crystallite Size XRD (nm)	T_B	H_C (Oe)	M_S (emu/g)	M_R (emu/g)	Resonance Field (Oe)	Linewidth (Oe)
$ZnFe_2O_4$	$Zn_1:Fe_2$	5.8	45	150	87.1	16.7	3444	795
$Ni_{.25}Zn_{.75}Fe_2O_4$	$Ni_{.31}:Zn_{.63}:Fe_{2.06}$	6.5	45	N/A	N/A	N/A	3309	1144
$Ni_{.5}Zn_{.5}Fe_2O_4$	$Ni_{.6}:Zn_{.45}:Fe_{1.95}$	5.5	35	100	58.5	9.8	3308	965
$Ni_{.75}Zn_{.25}Fe_2O_4$	$Ni_{.83}:Zn_{.26}:Fe_{1.9}$	6.0	35	N/A	N/A	N/A	3279	970
$NiFe_2O_4$	$Ni_{.97}:Fe_{2.06}$	6.0	45	300	32.4	11.5	3248	705
$Ni_{.75}Co_{.25}Fe_2O_4$	$Ni_{.78}:Co_{.23}:Fe_{1.93}$	5.8	135	3700	53.7	31.4	3015	2700
$Ni_{.5}Co_{.5}Fe_2O_4$	$Ni_{.5}:Co_{.43}:Fe_{2.05}$	5.7	175	5700	59.1	35.5	2965	2775
$Ni_{.25}Co_{.75}Fe_2O_4$	$Ni_{.3}:Co_{.72}:Fe_{1.98}$	5.6	185	8500	52.4	31.5	2919	3260
$CoFe_2O_4$	$Co_{.96}:Fe_{2.07}$	5.1	225	10,000	62.9	35.4	2850	3460
$NiFe_2O_4@CoFe_2O_4$		7.0	225	5000	47.9	30.9	3115	2650
$CoFe_2O_4@NiFe_2O_4$		7.0	225	7000	49.4	33.1	2710	3020

via profilometer for each unique film after testing by our collaborators at Michigan State University. Fabricated films were shipped to Michigan State University to be tested as microwave devices by measuring microwave absorption profiles with vector network analyzer.

7.4 Discussion

In **Chapters II-V** of this thesis we have demonstrated the ability to tune the unique ferromagnetic resonance profile of spinel ferrite nanocrystals through synthetic control of the magnetocrystalline anisotropy energy by varying physical parameters of the nanoparticle such as the size, chemical composition, and/or core@shell architecture (**Table 7-1**). Development of versatile film fabrication methods to produce nanomagnetic films is
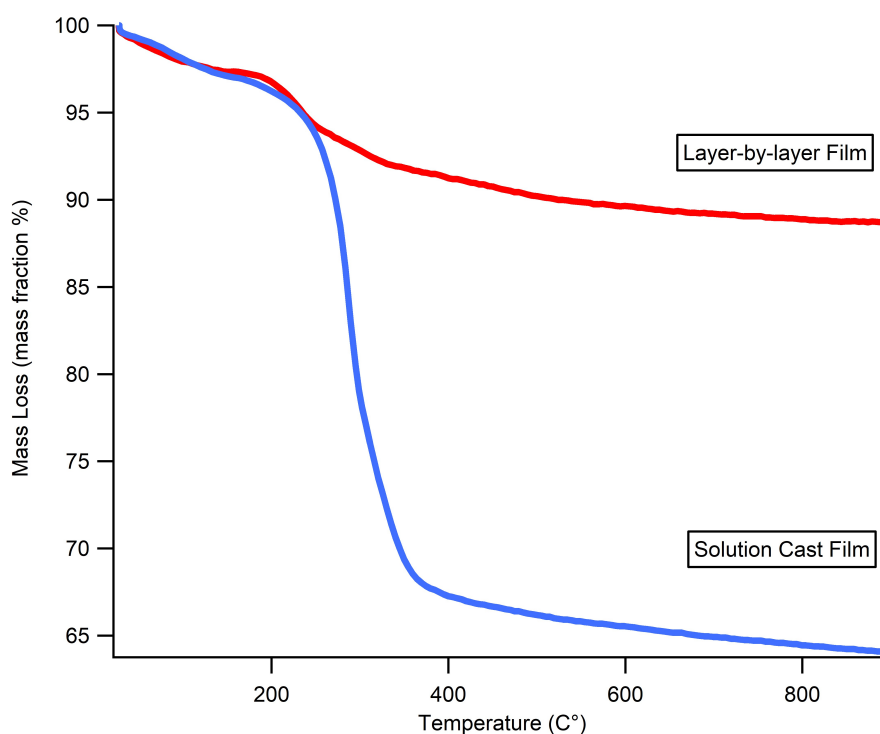

Figure 7-8:   Thermogravimetric analysis demonstrating nanoparticle load density of two films fabricated by the layer-by-layer and the solution cast methods.

144

essential to meet the application needs of modern microwave devices. To this effort, solution-casting technique have been developed to provide a time efficient and scalable approach to fabrication of nanomagnetic films of variable technical parameters. Solution cast nanomagnetic films have been effectively applied to a myriad of substrate materials and shapes.

Initial attempts at fabrication of nanomagnetic thin films for microwave device utilized layer-by-layer technique but were determined to be inefficient and time consuming (**Figure 7-2**).[9] The thin films produced by layer-by-layer technique were ranged from 1 –
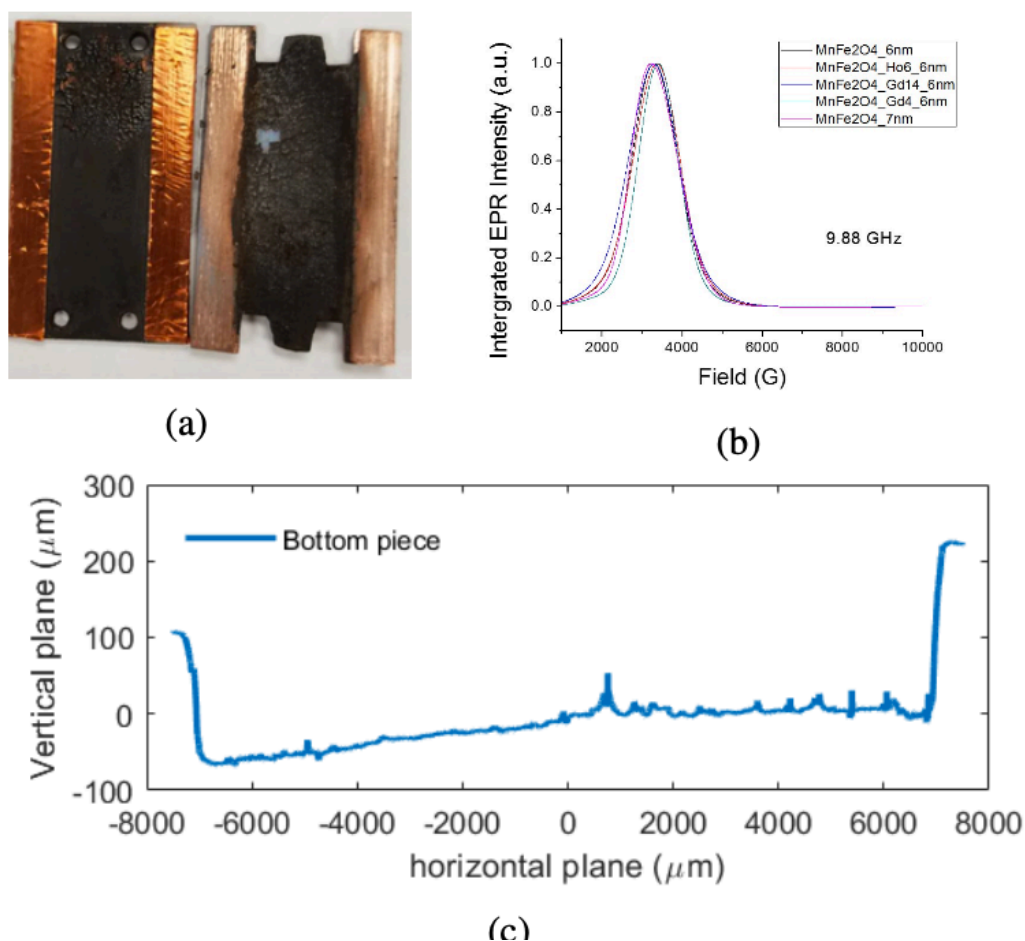

Figure 7-9: Solution cast MnFe₂O₄ nanomagnetic film (A) image of film, (B) FMR spectra of rare-earth doped MnFe₂O₄ nanoparticles, and (C) surface roughness measurement of solution cast film.[15]

100 micron in film thickness with nanoparticle load density approximately 95%. Vector network analysis of these films resulted in minimal signal enhancement due to the low overall nanoparticle loading in the thin film (**Figure 7-8**). Enhancing the thickness of the film via layer-by-layer technique was laborious with increasingly marginalized benefits as the film became increasingly unstable. Films produced via layer-by-layer method are depicted in **Figure 7-4**. The technical demands of microwave devices required efficient fabrication of quality films ranging in thickness from 0.1 - 10 millimeters.

The solution-casting technique utilizes a colloidal solution of surface-functionalized nanoparticles, a stabilizing additive (PMMA), and low boiling point solvent (DCM). The nanoparticles are functionalized with (3-glycidyloxypropyl) trimethoxysilane and 3-aminotriethoxysilane with the silane functional group chemically bonded to the nanoparticle surface resulting in the epoxide and amine functional groups outward facing.[15] The outward facing functional epoxide and amine functional groups can undergo an amine-epoxide reaction resulting in the creation of chemical bridges between functionalized
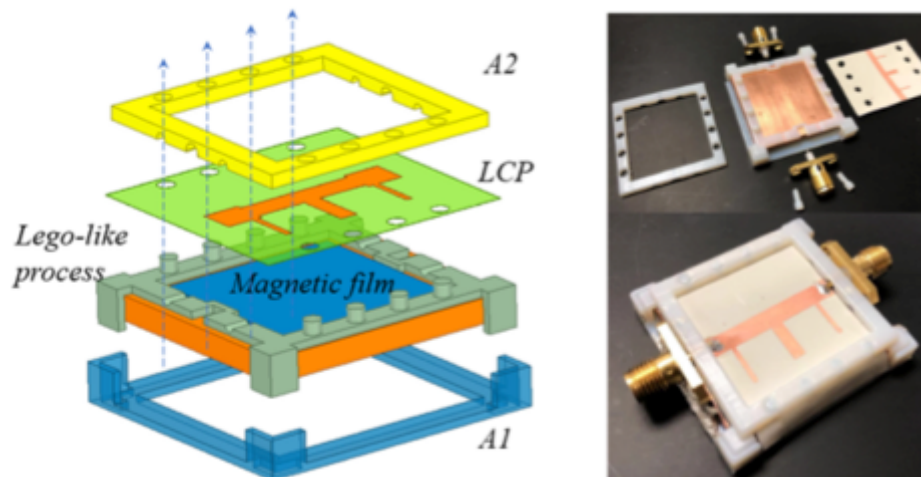

Figure 7-10: Fabricated sample (A) the lego-like 3D printed assembly, (B) Fully assembled microstrip devices.[15]

nanoparticles. The amine-epoxide reaction was utilized previously to build nanoparticle layers in the layer-by-layer method through alternating application of functionalized nanoparticles.[9] Polymethyl methacrylate (PMMA) serves as the primary stabilizer for the solution-casting technique by forming a solid glass-state after removal of the solvent. The PMMA to nanoparticle w/w% can be adjusted to increase nanoparticle loading density or increase film stability, 5 w/w% PMMA was found to produce stable nanomagnetic films that could achieve thicknesses above 50 microns.

Physical characterization of the nanomagnetic films was performed by thermogravimetric analysis (TGA). Comparison of nanoparticle loading density of films produced by both layer-by-layer and solution cast methods was performed by TGA as shown in **Figure 7-8**. Films fabricated by layer-by-layer technique consist of 95 w/w% nanoparticles while the solution cast films are only 65 w/w% nanoparticles. The layer-by-layer technique builds nanomagnetic films by alternating washes of surface-modified nanoparticle solutions: solution A consists of 3-aminotriethoxysilane coated nanoparticles, and solution B consists of (3-glycidyloxypropyl) trimethoxysilane coated nanoparticles. Alternating nanoparticle washes gradually builds the film by chemical reaction of the surface ligands via amine-epoxide reaction. As the film consists of only the nanoparticles and surface ligands the films produced in this manner have high nanoparticle loading density (95 w/w%) but are unstable upon continued application of the layer-by-layer technique limiting the film thickness to approximately 50 microns. The solution casting technique stabilizes the nanomagnetic film with the additive PMMA to build thicker films ranging 0.1 to 10 millimeters thick. Only 10 w/w% PMMA is added to the nanoparticle colloid solution which in addition to the surface ligands of the nanoparticle would estimate

the nanoparticle loading density to be larger than the 65 w/w% observed by TGA. The solution casting technique relies heavily on homogeneity of the colloidal suspension of nanoparticles thus precipitated nanoparticles maybe lost upon application of the solution to substrate via syringe. While solution cast films have reduced nanoparticle loading capacity as compared to layer-by-layer films the increased film stability and film thickness increases the net amount of nanoparticles.

The versatility of solution casting is demonstrated in **Figure 7-7** that highlight nanomagnetic films of various nanocrystal compositions, substrate materials, substrate designs, and film thickness. **Figure 7-9** depicts micron thick films composed of $MnFe_2O_4$ Nanomagnetic films depicted in **Figure 7-7** are composed of $NiFe_2O_4$ nanocrystals
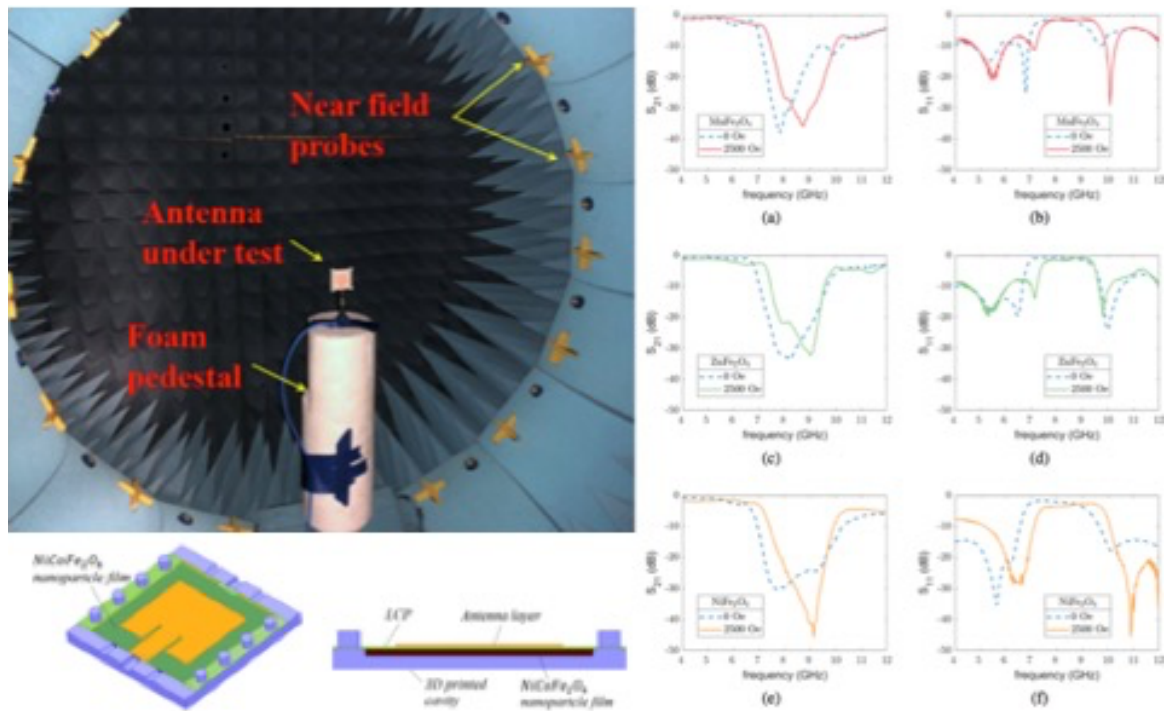

Figure 7-11: (Left) Antenna testing setup with model for antenna assembly with nanomagnetic film on 3D printed cavity. (Right) Vector network analyzer measurements at with and without 2500 Oe applied field for nanomagnetic films composed of $MnFe_2O_4$ (A,B), $ZnFe_2O_4$ (C,D), and $NiFe_2O_4$ (E,F).[15]

deposited onto copper well substrate approximately 10 microns in thickness. Solution casting also holds potential as a scalable fabrication technique that is clean room compatible and could be modified for 3D-printed film designs.

Our collaborators at Michigan State University analyze the fabricated nanomagnetic films as potential microwave devices with a vector network analyzer. An antennae assembly was fitted over the nanomagnetic films in a lego-like assembly as shown in **Figure 7-10**. Vector network analyzers measure the microwave absorption of a sample by sweeping the applied frequency while the applied magnetic field is held constant. The assembled antennae were tested under both self-biased and DC magnetic biased to determine antennae performance. Sample results of their measurements for $NiFe_2O_4$ nanocrystal films are shown in **Figure 7-11**. These $NiFe_2O_4$ films are early prototypes fabricated with the solution casting method that highlight significant surface cracking and roughness (**Figure 7-9**). The results for samples S1-S3 demonstrate that the presence of the nanomagnetic film shifts the signal frequency and increased impedance bandwith.* Significant improvements to the quality of the film surface as shown in **Figure 7-7** should enhance the antennae performance.

7.5 Conclusions

Fabrication of nanomagnetic films for ultrahigh frequency antennae devices is a project in the early stages with considerable future goals to achieve. Solution casting technique has solved the issues of nanoparticle loading density through significantly increasing the film thickness to millimeter range. As outlined in Chapters II-IV of this thesis the ferromagnetic resonance profile of spinel ferrite nanocrystals can be tuned

through modifying the magnetocrystalline anisotropy energy via synthetically controlling the size, chemical composition, and/or the core@shell architecture of the nanocrystals. These studies enable the selection of nanocrystals with specific FMR properties to meet technical demands of the antennae device. Nanomagnetic films hold significant potential outside the laboratory setting and evolution of the solution casting method to be compatible with clean room fabrication and 3D-printing techniques would vastly improve industrial relevance. Nanomagnetic film-based microwave antennas are key to miniaturization of device components and improving accessibility to radio frequencies.

7.6 REFERENCES

1.   Harris, V. G., Modern Microwave Ferrites. *IEEE Trans Magn.* **2012,** *48* (3), 1075-1104.

2.   Pardavi-Horvath, M., Microwave Applications of Soft Ferrites. *J Magn Magn Mater.* **2000,** *215*, 171-183.

3.   Adam, J. D., Mitigate the Interference: Nonlinear Frequency Selective Ferrite Devices. *IEEE Microwave Magazine* **2014,** *15* (6), 45-56.

4.   Zhu, J.; Zhao, M.; Zhou, S., An Optimization Design of Ultra Dense Networks Balancing Mobility and Densification. *IEEE Access* **2018,** *6*, 32339-32348.

5.   Venugopal, A.; Qu, T.; Victora, R. H., Nonlinear Parallel-Pumped FMR: Three and Four Magnon Processes. *IEEE Trans Microwave Theory and Techniques* **2020,** *68* (2), 602-610.

6.   Givernaud, J.; Crunteanu, A.; Orlianges, J.-C.; Pothier, A.; Champeaux, C.; Catherinot, A.; Blondy, P., Microwave Power Limiting Devices Based on the Semiconductor–Metal Transition in Vanadium–Dioxide Thin Films. *IEEE Transactions on Microwave Theory and Techniques* **2010,** *58* (9), 2352-2361.

7.   Alcalá, O.; Briceño, S.; Brämer-Escamilla, W.; Silva, P., Toroidal cores of Mn x Co 1−x Fe 2 O 4 / PAA nanocomposites with potential applications in antennas. *Mater Chem Phys.* **2017,** *192*, 17-21.

8.   Sabo, D. E., Novel Synthesis of Metal Oxide Nanoparticles via the Aminolytic Method and the Investigation of Their Magnetic Properties. **2012**, 158.

9.   Chen, H. W., Aminolytic Synthesis and Ferromagnetic Resonance of Cobalt and Manganese Based Spinel Ferrite Nanoparticles. **2018**, 148.

10.   Bedanta, S.; Kleemann, W., Supermagnetism. *Journal of Physics D: Applied Physics* **2009,** *42*, 1-28.

11.   Richardson, J. J.; Bjornmalm, M.; Caruso, F., Multilayer assembly. Technology-driven layer-by-layer assembly of nanofilms. *Science* **2015,** *348* (6233), aaa2491.

12.   Kotov, N. A., Layer-By-Layer Self-Assembly: The Contribution of Hydrophobic Interactions. *A. Nanostruct. Mater.* **1999,** *12*, 789.

13.   Zhang, X.; Chen, H.; Zhang, H., Layer-by-layer assembly: from conventional to unconventional methods. *Chem Commun (Camb)* **2007,** (14), 1395-405.

14.   Nothdurft, P.; Feldbacher, S.; Jakopic, G.; Mühlbacher, I.; Pötz, S.; Kern, W., Surface characterization of copper substrates modified with carboxyl terminated phosphonic acids. *International Journal of Adhesion and Adhesives* **2018,** *84*, 143-152.

15.   He, Y.; Chen, W.-Y.; Drew, E.; Zhang, Z. J.; Papapolymerou, J., Fabrication and Characterization of $CoFe_2O_4$ and $MnFe_2O_4$ Nanomagnetic Thin Films for RF Applications. *IEEE Transactions on Components, Packaging and Manufacturing Technology* **2019,** *9* (5), 973-983.